UNIVERSITY OF TECHNOLOGY SYDNEY
School of Mathematical and Physical Sciences

Stimulated Brillouin scattering in nanophotonic waveguides and resonators

by

Sayyed Reza Mirnaziry

A Thesis Submitted
in Partial Fulfillment of the
Requirements for the Degree

Doctor of Philosophy

Sydney, Australia

February, 2018

Certificate of Authorship/Originality

I certify that the work in this thesis has not been previously submitted for a degree nor has it been submitted as a part of the requirements for other degree except as fully acknowledged within the text.

I also certify that this thesis has been written by me. Any help that I have received in my research and in the preparation of the thesis itself has been fully acknowledged. In addition, I certify that all information sources and literature used are quoted in the thesis.

Production Note:
Signature removed prior to publication.

20/02/2018

ABSTRACT

Stimulated Brillouin scattering in nanophotonic waveguides and resonators

by

Sayyed Reza Mirnaziry

Dissertation directed by Associate Professor Christopher G. Poulton
School of Mathematical and Physical Sciences

In this work, we theoretically and numerically study Stimulated Brillouin Scattering (SBS) in integrated waveguides and resonators. We review SBS process by using coupled equations and determine a broad range of SBS parameters including SBS gain, opto-acoustic overlap, optical forces and power conversion between pump and Stokes waves. For numeric analysis, in addition to performing simulations we write appropriate codes and employ different iterative techniques as well as root finding methods to analyze SBS in interested configurations.

We study silicon-chalcogenide slot waveguides as a robust candidate to enhance SBS. We explain how constructive contribution of radiation pressure and electrostriction can increase the SBS gain in this structure. We also optimize the waveguide geometry and determine the optimum pump power as well as waveguide length as a function of SBS figure of merit, using our analytic expressions. We also show that putting a silica layer on top of the waveguide lead to a significant increase in the opto-acoustic overlaps and therefore, rise the SBS gain while reducing the impact of nonlinear losses in this structure.

We explore SBS in integrated racetrack ring resonators in both regimes of amplifying and lasing. We use analytic and numeric approaches to demonstrate pump and Stokes evolution in designed rings and through the output. In addition we an-

alyze the impact of nonlinear dispersion as well as thermal effects on SBS in rings. Finally, we determine the pump power to achieve Stokes amplification, the threshold pump power for lasing and the output Stokes power in the presence of linear and nonlinear optical losses.

Dedication

To Mudafi'an-i Haram who defended the Ahl al-Bayt (a) and fought against takfiri terrorists.

Acknowledgements

My deepest gratitude goes to my primary supervisor Dr. Christopher Poulton for his patience, motivation, enthusiasm and invaluable support throughout my PhD. He persistently tracked my progress and enlightened me with new ideas in our meetings. He was a meticulous supervisor who carefully read my manuscripts, especially this thesis, which greatly helped me improve its content. At many stages, where I had made mistakes in my analysis, he comprehensively assisted me in detecting them. I thank him for all his kind support.

I would like to thank my industrial supervisors, Dr. Benjamin Eggleton of Sydney University and Dr. Michael Steel of Macquarie University, for the patience, guidance, encouragement and advice they provided throughout my PhD. I also want to express my sincere gratitude to my co-supervisor Dr. Christian Wolff. His deep insights throughout this project assisted me through all stages of my research. I really appreciate the time he spent to go through my draft papers. I also thank Dr. Kokou Dossou at UTS for helping me in better understanding numerical techniques.

I am very indebted to these prestigious institutions for their support in this work; CUDOS for giving me this opportunity to collaborate with leading researchers and experimentalists and the University of Technology, Sydney for providing the facilities and supporting me throughout my PhD. I also acknowledge the financial support from the Industrial Doctoral Training Centre (IDTC) during my PhD, especially as they also provided training courses and annual conferences to establish contact between students and industries.

Last but not the least, I would like to thank my family in my language:

پدر و مادر عزیزم! بی تردید لحظه لحظه های زندگیم و ذره ذره موفقیت هایم مرهون فداکاری شما و بخشش سخاوتمندانه عمر بابرکتتان است. از خداوند بزرگ آرزوی سلامتی و عاقبت به خیری برایتان دارم. همسر عزیزم! همراهی تحسین برانگیزت را در دوران تحصیلم صمیمانه قدردانم. به وجودت افتخار، و در کنارت و سید هادی عزیزم احساس خوشبختی می کنم.

Sayyed Reza Mirnaziry

Sydney, Australia, 2017.

List of Publications

Journal Papers

1. Sayyed Reza Mirnaziry, Christian Wolff, MJ Steel, Benjamin J Eggleton, and Christopher G Poulton. Stimulated Brillouin scattering in silicon/chalcogenide slot waveguides. *Optics Express*, 24(5):4786–4800, 2016.
2. Sayyed Reza Mirnaziry, Christian Wolff, MJ Steel, Benjamin J Eggleton, and Christopher G Poulton. Stimulated Brillouin scattering in integrated ring resonators. *JOSA B*, 34(5):937–949, 2017.
3. Sayyed Reza Mirnaziry, Christian Wolff, Blair Morrison, MJ Steel, Benjamin J Eggleton, and Christopher G Poulton. Lasing in ring resonators by Stimulated Brillouin scattering in the presence of nonlinear loss. *Optics Express*, 25(20):23619–23633, 2017.

In addition to presentations in annual CUDOS workshops, a poster is presented from this project in the following conference

1. Sayyed Reza Mirnaziry, Christian Wolff, MJ Steel, Benjamin J Eggleton, and Christopher G Poulton. Stimulated Brillouin scattering in silicon-chalcogenide slot waveguides. *CLEO/Europe EQEC 2015 Conference*, Munich, Germany.

We note that Chapters 4, 5 and 6 are written according to papers 1, 2 and 3, respectively with small modifications.

Contents

List of Figures

Abbreviation

CW - Continuous Wave

SBS - Stimulated Brillouin Scattering

BSBS - Backward Stimulated Brillouin Scattering

SSA - Small Signal Approximation

TPA - Two Photon Absorption

FCA - Free Carrier Absorption

FCD - Free Carrier Dispersion

FSR - Free Spectral Range

SMF - Single Mode Fiber

Mid-IR - Mid- Infrared

WGR - Whispering Gallery Resonator

Chapter 1

Introduction

Nanophotonics, in which light is investigated in micro/nano scale structures wherein spatial confinement modifies propagation of waves, has today become a wide research area [1]. The propagation of electromagnetic energy in these structures — in the form of photons — can give rise to a mechanical response of a medium, resulting in mechanical waves in the form of phonons. The interaction between photons and phonons is weak in bulk materials, but it can become significant in nanophotonic waveguides. Recent progress in nanofabrication has resulted in a new class of waveguides and nanostructures in which opto-mechanical interactions are very large indeed. These new nano-optomechanical devices have a wide range of applications in sensing, new laser sources and in all-optical signal processing [2]

When a photon is scattered by a phonon, it changes its energy state, resulting in a small frequency shift. This is a type of inelastic scattering that was first predicted by Einstein in 1905, where he qualitatively demonstrated the possibility of changes in the energy level of incident photons to a material as a result of the non-zero temperature in the medium. Today, Brillouin and Raman scattering are the two major types of this inelastic scattering and have led to many studies since the 1920s. From the quantum mechanical point of view, Raman scattering occurs by optical phonons, while in Brillouin scattering acoustic phonons — which exist in a lower state of energy — play the role in scattering. There are however similarities between Brillouin and Raman scattering: In both, the power conversion is mediated via phonons. However, the Stokes shift in Brillouin is smaller by three orders of magnitude compared to that of Raman. Furthermore, the Brillouin linewidth is extremely narrow, with a typically bandwidth < 100 MHz [3].These differences result from the difference in the underlying interactions; In Raman, atoms experience out of phase vibrations in a lattice while they possess in phase movements in Brillouin scattering.

Brillouin scattering is the dominant light scattering mechanism which originates from interaction of light with acoustic waves in a propagating solid [3]. During Bril-

louin scattering, phonons are either created or annihilated [4]. In the absence of an initial Stokes wave, the phenomenon initiates from light interaction with thermal excitation of a propagation medium. This process is referred to as *spontaneous* Brillouin scattering, which leads to a weak light scattering. The scattering mechanism can increase remarkably by enhancing light intensity; this gives rise to temporary changes in the optical properties of the medium. The process is then referred to *Stimulated* Brillouin Scattering (SBS).

Observed first in 1964 by Chiao, SBS gained attentions a few years later in fiber telecommunication in which the phenomenon was known as a source of detrimental back-propagated reflections. Today, it is feasible to observe SBS in engineered chip scale structures with several order of magnitude stronger than SBS in hundreds of meters optical fiber. A broad range of applications, ranging from sensing [5] and filtering [6] to lasing [7] and signal amplifying [8] are investigated for SBS. There have been yet many unknown areas to explore in the future.

In the framework of this thesis, we investigate theoretically and numerically SBS in nanophotonic platforms. We study critical parameters which play a role in enhancing opto-acoustic interactions and propose configurations for tailoring SBS in nanophotonic waveguides. While following the established formulation of the phenomenon, we explore the power required for optimized Stokes results and by using analytic expressions we estimate the waveguide length for achieving maximum Stokes amplification. We also apply numeric techniques to study SBS in high Q-factor ring resonators. In addition, we evaluate a broad range of relevant quantities and parameters important to the SBS process and study the optical envelopes during the process, optical forces, opto-acoustic overlap and various nonlinear parameters in a number of multi-material structures.

We study SBS in slot waveguides consist of silicon and chalcogenide and examine the idea that by configuring a slot one can achieve enhancement in SBS interactions. The gain results for designed slot waveguides are comparable — and for some situations even higher — than the reported values for suspended silicon nanowires. We also investigate SBS in ring resonators for amplification and lasing application. We examine existing expressions for threshold power in the lasing regime with our derived expression and derive optimum powers to achieve maximum Stokes output in the presence of various linear and nonlinear losses.

1.1 Thesis Organization

This thesis is organized as follows. Chapter 2 provides the background to this work. We begin by describing the physics of SBS. This establishes the basic mechanism of the process and its conditions, types and parameters and physical phenomena associated to it. Then we review the literature and track the progress of SBS studies from early discoveries to the latest implementations. In addition, we look at recent applications of SBS which have been proposed for nanophotonic structures. In the last section we overview the current SBS theories and compare them in terms of their basic ideas and assumptions. We finish this chapter by reviewing the contribution to the SBS theory as demonstrated in this thesis.

In Chapter 2 we explain the theoretical framework of our approach used in studying SBS including principles, approximations and equations for pump and Stokes evolution through a waveguide. This chapter begins by describing the governing equations for optical and acoustic waves. Then opto-acoustic interactions are modeled as optical field perturbations occurring due to photoelasticity and waveguide boundary motion. The strength of the SBS process is then evaluated via a gain parameter which is quadratically dependent on the magnitude of light-sound overlap in a waveguide. Derivation of the overlap integral is also provided with other reported approaches for the purpose of verification. The remaining content of this chapter explains the evolution of the Stokes waves throughout a waveguide in the presence of linear and/or nonlinear losses. In this regard, fully numeric as well as analytic solutions (the latter applicable for small Stokes signals) are demonstrated for different situations.

In Chapter 3, the theories from Chapter 2 are applied to study SBS in designed silicon-chalcogenide slot waveguides. The multi-material structure of a slot benefits from a high refractive index material for optical confinement together with a mechanically flexible material for acoustic confinement; a situation which is not possible in a single material waveguide. These waveguides are thus potentially capable of enhancing SBS interactions. In addition, they are robust configurations, in comparison to suspended or semi-suspended waveguides suggested in the literature for SBS applications. Regarding slot waveguides, SBS gain and optical losses are evaluated for a range of slot and gap dimensions. Moreover, analytic expressions are derived to optimize the input pump and waveguide length in the presence of nonlinear losses.

Chapter 4 describes SBS in integrated racetrack ring resonators. Due to their high-Q factors, ring resonators enable considerable reduction of SBS device length in comparison to straight waveguides. We examine SBS in these structures for Stokes amplification. For this, we begin by describing the governing equations in the cavity and in the coupling region. Then design rules are given and conditions for Stokes amplification are derived for rings in the presence of linear and nonlinear losses. Maximum achievable amplification and threshold pump power required for initializing the process are obtained for rings with different losses, coupling and SBS figures of merit. In addition to a full numeric technique, analytic solutions for small signal approximations are demonstrated. Lastly, impact of nonlinear dispersion, temperature variation and ring length tolerances on the free spectral range and therefore, SBS performance, are evaluated.

Finally we focus on SBS lasing in integrated ring resonators in Chapter 5. Although the basic idea of SBS lasing has been demonstrated for fiber ring resonators, it has not been explored for chip scale waveguides. In this chapter, the physics of SBS lasing is studied in detail. We describe the conditions required for SBS lasing. Then, the output Stokes power is determined for rings with a realistic range of gain and loss parameters. In addition, in the presence of higher order nonlinearities, we find that there exists a finite power interval for lasing. We identify this interval and evaluate optimal pump power corresponding to the maximum Stokes output in the lasing regime. This chapter finishes by estimating the numerical calculation of the maximum Stokes power for rings with various loss and SBS figures of merit. In a concluding chapter we review the whole work and give some ideas for future studies.

Chapter 2

Background

Stimulated Brillouin Scattering (SBS) is a physical phenomenon in which light is scattered as a result of interaction between electromagnetic and acoustic waves in optical waveguides. During SBS two optical waves with a very small (typically GHz) frequency difference interfere and generate acoustic waves which make dynamic perturbations in optical properties of the propagation medium, usually due to the phenomenon of *photoelasticity*. These variations cause power to be transformed from the higher frequency (the "pump") to the lower frequency (the "Stokes"). The reflected Stokes in turn interferes with the pump, strengthening the acoustic wave and leading to additional transfer of optical energy from the pump to the Stokes. If the interaction between optical and acoustic waves is sufficiently strong then this process can be self-amplifying, resulting in a very large proportion of the pump power being reflected and a high-amplitude acoustic wave being generated within the waveguide. This mechanism is schematically shown in Fig. 2.1 where pump with frequency ω_1 and Stokes with frequency ω_2 first enter the waveguide (a). Then, acoustic vibrations are generated in the waveguide and propagate in the direction of the pump (b).

SBS can take place in four different situations: intra mode- forward, inter mode-forward, intra mode-backward and inter mode backward SBS. Within the intra mode SBS process pump and Stokes carry identical optical modes while in the inter mode coupling they have different optical modes. The optical and acoustic dispersion diagrams corresponding to these scenarios are shown in Fig. 2.2. In the SBS process the total energy and momentum are conserved. This requires that

$$\mathbf{q} = \boldsymbol{\beta}_1 - \boldsymbol{\beta}_2, \tag{2.1}$$

$$\Omega = \omega_1 - \omega_2, \tag{2.2}$$

where $\boldsymbol{\beta}_1$ and $\boldsymbol{\beta}_2$ and $\mathbf{q}$ are pump, Stokes and the acoustic wave vectors, respectively and Ω denotes acoustic angular frequency. In intra-mode forward SBS, $q = \frac{\Omega}{c} n_{\text{eff}}$ (c is the speed of light and n_{eff} effective mode index) is small, so that the mechanical

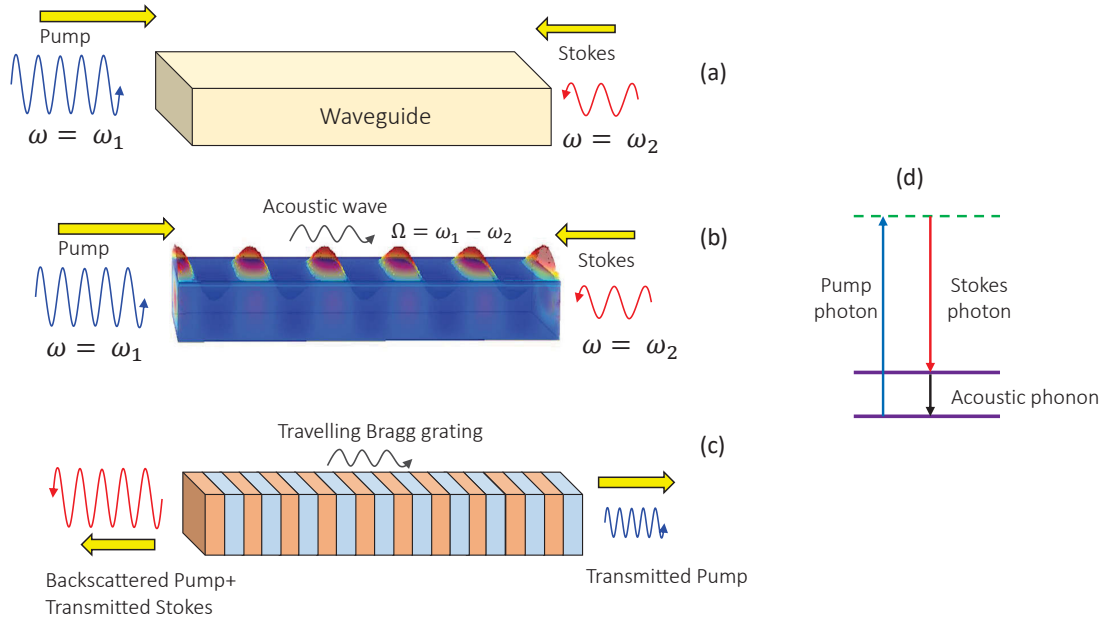

Figure 2.1 : (a) Schematic of the (Backward) SBS process. Pump and Stokes enter the waveguide in opposite (for BSBS) directions. (b) An acoustic wave is excited and starts propagation in the direction of pump. (c) In terms of optical properties, a traveling refractive index forms in the waveguide which causes pump scattering and red-shifting to the Stokes. (d) Energy diagram for Brillouin scattering. In SBS, pump photons loose energy by releasing an acoustic phonon, hence are converted to Stokes photons.

perturbations form a quasi-standing wave. In contrast, in intra-mode backward SBS, $q \approx 2|\boldsymbol{\beta}_1|$ as shown in Fig. 2.2.

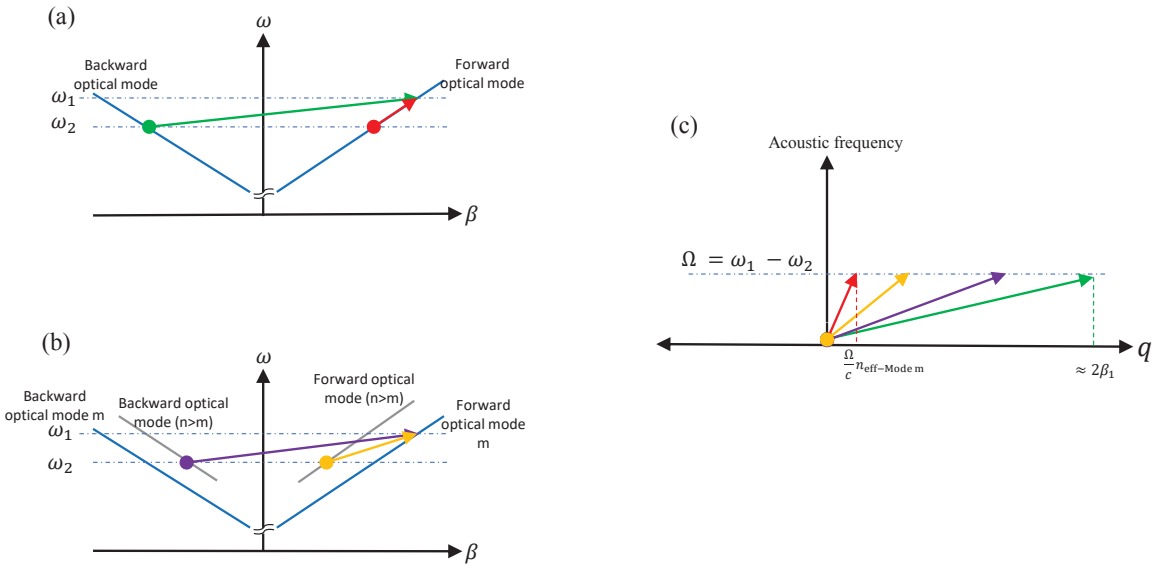

Figure 2.2 : Dispersion diagrams showing (a) intra mode (b) inter mode scenarios between optical modes in SBS. (c) is the acoustic dispersion diagram of the four situations shown in (a) and (b). In (a) an optical mode in forward and backward propagating are shown. In forward coupling (red vector), both pump and Stokes reside in the same mode. The acoustic wave vector resulting from this interaction —shown in (c)— is very small ($\approx \frac{\omega_1-\omega_2}{c} n_{\text{eff}}$). In contrast, in backward coupling (green vector) the acoustic wave vector is approximately $q = 2\beta$. In the case of inter mode coupling pump and Stokes carry different optical modes as shown in (b).

The strength of the SBS process is usually characterized by the gain g, which is measured in $\text{W}^{-1}\text{m}^{-1}$. The SBS gain is a key parameter in designing SBS-based devices as it is used to determine important quantities such as threshold pump power and net Stokes amplification. In single mode optical fibers g is weak, of the order of $10^{-2}\,\text{W}^{-1}\text{m}^{-1}$ [9]. This number increases by up to 6 orders of magnitude in nanoscale waveguides [10, 11]. The gain takes a Lorentzian shape over the frequency spectrum (Fig. 2.3) with a peak at phase-matched frequencies. The gain linewidth Γ_B depends on phonon lifetime τ ($\Gamma_\text{B} = \frac{1}{\tau}$), and is typically of the order of 10 – 100 MHz.

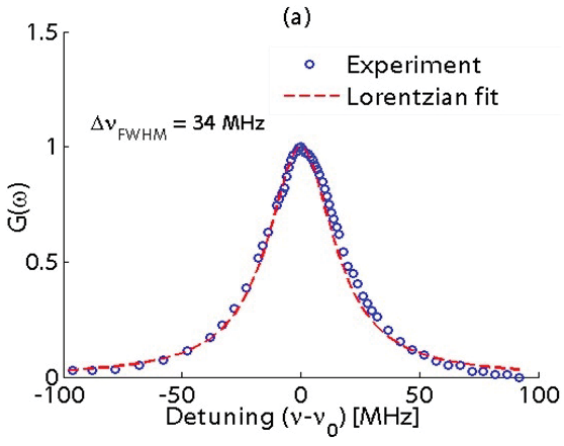

Figure 2.3 : The Lorentzian of the SBS gain measured in a chalcogenide rib waveguide. Picture from [12].

The waveguide material and waveguide geometry together play an important role in tailoring SBS interactions. With regarding to the former, a potential material in a SBS device should provide both optical and acoustic confinement to ensure sufficient opto-acoustic overlap. In terms of optical confinement, high refractive index materials are ideal. Moreover, for acoustic confinement, a mechanically flexible material is required. We note that these properties for a material are in comparison to the surrounding materials; a material might have a moderate refractive index for instance but must have the highest refractive index in a configuration to confine the light. Materials such as silicon, germanium and chalcogenide glasses are promising candidates to be used in SBS devices. In practice, it is hard to find all desirable optical and acoustic properties in a single material [2, 13]. Silicon for instance, has a high refractive index but is a very stiff material (longitudinal sound velocity in Si is $v = 8433$ m/s). Therefore, if it is fabricated on a silica substrate which is less-stiff — with $v = 5960$ m/s longitudinal —, acoustic waves cannot be confined in silicon and leak to the substrate. There are other types of limitations in selecting a material; Germanium for instance has even higher refractive index ($n \approx 4$) than silicon and smaller stiffness [14]. However, due to its small energy band gap (0.67 eV), it is not suitable for SBS in near-IR because band to band transitions lead to extremely large linear losses [8]. Finally, the guiding material must have a non-negligible electrostrictive response, provided that electrostriction — and not radiation pressure (see Section 3.8.2) — is the dominant opto-mechanical mechanism.

Beside material properties, strong SBS in chip scale waveguides requires the correct geometry. While in quasi-bulk waveguides, optical and acoustic waves propagate longitudinally and SBS is mainly originated from electrostriction, in integrated waveguides, optical and acoustic waves are confined and propagate in modes which range from pure longitudinal to pure transverse. Consequently, the strength of the opto-acoustic overlap depends on the mode profiles. In addition, a carefully designed geometry can compensate weak material properties of a configuration and therefore, enhance the overlap between light and sound. Finally, to be able to amplify Stokes in the presence of optical nonlinearities, the waveguide length must be optimized; otherwise, nonlinear optical losses (see Section 3.11) can eliminate all obtained Stokes gain.

2.1 Early work on SBS

The idea of Brillouin scattering was first studied by Leon Brillouin who explained the effect of excited acoustic waves on inelastic light scattering. The process was also reported by Mandelstam, a few years after Brillouin's paper, therefore it is also referred as Brillouin-Mandelstam scattering [15]. Soon after, many efforts were devoted to observe the phenomenon [16]. The first report of observation of stimulated Brillouin scattering dated after the laser invention and was made by Chiao who detected intensified acoustic vibrations in quartz and sapphire by emission of a laser beam [17]. Since these early experiments, SBS has been extensively investigated in different states of matter including liquids [18, 19], gases [20] and waveguide devices [21].

The development of optical fiber for telecommunications opened a new window in exploring nonlinear effects including four-wave mixing, self-phase modulation as well as stimulated Raman and Brillouin scattering [22]. In contrast to bulk Brillouin scattering experiments, the confined geometry of fiber showed that the SBS spectrum is influenced by excited acoustic eigenmodes, rather than by bulk acoustic waves. In low loss optical fibers SBS was shown to have a detrimental effect in optical power transfer [21]. This was because SBS causes backward scattered Stokes which grows exponentially with the input signal power. Although the SBS gain is weak in fibers, light often travels long distances — tens of kilometers —, thus the backward Stokes becomes considerable [23]. Both backward [24] and forward [21] SBS were explored in optical fibers. These processes found applications in sensing [25], lasing [26] and amplifying [27].

2.2 SBS in integrated waveguides

In the past decade and along with tremendous progress in nanotechnology and fabrication techniques, there has been a strong interest toward tailoring SBS in nanophotonic structures. New classes of ultra-efficient opto-mechanical device have been proposed to manipulate hypersonic acoustic waves and to enhance precise interactions between sound and light. In Single Mode Fibers (SMF), the difference between acoustic properties of fiber core and cladding is very small. Therefore, acoustic power exists in both area and waveguide medium behave like a quasi bulk glass. Consequently, SBS is dominated by longitudinal quasi-plane waves [28]. In contrast, in waveguides with engineered cross sections — such as Photonic Crystal Fibers (PCFs), tight spacial confinement leads to a complex interaction between optical and acoustic waves [29].

SBS research on PCFs has been a key step toward transition from a quasi bulk waveguide — such as SMF — to a confined micro structure. PCFs are composed of single glass and air holes through the fiber cross section which have different types — depending on the core and holes geometry, position and material — and have been subject to a number of SBS researches [30, 31, 32]. In air glass PCFs with large air-filling fractions and micrometer-size glass cores, the resulting acoustic modes contain proportions of both shear and longitudinal strain which lead to a range of hybrid modes with different dispersion relations [28]. Dainese et al. showed that PCFs support phononic bandgaps which allows these waveguides to transversally confine of acoustic modes [28]. The SBS gain in these structures are remarkable; chalcogenide ($Ge_{15}Sb_{20}S_{65}$) PCFs have shown the SBS gain of $8 \times 10^{-10}\,\mathrm{mW}^{-1}$ which is about 100 times larges than those reported for silica fibers [33].

The complex dynamics of acoustic waves and their localized mode distributions through the PCF cross section lead to an increased SBS threshold in infrared wavelengths. This is mainly because acoustic modes exist in the whole cladding while optical modes are confined in the waveguide core. Thus, the overlap between optical and acoustic modes is reduced. Significantly large thresholds up to a factor of five higher than those calculated theoretically have been reported in PCFs in infrared regime [34]. Due to their SBS threshold features, PCFs are interesting in applications — such as in quantum information experiments — which require high levels of Forward SBS suppression [35]. PCFs are also examined for realization of slow light via SBS [36].

A serious setback in reducing the size of previous SBS devices to chip scale structures was their small SBS gains. To compensate this, SMFs hundreds of meters long was required to be able to observe the Stokes power [37]. In PCFs the length is reduced to a few meters [35, 9] as the SBS gain is improved. In nanoscale photonic waveguides, however, the boundary force of radiation pressure scales up remarkably. This was unlike previous interpretations which attributed the strength of SBS as arising entirely from material photoelasticity. In this regard, a broad range of structures such as nanorods [10], rib waveguides [12], slot waveguides [13] were investigated. Early studies on SBS in chip scale structures aimed to determine the SBS gain of translationally invariant waveguides. Features such as impact of optical forces, in particular radiation pressure and its contribution to the overall gain, in comparison to other important optical forces were explored in selected waveguides [38, 10, 39]; In [40] Rakich.et al showed that while electrostrictive force increases in high refractive index waveguides, it can constructively or destructively interfere with radiation pressure, thus making a considerable change in the SBS gain; a situation which requires engineering of the waveguide cross-section. Figure (2.4) shows some of the integrated configurations studied for SBS purposes.

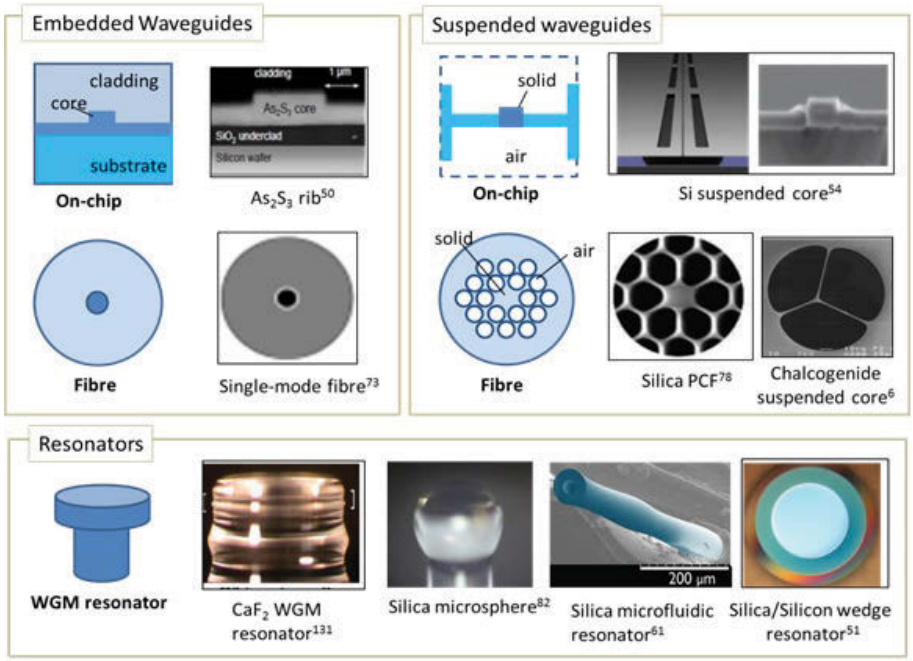

Figure 2.4 : Waveguide geometries for harnessing SBS in chip-scale. Picture from [2].

First observation of on-chip SBS was reported by Pant et al. who demonstrated

SBS in a chalcogenide rib waveguide of 7 cm long [12]. They measured the SBS gain of $7.15 \times 10^{-8}\,\mathrm{mW}^{-1}$, a value which is the same order of magnitude of the gain reported for PCF. Soon after, the first demonstration of cascaded on-chip SBS capable of generating three Stokes order in the same waveguide but with the length 4 cm were reported by the same group. Because of their large waveguide cross section ($4\,\mu\mathrm{m} \times 850\,\mathrm{nm}$), electrostriction is the dominant mechanism to generate SBS gain in these structures [41].

Currently both forward and backward SBS are under investigation at the nanoscale; in the forward process, interesting features such as long phonon lifetime and easy generation are deployed to demonstrate a number of applications, including Brillouin scattering induced transparency [42], Brillouin cooling [43] and lasing[44]. In addition, through FSBS, multiple Stokes and ani Stokes lines (cascading) are usually generated. A comprehensive study of the process is proposed in [45] which will be reviewed in the next section.

In order to increase the opto-acoustic overlap for enhancing SBS gain in nanoscale waveguides, various ideas are proposed. Among them, suspending a waveguide enables compensating the weakness in acoustic confinement in waveguides. In 2014, Van Laer *et al.* reported SBS in a silicon nanowire with $450\,\mathrm{nm} \times 230\,\mathrm{nm}$ fabricated on a tiny pillar of 15 nm (Fig. 2.5) [46]. The tiny pillar reduced the escape of the phonons to the substrate, hence providing acoustic confinement. A huge coupling between light and acoustic waves due to constructive interference of electrostriction and radiation pressure resulted in peak SBS gain of $3055\,\mathrm{W}^{-1}\mathrm{m}^{-1}$ with the measured Brillouin linewidth of 40 MHz. Later a suspended silicon rib waveguides were examined in which Stokes could be amplified up to 5 dB — comparing with 0.5 dB in Van Laer structure —[47].

Research on SBS nonlinearities in silicon waveguides remained active; a fundamental challenge in silicon is nonlinear optical loss mainly due to Two Photon Absorption (TPA) and Free Carrier Absorption (FCA) at near infrared regime, which can totally neglect the SBS gain. To analyze the impact of nonlinear losses, Wolff *et al.* introduced a new formulation based on coupled mode theory to include the third and fifth order nonlinearities in SBS [48]. In addition, the group derived a SBS figure of merit, a quantity to evaluate whether the SBS gain is sufficient to compensate nonlinear loss in order to achieve Stokes amplification. The new formulation provides theoretical tools to determine optimum waveguide length as well as

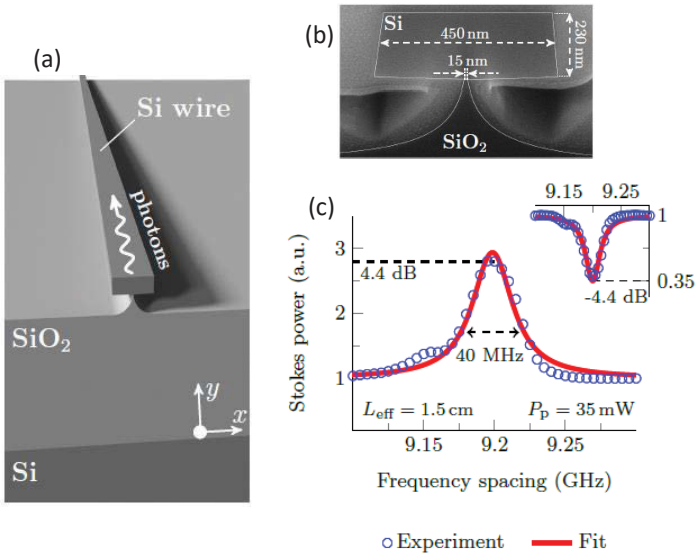

Figure 2.5 : (a) A silicon nanowire on a tiny pillar with cross section dimensions shown in (b). (c) The Lorentzian SBS gain of the structure. The inset shows the profile of depleted ani-Stokes photons. Picture from [46].

optical power required for maximum Stokes amplification [48, 13] and is outlined in Chapter 3.

SBS has also gained attention in integrated racetrack ring resonators [8, 49, 50]. Although SBS in long fiber ring resonators was studied extensively for lasing purposes [26, 51, 52], tailoring SBS in a high Q-factor resonator and in a small footprint enables considerable reduction of the optimal waveguide length while keeping the output Stokes high. A comprehensive theoretical study of SBS in integrated ring resonators as a Stokes amplifier is in Chapter 5 of this thesis where various aspects of SBS, including designing, Stokes amplification and impact of variation of Free Spectral Range (FSR) on the process are demonstrated. Integrated Brillouin lasers have also been explored; recently a silicon Brillouin laser was demonstrated in a racetrack ring consisting of a 4.576cm suspended rib waveguide which required threshold input pump power of 10.9 mW and compressed the Stokes bandwidth to 20kHz [53]. An extensive theoretical exploration of SBS lasers in ring resonators is given in Chapter 6.

In addition to racetrack ring resonators, micro-scale Whispering Gallery Res-

onators (WGR) have proven great potential in enhancing the SBS gain. In microsphere WGR, giant SBS gain of $4 \times 10^6\,\mathrm{W^{-1}m^{-1}}$ has been measured which shows the impact of large values of optical forces generated on WGR boundaries [54]. Other types of high Q factor resonators including micro disks [55] and micro rods [56] have been proposed for SBS applications.

2.3 Applications

A broad range of applications have been explored since the observation of SBS; Lasing, amplifying and sensing, light storing, microwave photonic processing and frequency comb generation are among those reported so far. We here review some of the SBS applications that have recently gained attention in nanophotonic waveguides.

2.3.1 SBS microwave filters

Microwave Photonic Filters (MPF) are potentially one of key components of all-optical signal processing circuits in future mobile communications technology. Microwave photonics requires narrow linewidth filters that are widely tunable and resistant to electromagnetic interference [57]. In this regard, SBS is found to have great potential to realize these filters.

A basic scheme of a SBS MPF is shown in Fig. 2.6. The microwave signal is first phase modulated with an optical frequency (ω) as shown in Fig. 2.6(a). This results in two sidebands with identical frequency but unequal magnitudes. SBS with a gain spectrum peak equal to a selected frequency is then applied on the weaker sideband to enhance its magnitude and make it equal as the amplitude in the stronger sideband(Fig. 2.6(b)). Next, the sidebands are sent for photodetection (Fig. 2.6(c)). Due to a destructive interference between the two sidebands at the SBS peak gain frequency, the microwave signal at the gain resonance is highly suppressed(Fig. 2.6(d)) [58]. MPFs based on SBS were first demonstrated in optical fibers [59]. Then, moving to chip scale, the idea has been recently examined in chalcogenide rib waveguide [60, 58, 61].

2.3.2 SBS lasers

Brillouin lasers were initially demonstrated for optical fibers [52, 62]. Due to their narrow linewidth, fiber ring lasers based on SBS became subject for a number

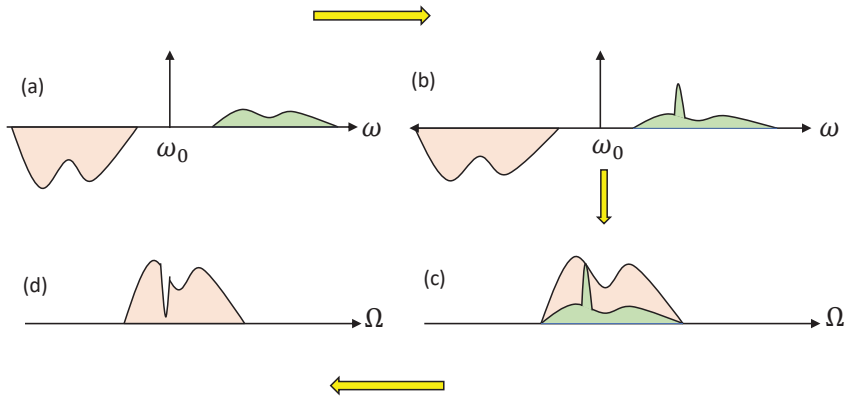

Figure 2.6 : (a) Dual side-modulated optical signal as in input of the filter, containing out of phase but unequal sides. (b) SBS gain amplifies the weaker side at the gain resonance to reach the same amplitude as in the strong side. (c) The modified signal is sent to a high speed photodetector for direct detection. (d) At the frequency where amplification has occurred, sideband have equal amplitude but opposite signs. Therefore, they cancel each other and leads to a significant suppression.

of investigations to realize linewidth narrowing, microwave frequency generation, etc [63]. In chip scale footprints, Brillouin lasers possess low frequency noise which have been studied in microcavities and racetrack rings to be used in precision spectroscopy [64]. We will review the physics of SBS lasers in single ring resonators in chapter 6.

2.3.3 Optical data storage

Over the recent decade, research on optical data storage in modern optical networks has remarkably increased. The use of photon-phonon interactions in storing light was first studied in optical fibers [65]. Different techniques including performing spectral holography of femto-second pulses [66] and employing Electromagnetically Induced Transparency (EIT) have been extensively explored [67, 68]. More recently attempts have shifted toward realizing light storage via SBS in integrated waveguides [69]. In this regard, SBS has proven the capacity to store light on a timescale below the lifetime of the acoustic phonons propagated in a waveguide. The method is shown schematically in Fig. 2.7. The optical data (pump) and a write signal (Stokes) enter a waveguide from opposite directions (Fig. 2.7A). Due to

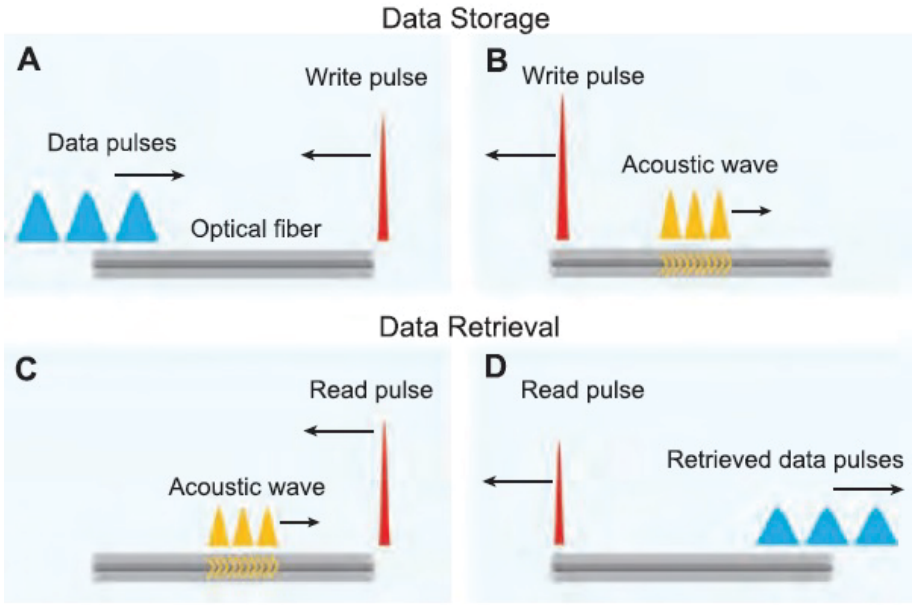

Figure 2.7 : Data storage process in an optical fiber. (a) A short write pulse acting as Stokes seed and interfere with the data pulses. (b) Through the SBS process, data pulse is depleted, write pulse is enhanced and an acoustic wave is generated which travels opposite to the write pulse. (c)A read pulse enters and (d) retrieve the data pulse Credit: Z. Zhu [65].

SBS, the pump is depleted and generates acoustic waves propagating in the direction of pump (Fig. 2.7B). Next, on a timescale below the phonon decay time, a read pulse — which is identical to the write pulse — enters from the same direction as the write pulse (Fig. 2.7 C). This time the traveling acoustic data is depleted and transfer its energy to the read pulse, thus retrieve the data, propagating in its initial direction (Fig. 2.7 D).

2.3.4 All optical isolator

Non-reciprocal devices are components which allow optical fields to propagate only in one direction, and have potential to suppress noise and backscattered light in integrated photonic devices [70, 71]. SBS has been proposed to realize these devices [71, 72] because in contrast to the common Faraday rotation approach in magnetic materials, it can be easily implemented in chip-scale waveguides. SBS-based isolators have also been demonstrated in optical fibers. The simple idea is to break the Lorentz reciprocity by using the phase matching conditions for SBS; light that does not satisfy the momentum conservation can propagate with no change, and light that is phased-matched creates phonon-photon couplings via SBS, hence looses energy.

2.4 Theory of SBS in optical waveguides and context of this thesis

In the early studies of SBS, pump, Stokes and acoustic waves were all assumed to be plane waves. On the optical side, the governing equation is the electromagnetic equation and optical field consists of the summation of pump and Stokes fields. On the acoustic side, the dynamic equation of motion is applied which is an inhomogeneous partial differential equation due to the presence of the electrostrictive force. Next, the coupled mode equations — which describe slowly varying optical envelopes as well as density variations — are derived from the governing wave equations [73, 74].

A common approximation in the wave analysis consists of neglecting the spatial derivation of material density along the propagation direction. This is valid as long as phonon lifetime is very small — in the range of nanosecond. In addition, SBS is usually studied in the steady state; those terms with time derivatives drop from the derived coupled equations. The acoustic wave is also assumed to be longitudinal

in BSBS. Moreover, among all components of the photoelastic tensor, only p_{12} — which is relates the interaction of longitudinal acoustic waves to the transversed components of interfered optical fields — is assumed to contribute to peak SBS gain.

The plane wave approximation in step index fibers provides a reasonably accurate estimation for the evolution of optical and acoustic waves during SBS. This is due to the quasi-bulk property of the fiber for SBS interactions. However, an accurate analysis requires including the guiding properties of a propagation medium in the equations. In more complex configurations such as graded index fibers, plane wave approximation results in substantial overestimation of the SBS gain as well as the threshold pump power (the pump power needed to achieve Stokes amplification). In addition, in engineered geometries such as PCFs and nanoscale waveguides, the optical and acoustic modes are remarkably influenced by the waveguide configuration, therefore opto-acoustic overlaps are very different to the plane wave approximation. In these cases, one has to compute the both optical and acoustic modes, to analyze the SBS process; an approach that we refer to as the *modal approach*.

The modal approach used in studying SBS in integrated photonic waveguides differs from plane wave approximations in several aspects; Obviously, modes should now be computed. But a major discrepancy between the two approaches also appears in defining and calculating the SBS gain. In general in all methods, the gain g is represented as $g = G|Q|^2\mathcal{L}(\Omega)$ where $G|Q|^2$ represents the maximum achievable SBS gain of the device, in which Q denotes the overlap integral between optical and acoustic waves and $\mathcal{L}(\Omega)$ accounts for the spectral distribution of the gain. In the early approach — which is applicable in the bulk — $Q = 1$ because the optical and acoustic fields do not vary through waveguide cross section. In the early modal approximations — applicable in quasi-bulk media such as step index fibers —, Q was usually defined as the overlap integral of squared optical mode and acoustic mode. In addition, G in these cases was calculated similarly; in deriving its expression only longitudinal components of electrostrictive stress contribute as it is the dominant stress component (i.e. $G = F(p_{12})$). With regard to the Q — which evaluates the strength of opto-acoustic couplings —, there are two approaches in the literature for incorporating SBS interactions in the overlap integral. We describe them as follows.

The first treatment relies on determining optical forces acting on the waveguide, in order to evaluate the overlap integral and consequently, the SBS gain. As de-

scribed in the previous sections there are two major optical forces due to electrostriction and radiation pressure. Electrostriction appears on both core and waveguide boundaries (the latter is usually referred to electrostrictive boundary force) while radiation pressure act only on boundaries. Then, the overlap integral is the dot product of the optical forces and acoustic displacement fields integrated over the waveguide cross-section.

The second and more recent approach describes SBS as an energy transfer occurring between pump and Stokes due to optical field perturbations. The optical field distortions are the results of mechanical displacement in a waveguide interior and on its boundaries. Only those harmonics of perturbed fields which satisfy SBS phase matching conditions interact in the process. Unlike the previous approach, optical forces are not explicitly calculated, although the overlap integral again consists of contributions from electrostriction and radiation pressure. Therefore the advantage of this approach is avoiding confusion in expressions for optical forces.

Research on SBS theory is not limited to determining the gain. The gain quantity is not sufficient to determine the quantity of output Stokes power. This is because only the impact of linear acoustic loss is included in the current expression of the gain. The critical quantity of Stokes power — which is observable and measurable — depends not only on the SBS gain, but on the optical loss and the length of a waveguide. This is in particular important when SBS occurs in waveguides with higher order nonlinearities. For instance, recent studies have shown large values of gain in silicon nanowires [48] however, in addition to large gain, there exists significant nonlinear loss due to TPA and FCA-induced by TPA, and this should be considered in evaluating SBS performance. To study these effects, coupled mode equations are modified by including third and fifth order nonlinear losses. A full description of derivations are covered in next chapter.

The *Hamiltonian approach* is another way for studying SBS in which quantum theory is employed to provide a microscopic picture of the process. For this, a proper Hamiltonian is constructed and quantized to cover both creation and annihilation operators of photons and phonons using appropriated operators [75, 45, 76, 77]. Although the approach is not new [77], it has recently gained attention because it uses the thermodynamic arguments to describe coupling terms while avoiding explicit expressions for optical forces [75]. SBS quantum studies are currently developing to better understand mechanisms such as Forward SBS [45] as well as connections

between SBS process and cavity optomechanics [76]. In the past, optomechanics — which demonstrates phenomena corresponding to the mutual interactions between light and mechanical motions [78] —, relied mostly on the effect of radiation pressure while SBS in the bulk was mainly due to the electrostriction [76]. However, in both there exist similar concepts such as gain. Today, these area are becoming closer in nanoscale waveguides and their demonstrations are connecting via quantum formulations.

In this thesis, we follow the wave approach in [48] for exploring SBS in both forward and backward processes. For this, we employ the coupled mode equations and describe evolution of pump and Stokes in a number of platforms and in the presence of linear and nonlinear losses and dispersion. In terms of the theory, we improve analytic expressions for optimizing the input pump power and also waveguide length. We implement this approach to study SBS in integrated racetrack ring resonators, in the different regimes of amplification and lasing. In terms of amplification, features such as design and optimization of physical and optical parameters are demonstrated to enhance SBS nonlinearities. Other aspects such as interfering parameters including variation of free spectral range occurred by optical nonlinearities or thermal effects are covered. In terms of SBS lasing, we demonstrate the condition of lasing in the presence of nonlinear loss and evaluate pump and Stokes for a range of SBS related parameters. Full details of the contribution are given at the beginning of each chapter.

Chapter 3

Theory

In this chapter, we review the fundamentals of SBS interactions in optical waveguides. This analysis enables us to gain a comprehensive picture of relevant mechanisms which determine the strength of the SBS gain and power transmission from pump to the Stokes. The physical concepts and expressions introduced in this chapter will be used repeatedly in next chapters. Among the literature used in explaining the theoretical aspects of SBS, we in particular use [79] to establish the notation and also to describe the SBS parameters.

3.1 Initial assumptions

SBS arises from the interaction between two optical waves with a frequency difference of a few GHz. From energy conservation, the light (pump) with higher frequency (ω_1) and the light (Stokes) with the lower frequency (ω_2) satisfy the phase-matching conditions as in Eq. (2.1)

$$\mathbf{q} = \boldsymbol{\beta}_1 - \boldsymbol{\beta}_2$$

To understand the coupling between pump and Stokes we consider an infinite waveguide aligned along the z axis as shown in Fig. 3.1. The waveguide material and cross-section along the z axis are assumed to be translationally invariant. Moreover, we assume that waveguide materials are purely dielectric ($\mu_\mathrm{r} = 1$).

3.2 Electromagnetic waves in waveguides

We start with the Maxwell equations which characterize the variation of the optical modes as they propagate in a waveguide:

$$\nabla \times \mathbf{E} = -\mu_0 \frac{\partial \mathbf{H}}{\partial t}, \tag{3.1}$$

$$\nabla \times \mathbf{H} = \frac{\partial \mathbf{D}}{\partial t}, \tag{3.2}$$

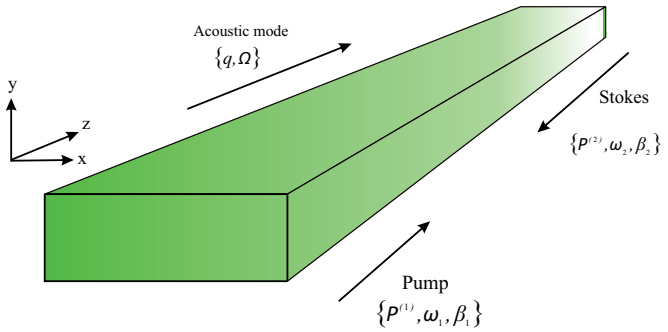

Figure 3.1 : Schematic of translationally invariant waveguide along z. Pump, Stokes and acoustic waves with their parameters and direction — in BSBS — are shown.

where μ_0 is the permeability; $\mathbf{E}$, $\mathbf{H}$ and $\mathbf{D}$ are electric, magnetic and optical displacement fields, respectively. Substituting Eq. (3.2) into Eq. (3.1) leads to the full vector electromagnetic wave equation

$$\nabla \times \nabla \times \mathbf{E} + \mu_0 \frac{\partial^2 \mathbf{D}}{\partial t^2} = \mathbf{0}. \tag{3.3}$$

in a source free nonmagnetic medium. We can split each of the fields into a combination of pump and Stokes waves,

$$\mathbf{E} = \mathbf{E}^{(1)} + \mathbf{E}^{(2)}, \tag{3.4}$$

$$\mathbf{H} = \mathbf{H}^{(1)} + \mathbf{H}^{(2)}, \tag{3.5}$$

$$\mathbf{D} = \mathbf{D}^{(1)} + \mathbf{D}^{(2)}. \tag{3.6}$$

in which the superscripts 1 and 2 refer to pump and Stokes, respectively. We now assume that the electric field varies slowly over an optical time scale

$$\mathbf{E}^{(\mathrm{i})} = \bar{\mathbf{E}}^{(i)} + c.c \tag{3.7}$$

$$= A^{(\mathrm{i})}(z,t)\tilde{\mathbf{e}}^{(\mathrm{i})}(x,y,z,t) + c.c, \tag{3.8}$$

where $i = 1, 2$, $A^{(\mathrm{i})}$ is the slowly varying modal envelope (i.e. $A^{(\mathrm{i})}$ varies slowly over the time scale and wavelength of an optical cycle) and $c.c$ is the complex conjugate term. $\tilde{\mathbf{e}}^{(\mathrm{i})}$ denotes the optical mode which is the eigensolution of Maxwell equations — while applying the appropriate electromagnetic boundary conditions

on waveguide interfaces — in which $\partial_z = i\beta_i$ (i = 1,2). In the case of time harmonic fields, the mode expression can be further expanded as

$$\tilde{\mathbf{e}}^{(\mathrm{i})}(x,y,z,t) = \hat{\mathbf{e}}^{(\mathrm{i})}(x,y)e^{i\beta_{\mathrm{i}}z - i\omega_{\mathrm{i}}t}, \tag{3.9}$$

where $\hat{\mathbf{e}}^{(\mathrm{i})}(x,y)$ is the cross sectional mode profile; β_{i} is the optical propagation constant which depending on the optical mode propagation direction, can be positive or negative and ω_{i} is the angular frequency. Modes represent spatial distribution of electric and magnetic fields and $\tilde{\mathbf{e}}^{(\mathrm{i})}$ obeys the equation.

$$(\nabla_\perp + i\beta_i\hat{z}) \times (\nabla_\perp + i\beta_i\hat{z}) \times \hat{\mathbf{e}}^{(\mathrm{i})} - \frac{\omega_{\mathrm{i}}^2}{c^2}\hat{\mathbf{d}}^{(\mathrm{i})} = 0, \tag{3.10}$$

where $\hat{\mathbf{d}}^{(\mathrm{i})}$ is the displacement field of mode i and c is the speed of light in free space.

The pump and Stokes eigenmode power and energy density along the propagation direction z are denoted by

$$\mathcal{P}^{(\mathrm{i})} = 2\int \mathrm{Re}[\tilde{\mathbf{e}}^{(\mathrm{i})} \times [\tilde{\mathbf{h}}^{(\mathrm{i})}]^*]\ ds, \quad [\mathrm{W}] \tag{3.11}$$

$$\mathcal{E}^{(i)} = 2\int \tilde{\mathbf{e}}^{(\mathrm{i})}.[\tilde{\mathbf{d}}^{(\mathrm{i})}]^*\ ds \quad [\mathrm{J/m}]. \tag{3.12}$$

The relation between the optical power and energy density is expressed by

$$\mathcal{P}^{(\mathrm{i})} = v_g^{(\mathrm{i})}\mathcal{E}^{(i)}, \tag{3.13}$$

where $v_g^{(\mathrm{i})}$ is the optical group velocity. Now the optical pump (Stokes) powers can be represented as

$$P^{(i)} = |A^{(i)}|^2\mathcal{P}^{(i)}. \tag{3.14}$$

3.3 Acoustic waves in waveguides

Similar to the approach we described for optical modes, the acoustic displacement field $\mathbf{U}$ can be expressed by

$$\mathbf{U} = b(z,t)\tilde{\mathbf{u}}(x,y,z,t) + c.c, \tag{3.15}$$

where $b(z,t)$ is the acoustic envelope and $\tilde{\mathbf{u}}$ the acoustic mode. The displacement field is a continuous variable in a solid. It describes the mechanical vibrations within a waveguide.

A waveguide is said to be *deformed* when the waveguide particles — assumed to be infinitely small volumes in the propagation medium — are displaced relative to each other. While the displacement field shows the particles' vibration pattern, it does not give a complete picture of the deformations in a waveguide. In the case of rigid rotations, for instance, a waveguide is not deformed although the displacement field is nonzero. Deformation is the result of body or external forces. The appropriate quantity which characterizes deformation is mechanical Strain. Strain describes the relative displacement of the particles from an equilibrium position and is expressed by

$$S_{ij} = \frac{1}{2}(\partial_i U_j + \partial_j U_i), \tag{3.16}$$

in which $i, j \in \{x, y, z\}$. This is the linearized expression of strain applicable for rigid materials [80]. Another important parameter — which is closely related to strain — is stress. Stress describes the internal force applied to each particle from the neighboring particles. The dynamics of any elastic problem is governed by the following equation which plays the same role as Maxwell equations

$$\rho\partial_t^2\mathbf{U} = \nabla.\mathbf{T} + \mathbf{F}, \tag{3.17}$$

where $\mathbf{T}$ is the stress tensor, ρ is mass density and $\mathbf{F}$ is the external body force. The divergence of the stress $(\nabla.\mathbf{T})$ is denoted by

$$(\nabla.\mathbf{T})_i = \partial_j T_{ij}, \tag{3.18}$$

where $\{i, j\} \in \{x, y, z\}$. According to Hooke's law stress is linearly proportional to strain via

$$\mathbf{T} = \mathbf{c} : \mathbf{S} + \eta : \partial_t\mathbf{S}, \tag{3.19}$$

where $\mathbf{c}$ and η are tensors of stiffness and viscosity, respectively. The double dot denotes the product of forth rank and a second rank tensor$((\mathbf{c} : \mathbf{S})_{ij} = \sum_{kl} c_{ijkl}S_{kl})$. Equation (3.19) can be written in terms of the stress components

$$T_{ij} = c_{ijkl}S_{kl} + \eta_{ijkl}\partial_t S_{kl}, \tag{3.20}$$

where $\{i, j, k, l\} \in \{x, y, z\}$. The stiffness tensor components c_{ijkl} are small in easily deformed materials while in rigid ones they take large values. In practice, many of the stiffness components are not independent. Due to the symmetry of strain and stress tensor

$$c_{ijkl} = c_{jikl} = c_{ijlk} = c_{klij}, \tag{3.21}$$

which reduces the number of independent stiffness constants to 21 which is the most number for anisotropic linear acoustic materials. However, as we shall see this can be further reduced to 2 isotropic materials.

Now using the acoustic displacement and strain quantities, the dynamic equation of acoustic motion can be expressed by [80]

$$\rho\partial_t^2 U_i = \sum_{jkl} \partial_j (c_{ijkl} S_{kl} + \eta_{ijkl} \partial_t S_{kl}) + F_i, \tag{3.22}$$

where $\{i, j, k, l\} \in \{x, y, z\}$. Similar to the optical modes, in the case of time harmonic fields, $\tilde{\mathbf{u}}$ can be expressed by

$$\tilde{\mathbf{u}}(x, y, z, t) = \hat{\mathbf{u}}(x, y) e^{iqz - i\Omega t}, \tag{3.23}$$

where $\hat{\mathbf{u}}$ is a basis function which shows the cross sectional mode profile; q acoustic propagation constant and Ω acoustic frequency. The term $\hat{\mathbf{u}}$ is the solution of the 2D eigenmode problem (i.e. solution of Eq. (3.22) assuming $b(z, t) = 1$ for a time harmonic acoustic wave in a lossless medium) [79]

$$\rho\Omega^2 \hat{\mathbf{u}} + \sum_{jkl} (\nabla_\perp + iq\hat{z}) c_{ijkl} (\nabla_\perp + iq\hat{z})_k \hat{\mathbf{u}}_l = 0, \tag{3.24}$$

where $\nabla_\perp$ acts on perpendicular plain to the propagation direction (i.e. $\nabla_\perp \equiv \partial_x \hat{x} + \partial_y \hat{y}$). The indices $\{i, j, k, l\} \in \{x, y, z\}$.

3.3.1 Voigt notation

The complexity of working with forth rank tensors can be alleviated by using the symmetry properties, shown in Eq. (3.21). By using the abbreviated subscript notation, Eq. (3.20) can be written in the form of

$$T_I = c_{IJ} S_J + \eta_{IJ} \partial_t S_J, \tag{3.25}$$

where I (J) is

I	ij
1	xx
2	yy
3	zz
4	yz, zy
5	xz, zx
6	xy, yx

In the case of cubic or isotropic materials, the acoustic response of the medium is identical in three coordinate plains xy xz and yz [80]. Using the notation described in Eq. (3.25)

$$c_{11} = c_{22} = c_{33}, \tag{3.26}$$

$$c_{12} = c_{13} = c_{23}. \tag{3.27}$$

This equality reduces the number of stiffness tensor variables to only three (in cubic)/ two (in isotropic) variables. Both tensors $\mathbf{c}$ and η are properly tabulated for a broad range of materials in the literature (see for example [80, 14]).

3.4 Acoustic waves: solution

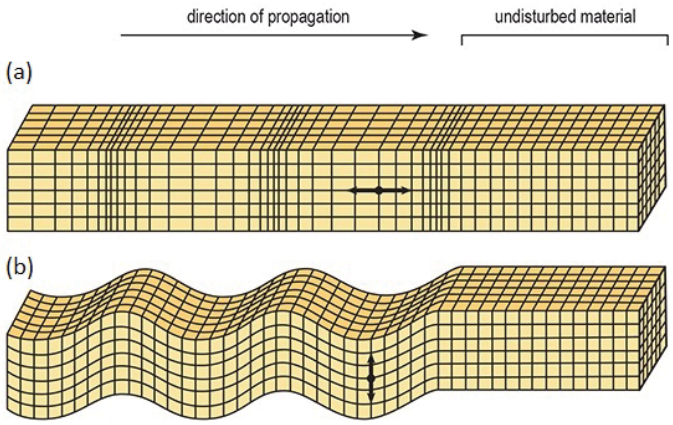

Figure 3.2 : Types of acoustic waves in a waveguide. (a) compressional (b) Shear waves. Picture from [81]

Acoustic modes are obtained by solving the wave equation (Eq. (3.22)) in the absence of external force. In general finding acoustic modes is considerably more difficult than optical modes and for a waveguide with any given configuration numeric techniques are often required to obtain acoustic modes. Among analytic approaches applicable for simpler configurations, we review the method of potential theory which is generally used to illustrate waves in an isotropic unbound plate.

Following [80], we define the acoustic wave vector $\mathbf{K}$ of a plane wave propagating along the direction $\hat{\mathbf{l}}$

$$\begin{aligned} \mathbf{K} &= |\mathbf{K}|\hat{\mathbf{l}} \\ &= |\mathbf{K}|(\hat{\mathbf{x}}l_x + \hat{\mathbf{y}}l_y + \hat{\mathbf{z}}l_z), \end{aligned} \tag{3.28}$$

Now by substituting into the acoustic wave equation and simplifying the terms, in the absence of external force and assuming an isotropic medium, we have

$$c_{44}\nabla^2\mathbf{v} + (c_{11} - c_{44})\nabla(\nabla.\mathbf{v}) = \rho\partial_t^2\mathbf{v}, \tag{3.29}$$

where $\mathbf{v} = \partial_t u$ and is expressed in terms of scalar(Φ) and vector($\mathbf{\Psi}$) potentials via

$$\mathbf{v} = \nabla\Phi + \nabla \times \mathbf{\Psi}, \tag{3.30}$$

we now substitute Eq. (3.30) into Eq. (3.29)

$$\nabla(c_{11}\nabla^2\Phi - \rho\partial_t^2\Phi) - \nabla \times (c_{44}\nabla \times \nabla \times \mathbf{\Psi} + \rho\partial_t^2\mathbf{\Psi}) = 0, \tag{3.31}$$

One way to satisfy Eq. (3.31) is that

$$\nabla^2\Phi - \frac{1}{V_l^2}\partial_t^2\Phi = 0, \tag{3.32}$$

$$\nabla \times \nabla \times \mathbf{\Psi} + \frac{1}{V_s^2}\partial_t^2\mathbf{\Psi} = 0. \tag{3.33}$$

where V_l and V_s are longitudinal and shear velocities defined by

$$V_l = \sqrt{\frac{c_{11}}{\rho}}, \tag{3.34}$$

$$V_s = \sqrt{\frac{c_{44}}{\rho}}, \tag{3.35}$$

If we set $\mathbf{\Psi} = 0$, then Eq. (3.32) results in a pure longitudinal acoustic wave. By assuming the scalar potential Φ to be zero, then the solution to the wave equation is a pure shear wave.

In a pure shear wave, acoustic deformations are only along transverse direction(s) of propagation as shown in Fig. 3.2(a). In a pure longitudinal wave in contrast, the displacements are only along the propagation directions (Fig. 3.2(b)). In a pure homogeneous medium longitudinal waves propagate faster because $V_{\rm l} > V_{\rm s}$. In an inhomogeneous medium such as a conventional optical waveguide, these two waves are usually coupled so that there is no pure shear or compressional wave [82]. The dispersion relation corresponding to these two waves are expressed by

$$K_{\rm ts}^2 + q^2 = (\frac{\Omega}{V_{\rm s}})^2, \tag{3.36}$$

$$K_{\rm tl}^2 + q^2 = (\frac{\Omega}{V_{\rm l}})^2, \tag{3.37}$$

where $K_{\rm ts}$ and $K_{\rm tl}$ are transverse and longitudinal components of acoustic wave vector, q is the acoustic wavenumber. In non-bulk waveguides, these equations are to be solved via considering the acoustic boundary conditions on waveguide interfaces

$$\mathbf{T}_1 \cdot \mathbf{n} = \mathbf{T}_2 \cdot \mathbf{n},$$

where $\mathbf{T}_1$ and $\mathbf{T}_2$ are stress in medium 1 and 2 of an interface, respectively and $\mathbf{n}$ is the normal vector of the interface. In Fig. 3.3 and 3.4 we have computed pure longitudinal and shear modes for a suspended silicon nanowire with cross section dimensions $300\,[\rm nm] \times 220\,[\rm nm]$. As expected, the pure longitudinal modes occur at higher acoustic frequencies than shear modes of the same order. These modes are computed by assuming that $u_{\rm z} = 0$ for pure shear and $u_{\rm x} = u_{\rm y} = 0$ for pure longitudinal modes. However, the real acoustic modes in these integrated geometries are a mixture of both shear and longitudinal waves; For a given acoustic beta, the mode is purely shear at lower frequencies, then it becomes like mixture of pure and longitudinal as shown for a few of the modes in Fig. 3.5. Finally the acoustic mode form a pure longitudinal mode at higher frequencies.

3.5 Acoustic power and energy

For an acoustic field represented by Eq. (3.15) the averaged power can be obtained by

$$\mathbf{P}^{(\rm ac)} = \frac{1}{T_{\rm ac}} \iint \big[(\partial_t \mathbf{U}).\mathbf{T}\big] dsdt, \tag{3.38}$$

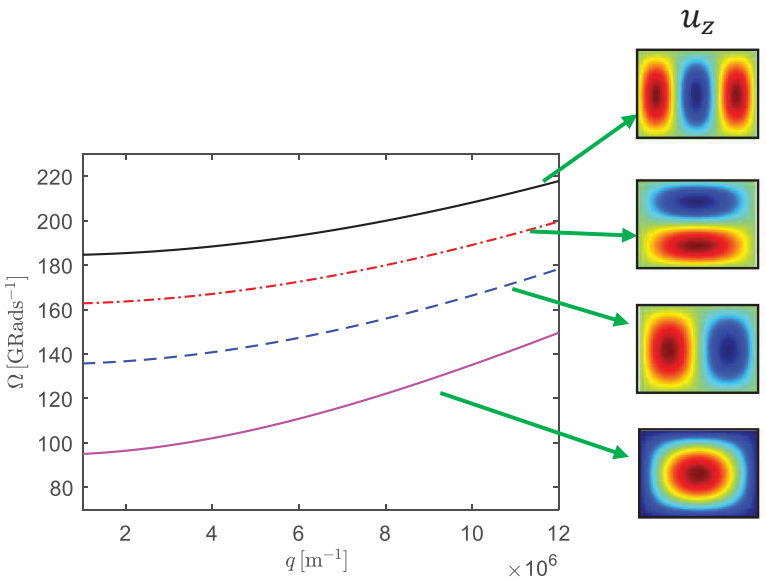

Figure 3.3 : Pure longitudinal acoustic modes in a suspended silicon nanowire with cross section dimensions 300[nm] $\times$ 210[nm].

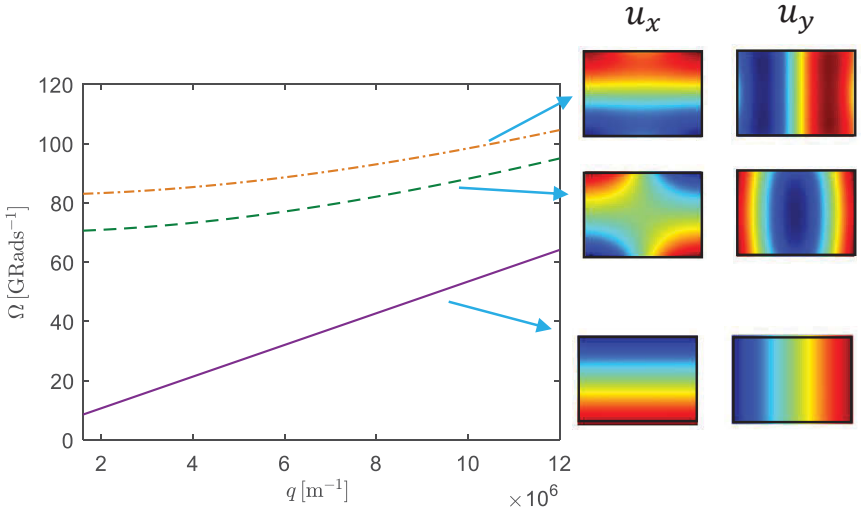

Figure 3.4 : Pure shear acoustic modes in a suspended silicon nanowire with cross section dimensions 300[nm] $\times$ 210[nm].

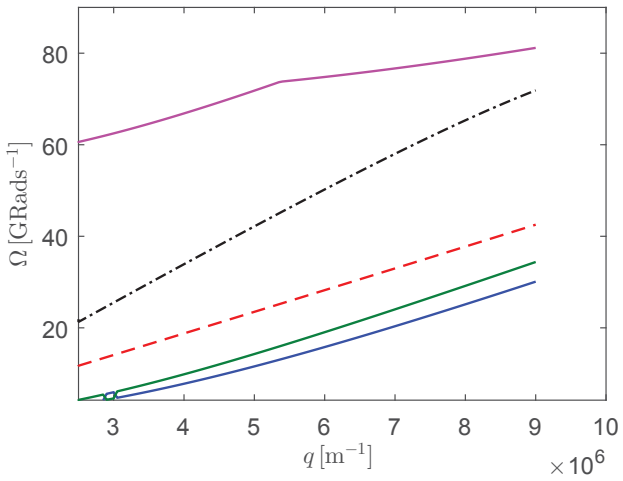

Figure 3.5 : Acoustic modes in a suspended silicon nanowire with cross section dimensions 300[nm] × 210[nm].

where T_{ac} is the acoustic cycle. Assuming that the acoustic wave is propagating along z, then

$$|\mathbf{P}^{(\text{ac})}| = P_{\text{z}}^{(\text{ac})} = 2i\Omega \int (\sum_{jkl} u_j^* C_{zjkl} \partial_k u_l)\ ds. \tag{3.39}$$

Acoustic energy is the sum of kinetic and elastic stored energies [80]

$$\mathcal{E}_{\text{ac}} = \frac{1}{2T_{\text{ac}}} \iint [\rho |\partial_t \mathbf{U}|^2 + \sum_{ijkl} S_{ij} C_{ijkl} S_{kl}]\ dsdt, \tag{3.40}$$

Moreover in typical cases the total momentum of a waveguide is zero which means that the elastic energy is equal to that of kinetic energy (assuming $b = 1$).

$$\begin{aligned} \mathcal{E}_{\text{ac}} &= \frac{1}{T_{\text{ac}}} \iint [\rho |\partial_t \mathbf{U}|^2]\ dsdt \\ &= 2\Omega^2 \int \rho |\mathbf{u}|^2\ ds. \end{aligned} \tag{3.41}$$

Similar to electromagnetic waves [83] two quantities $P_{\text{z}}^{(\text{ac})}$ and $\mathcal{E}_{\text{ac}}$ are related via

$$P_{\text{z}}^{(\text{ac})} = v_g^{(ac)} \mathcal{E}_{\text{ac}}, \tag{3.42}$$

where $v_g^{(ac)}$ is the acoustic group velocity.

3.6 Power conversion in SBS: field perturbation and mechanism of energy exchange

The field interference between pump and Stokes, if satisfies the phase matching conditions Eq. (2.1) and (2.2), gives rise to a Bragg grating which travels along with the acoustic wave. As a result, the optical mode profile changes. The new optical fields can be expressed by

$$\mathbf{E}^{(\text{new})} = \mathbf{E} + \Delta\mathbf{E}, \tag{3.43}$$

$$\mathbf{D}^{(\text{new})} = \mathbf{D} + \Delta\mathbf{D}, \tag{3.44}$$

where $\Delta\mathbf{E}$ ($\Delta\mathbf{D}$) are the perturbed electric (displacement) field vector. We note that the new optical fields in Eq. (3.43) and Eq. (3.44) satisfy the wave equation (Eq. (3.3)). Only those harmonics of the perturbed fields which satisfy the phase matching conditions can effectively contribute to the SBS interactions. This means that only phase-matched harmonics have nonzero time-average effect on the acoustic response of the waveguide. Using Eq. (3.8) and Eq. (3.15) the perturbed fields $\Delta\mathbf{E}$ and $\Delta\mathbf{D}$ can be further expanded as

$$\Delta\mathbf{E} = A^{(2)}b\Delta\tilde{\mathbf{e}}^{(1)} + A^{(1)}b^{*}\Delta\tilde{\mathbf{e}}^{(2)} + c.c, \tag{3.45}$$

$$\Delta\mathbf{D} = A^{(2)}b\Delta\tilde{\mathbf{d}}^{(1)} + A^{(1)}b^{*}\Delta\tilde{\mathbf{d}}^{(2)} + c.c, \tag{3.46}$$

The optical modes $\Delta\tilde{\mathbf{e}}^{(1)}$ and $\Delta\tilde{\mathbf{e}}^{(2)}$ are small perturbations caused in the optical mode profile which can be expressed by

$$\Delta\tilde{\mathbf{e}}^{(i)} = \Delta\hat{\mathbf{e}}^{(i)}(x,y)e^{(i\beta_i z - i\omega_i t)}. \tag{3.47}$$

At this stage we assume that the optical loss is negligible. While this assumption enables us to provide a quantitative picture of SBS gain, it does not limit the suitability of our approach : the impact of optical loss will be included appropriately in the next steps. By substituting Eq. (3.6) into Eq. (3.44), the wave equation Eq. (3.3) in the perturbed waveguide can be expanded and separated for pump and Stokes frequencies:

$$A^{(1)}[\nabla\times\nabla\times\tilde{\mathbf{e}}^{(1)}-\mu\omega_1^2\tilde{\mathbf{d}}^{(1)}]+\partial_z A^{(1)}[\hat{z}\times\nabla\times\tilde{\mathbf{e}}^{(1)}+\nabla\times\hat{z}\times\tilde{\mathbf{e}}^{(1)}]+$$
$$\partial_t A^{(1)}(-2i\mu\omega\tilde{\mathbf{d}}^{(1)})+A^{(2)}b[\nabla\times\nabla\times\Delta\tilde{\mathbf{e}}^{(1)}-\mu\omega_1^2\Delta\tilde{\mathbf{d}}^{(1)}]+h.o.t.+c.c=0, \tag{3.48}$$

$$A^{(2)}[\nabla\times\nabla\times\tilde{\mathbf{e}}^{(2)}-\mu\omega_2^2\tilde{\mathbf{d}}^{(2)}]+\partial_z A^{(2)}[\hat{z}\times\nabla\times\tilde{\mathbf{e}}^{(2)}+\nabla\times\hat{z}\times\tilde{\mathbf{e}}^{(2)}]+$$
$$\partial_t A^{(2)}(-2i\mu\omega\tilde{\mathbf{d}}^{(2)})+A^{(1)}b^*[\nabla\times\nabla\times\Delta\tilde{\mathbf{e}}^{(2)}-\mu\omega_2^2\Delta\tilde{\mathbf{d}}^{(2)}]+h.o.t.+c.c=0 \tag{3.49}$$

where *h.o.t.* accounts for higher order time and space derivatives which can be neglected in the case of slowly varying envelopes. Moreover, in deriving Eq. (3.48) and Eq. (3.49) we have neglected $\partial_t b$ and consider the steady state for the acoustic wave.

In the steady state (i.e. $\partial_t=0$), the optical mode $\mathbf{e}^{(1)}(\mathbf{e}^{(2)})$ is projected on both sides of Eq. (3.48)(Eq. (3.49)), then integrated over a time interval $T^{(\mathrm{opt})}$ ($T^{(\mathrm{opt})}$ is the optical cycle) to obtain

$$\partial_z A^{(1)}-\frac{1}{v_{\mathrm{g}}^{(1)}}\partial_t A^{(1)}+\frac{i\omega_1 Q_1}{\mathcal{P}^{(1)}}A^{(2)}b=0, \tag{3.50}$$

$$\partial_z A^{(2)}-\frac{1}{v_{\mathrm{g}}^{(2)}}\partial_t A^{(2)}+\frac{i\omega_2 Q_2}{\mathcal{P}^{(2)}}A^{(1)}b^*=0, \tag{3.51}$$

where Q_{i} is an overlap integral expressed by

$$\begin{aligned}Q_i&=\frac{-1}{\mu\omega_{\mathrm{i}}^2}\int\tilde{\mathbf{e}}^{(\mathrm{i})}\cdot(\nabla\times\nabla\times\Delta\tilde{\mathbf{e}}^{(\mathrm{i})}-\mu\omega_{\mathrm{i}}^2\Delta\tilde{\mathbf{d}}^{(\mathrm{i})})\,ds\\&=\int([\tilde{\mathbf{d}}^{(\mathrm{i})}]^*.\Delta\tilde{\mathbf{e}}^{(\mathrm{i})}+[\tilde{\mathbf{e}}^{(\mathrm{i})}]^*.\Delta\tilde{\mathbf{d}}^{(\mathrm{i})})\,ds.\end{aligned} \tag{3.52}$$

Equation (3.50) in the steady state regime is simplified to

$$\partial_z A^{(1)}+\frac{i\omega_1 Q_1}{\mathcal{P}_1}A_2 b=0, \tag{3.53}$$

$$\partial_z A^{(2)}+\frac{i\omega_2 Q_2}{\mathcal{P}_2}A_1 b^*=0, \tag{3.54}$$

From Eq. (3.53) and Eq. (3.54), in the absence of nonlinear SBS interactions (i.e. $Q_i=0$), the optical envelope $A^{(\mathrm{i})}$ does not vary as it travels through the waveguide. In the presence of SBS process however, the overlap integral is nonzero which implies variation of the optical mode through the waveguide. Since we have assumed a lossless structure, the optical power is transfered from pump to the Stokes.

The overlap integrals Q_{i} represent the impact of field perturbation caused by the acoustic waves on the optical envelopes. In general, field perturbation occurs

due to either photoelasticity or waveguide moving boundaries [79]. The expression of the overlap integral in Eq. (3.52) is the overall contribution. We decompose Q_i to separately calculate it inside and on waveguide boundaries. In the following we describe these impacts on the overlap integral in detail. Figure 3.6 (a) shows a waveguide in two different situations; without stress and under mechanical stress that leads to a slight deformation. The integrating domain in Fig. 3.6 (a) is divided into two parts; Inside the waveguide cross section(A_1), away from the boundaries and on the boundaries (A_2). We first examine Eq. (3.52) in the domain (A_1).

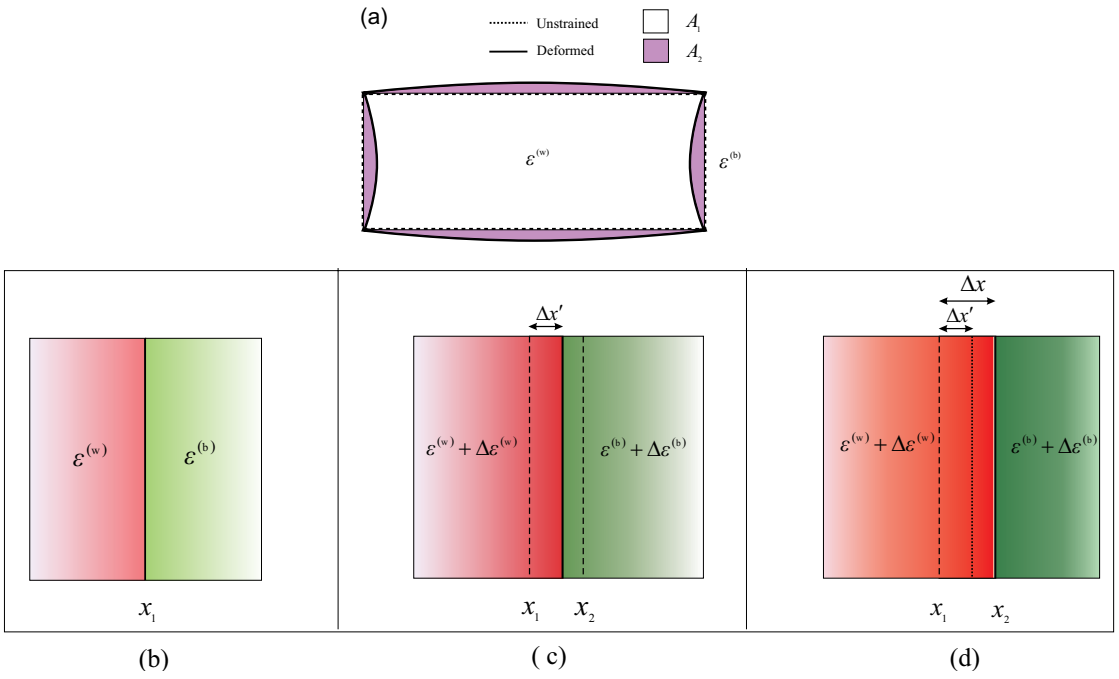

Figure 3.6 : (a) Schematic of a typical waveguide in two different situations; no strain and under strain. (b-d) Waveguide boundary deformed by electrostriction and radiation pressure; (b) Before deformation (c) deformed by only electrostriction (d) deformed only due to radiation pressure.

3.6.1 Impact of electrostriction away from waveguide boundaries

Photoelasticity is the change in the refractive index of a material due to mechanical strain [84]. The photoelastic effect is usually characterized by using Pockels' elasto-optic fourth rank tensor p which expresses the relation between mechanical

strain and variation of material relative permittivity:

$$\begin{aligned}\Delta\epsilon_{ij} &= -\sum_{k,l,m,n} \epsilon_{ik} p_{klmn} \epsilon_{lj} S_{mn} \\ &= -\frac{1}{2}\sum_{k,l,m,n} \epsilon_{ik} p_{klmn} \epsilon_{lj} \partial_m U_n - \frac{1}{2}\sum_{k,l,m,n} \epsilon_{ik} p_{klmn} \epsilon_{lj} \partial_n U_m \\ &= -\frac{1}{2}\sum_{k,l,m,n} \epsilon_{ik} p_{klmn} \epsilon_{lj} \partial_m U_n - \frac{1}{2}\sum_{k,l,m,n} \epsilon_{ik} p_{klnm} \epsilon_{lj} \partial_n U_m \\ &= -\sum_{k,l,m,n} \epsilon_{ik} p_{klmn} \epsilon_{lj} \partial_m U_n,\end{aligned} \tag{3.55}$$

where $\{i,j,k,l,m,n\} = \{1,2,3\}$ and we have assumed the photoelastic tensor p to be symmetric as we are studying SBS process in centrosymmetric crystals. $\Delta\epsilon_{ij}$ is the ij^{th} component of the difference between the relative permittivity strained and unstrained waveguide and S_{kl} are components of the strain matrix. The tensor p is dimensionless. The symmetry properties described for the stiffness tensor in Eq. (3.25) apply also to the photoelastic tensor. In the case of isotropic or cubic materials of class $m3m$, Eq. (3.55) can be further simplified because the relative permittivity takes a diagonal matrix [85]

$$\Delta\epsilon_{ij} = -\epsilon^2 \sum p_{ijmn} \partial_m U_n, \tag{3.56}$$

the displacement field $\mathbf{D}$ is then changed by $\Delta D_i = \Delta\epsilon_{ij} E_j$. The term $\Delta\tilde{\mathbf{e}}$ is nonzero only on waveguide boundaries and interfaces between waveguide materials with different refractive index. Therefore, the overlap integral within the waveguide — apart from the waveguide boundaries — is explicitly due to the photoelasticity. Using Eq. (3.52)

$$\begin{aligned}Q_1^{(\mathrm{PE})} &= \int \left([\tilde{\mathbf{e}}^{(1)}]^* . \Delta\tilde{\mathbf{d}}^{(1)}\right) ds \\ &= -\epsilon_0 \int \Big(\sum_{ijmn} [\tilde{e}_{\mathrm{i}}^{(1)}]^* \tilde{e}_j^{(2)} \epsilon^2 p_{ijmn} \partial_m u_n \Big) \, ds,\end{aligned} \tag{3.57}$$

where non-phase matched terms are neglected. In a similar way, $Q_2^{(\mathrm{PE})}$ can be obtained. By comparing the two overlap integrals one finds that $Q_1^{(\mathrm{PE})} = [Q_2^{(\mathrm{PE})}]^*$.

3.6.2 Field perturbation on waveguide boundaries

The field perturbation on waveguide boundaries include nonzero terms for both electric and displacement fields. Figures 3.6(b-d) show the an infinitesimal segment

of the waveguide boundary before field perturbation. From the figure, the waveguide boundary is located at x_1. The relative permittivity of the waveguide and the surrounding medium are denoted by $\epsilon^{(\mathrm{w})}$ and $\epsilon^{(\mathrm{b})}$, respectively. Deformation of the waveguide boundaries in SBS is the result of electrostriction and radiation pressure. While these two effects are simultaneously applied on a waveguide, in order to evaluate the contribution of each effect, we consider them in a sequence; first only electrostriction is applied then only radiation pressure is considered in the model. For this, we define a intermediate step at which, the displacement field is changed only due to the electrostriction and the waveguide boundary is moved $x_1 + \Delta x'$. In this step, we assume that tangential electric fields are unperturbed in the limit of unperturbed fields. Next, the radiation pressure is presented which shifts the boundary to $x_1 + \Delta x$. We will see that this model is accurate because in practice, Δx is infinitesimal. In the following we explain the two steps in detail.

The relative permittivity of the waveguide and the background are changed according to Eq. (3.55). The fields $\mathbf{E}^{(\mathrm{ES-perturbed})}$ and $\mathbf{D}^{(\mathrm{ES-perturbed})}$ at point $x_1+\Delta x' < x_\mathrm{p} < x_2$ are

$$\begin{aligned}\mathbf{E}^{(\mathrm{ES-perturbed})} &= \mathbf{E}_\parallel + [\epsilon^{(\mathrm{b})} + \Delta\epsilon^{(\mathrm{b})}]^{-1}\epsilon_0^{-1}(\mathbf{D}_\perp + \Delta\mathbf{D}_\perp^{(\mathrm{ES,b})}) \\ &\approx \mathbf{E}_\parallel + [\epsilon^{(\mathrm{b})}]^{-1}\epsilon_0^{-1}(\mathbf{D}_\perp + \Delta\mathbf{D}_\perp^{(\mathrm{ES,b})}),\end{aligned} \tag{3.58}$$

$$\begin{aligned}\mathbf{D}^{(\mathrm{ES-perturbed})} &= (\epsilon^{(\mathrm{b})} + \Delta\epsilon^{(\mathrm{b})})\epsilon_0\mathbf{E}_\parallel + (\mathbf{D}_\perp + \Delta\mathbf{D}_\perp^{(\mathrm{ES,b})}) \\ &\approx \epsilon^{(\mathrm{b})}\epsilon_0\mathbf{E}_\parallel + (\mathbf{D}_\perp + \Delta\mathbf{D}_\perp^{(\mathrm{ES,b})}),\end{aligned} \tag{3.59}$$

where the symbols $\parallel$ and $\perp$ refer to parallel and perpendicular field components, respectively. $\Delta\mathbf{D}_\perp^{(\mathrm{ES,b})}$ and $\Delta\mathbf{D}_\perp^{(\mathrm{ES,w})}$ are the normal components of $\Delta\mathbf{D}$ formed because of the change in the refractive index on both sides of the boundary due to the photoelasticity. We note that the tangential electric fields in Eq. (3.58) and Eq. (3.59) are assumed to remain unperturbed in the limit of infinitesimal boundary displacement. Moreover, the boundary condition for the displacement field shows that

$$\Delta\mathbf{D}_\perp^{(\mathrm{ES,b})} = \Delta\mathbf{D}_\perp^{(\mathrm{ES,w})} = \Delta\mathbf{D}_\perp^{(\mathrm{ES})}. \tag{3.60}$$

Now, we include the effect of boundary movement as an additional perturbation to $\mathbf{D}$. Then as shown in Fig. 3.6 (d) the waveguide boundary is shifted to x_2.

We here make an approximation: that the strain components S_{ij} do not change through the width Δx. As long as Δx is infinitesimal, this is a valid approximation. Therefore and according to Eq. (3.55), $\Delta\epsilon^{(\mathrm{w})}$ and $\Delta\epsilon^{(\mathrm{b})}$ do not change noticeably as the boundary is shifted from $x_1 + x'$ to x_2. The fields $\mathbf{E}^{(\mathrm{ES-MB-perturbed})}$ and $\mathbf{D}^{(\mathrm{ES-MB-perturbed})}$ at point $x_1 + \Delta x' < x_\mathrm{p} < x_2$ can be expressed by

$$\mathbf{E}^{\mathrm{ES-MB-perturbed}} \approx \mathbf{E}_\parallel + [\epsilon^{(\mathrm{w})}]^{-1}\epsilon_0^{-1}(\mathbf{D}_\perp + \Delta\mathbf{D}_\perp^{(\mathrm{ES,w})}), \tag{3.61}$$

$$\mathbf{D}^{\mathrm{ES-MB-perturbed}} \approx \epsilon^{(\mathrm{w})}\epsilon_0\mathbf{E}_\parallel + (\mathbf{D}_\perp + \Delta\mathbf{D}_\perp^{(\mathrm{ES,w})}). \tag{3.62}$$

Now, using Eqs. (3.58), (3.59), (3.61) and (3.62), the field perturbations on the boundary can be expressed as follows

$$\begin{aligned}\Delta\mathbf{E}^{(\mathrm{MB})} &= \mathbf{E}^{\mathrm{ES-MB-perturbed}} - \mathbf{E}^{\mathrm{ES-perturbed}} \\ &= \left[(\epsilon^{(\mathrm{w})})^{-1} - (\epsilon^{(\mathrm{b})})^{-1}\right]\epsilon_0^{-1}\mathbf{n}(\mathbf{n}.(\mathbf{D} + \Delta\mathbf{D}^{(\mathrm{ES})})) \\ &= \left[(\epsilon^{(\mathrm{w})})^{-1} - (\epsilon^{(\mathrm{b})})^{-1}\right]\epsilon_0^{-1}\mathbf{n}(\mathbf{n}.(\mathbf{D}) + \\ &\epsilon^{(\mathrm{b})}\mathbf{n}(\mathbf{n}.(\sum p_{ijkl}^{(\mathrm{b})}\partial_k u_l E_j\hat{i})) - \epsilon^{(\mathrm{w})}\mathbf{n}(\mathbf{n}.(\sum p_{ijkl}^{(\mathrm{w})}\partial_k u_l E_j\hat{i})),\end{aligned} \tag{3.63}$$

$$\begin{aligned}\Delta\mathbf{D}^{(\mathrm{MB})} &= \mathbf{D}^{\mathrm{ES-MB-perturbed}} - \mathbf{D}^{\mathrm{ES-perturbed}} \\ &= (\epsilon^{(\mathrm{w})} - \epsilon^{(\mathrm{b})})\epsilon_0(-\mathbf{n}\times\mathbf{n}\times\mathbf{E}),\end{aligned} \tag{3.64}$$

where the term MB refers to moving boundary, $p_{ijkl}^{(\mathrm{b})}$ and $p_{ijkl}^{(\mathrm{w})}$ are photoelastic tensor components in background and waveguide, respectively. We can now calculate the overlap integral (Eq. (3.52)) in domain A_2. By substituting Eq. (3.63) and Eq. (3.64) in Eq. (3.52)

$$Q_i^{(\mathrm{MB})} = \int_{A_2} (\tilde{\mathbf{d}}^{(\mathrm{i})}.[\Delta\tilde{\mathbf{e}}^{(\mathrm{i,MB})]^*} + \tilde{\mathbf{e}}^{(\mathrm{i})}.[\Delta\tilde{\mathbf{d}}^{(\mathrm{i,MB})}]^*)\, ds. \tag{3.65}$$

By substituting Eq. (3.63) and (3.64) in Eq. (3.52), $Q_1^{(\mathrm{MB})}$ is

$$\begin{aligned}Q_1^{(\mathrm{MB})} = \int_{\mathcal{C}} \Bigg(&((\epsilon^{(\mathrm{w})})^{-1} - (\epsilon^{(\mathrm{b})})^{-1})\epsilon_0^{-1}(\mathbf{n}.[\tilde{\mathbf{d}}^{(1)}]^*)(\mathbf{n}.\tilde{\mathbf{d}}^{(2)}) \\ &+ (\epsilon^{(\mathrm{w})} - \epsilon^{(\mathrm{b})})\epsilon_0(\mathbf{n}\times[\tilde{\mathbf{e}}^{(1)}]^*).(\mathbf{n}\times\tilde{\mathbf{e}}^{(2)})\Bigg)\ (\mathbf{n}.\mathbf{u}\, dl) \\ + \int_{A_2} \Bigg(&\mathbf{n}.\Big[(\epsilon^{(\mathrm{b})})^2\epsilon_0 \sum P_{ijkl}^{(\mathrm{b})}\partial_k u_l^* e_i^{*,(1,\mathrm{b})} e_j^{(2,\mathrm{b})}\hat{i} \\ &- (\epsilon^{(\mathrm{w})})^2\epsilon_0 \sum P_{ijkl}^{(\mathrm{w})}\partial_k u_l^* e_i^{*,(1,\mathrm{w})} e_j^{(2,\mathrm{w})}\hat{i}\Big]\Bigg)\, ds,\end{aligned} \tag{3.66}$$

where $\mathcal{C}$ is the waveguide boundary, $\hat{i}$ is the unit vector with $\{i,j,k,l,\} \in \{x,y,z\}$ and $ds = \mathbf{n}.\mathbf{u}\,dl$ on the boundary ($\mathbf{n}$ is the normal vector on each boundary). We note that permittivities are assumed to be isotropic in Eq. (3.66). Similarly, $Q_2^{(\mathrm{MB})}$ can be obtained. It can be shown that $Q_1^{(\mathrm{MB})} = [Q_2^{(\mathrm{MB})}]^*$.

We have divided the overlap integral $Q_1^{(\mathrm{MB})}$ into two integrals; the first integral represents the impact of radiation pressure, i.e.

$$\begin{aligned} Q_1^{(\mathrm{MB-RP})} = \int_{\mathcal{C}} \Big(&((\epsilon^{(\mathrm{w})})^{-1} - (\epsilon^{(\mathrm{b})})^{-1})\epsilon_0^{-1}(\mathbf{n}.[\tilde{\mathbf{d}}^{(1)}]^*)(\mathbf{n}.\tilde{\mathbf{d}}^{(2)}) \\ &+ (\epsilon^{(\mathrm{w})} - \epsilon^{(\mathrm{b})})\epsilon_0(\mathbf{n}\times[\tilde{\mathbf{e}}^{(1)}]^*).(\mathbf{n}\times\tilde{\mathbf{e}}^{(2)})\Big)(\mathbf{n}.\mathbf{u}\,dl). \end{aligned} \tag{3.67}$$

while the second integral shows the impact of electrostriction

$$\begin{aligned} Q_1^{(\mathrm{MB-ES})} = \int_{A_2} \Big(&\mathbf{n}.\big[(\epsilon^{(\mathrm{b})})^2\epsilon_0 \sum p_{ijkl}^{(\mathrm{b})}\partial_k u_l^* e_i^{*,(1,\mathrm{b})} e_j^{(2,\mathrm{b})}\hat{i} \\ &- (\epsilon^{(\mathrm{w})})^2\epsilon_0 \sum p_{ijkl}^{(\mathrm{w})}\partial_k u_l^* e_i^{*,(1,\mathrm{w})} e_j^{(2,\mathrm{w})}\hat{i}\big]\Big)\, ds. \end{aligned} \tag{3.68}$$

3.7 Acoustic wave equation

To describe the variation of acoustic displacement envelope we derive the corresponding dynamic equation from acoustic wave equation. We begin by Eq. (3.17)

$$\rho\partial_t^2\mathbf{U} = \nabla.\mathbf{T} + \mathbf{F},$$

where the external optical force $\mathbf{F}$ can be expressed by the following ansatz

$$\mathbf{F} = A^{(1)}[A^{(2)}]^*\mathbf{f} + c.c. \tag{3.69}$$

in which $\mathbf{f}$ denotes the force mode. We substitute the displacement field (i.e. Eq. (3.15)) in Eq. (3.22). Then we simplify Eq. (3.17) by neglecting the higher order derivatives and non-phase matched terms (i.e. those terms with different acoustic frequency than Ω)

$$\begin{aligned} &b\big[(C_{ijkl} - i\Omega\eta_{ijkl})\partial_j\partial_k u_l - (-i\Omega)^2\rho u_i\big] + \partial_z b\big[(C_{izkl} + (-i\Omega)\eta_{izkl})\partial_k u_l + \\ &(C_{ijkz} - i\Omega\eta_{ijkz})\partial_j u_k\big] + \partial_t b\big[\eta_{ijkl}\partial_k u_l - 2(-i\Omega)\rho u_i\big] + \tilde{f}_i A^{(1)}[A^{(2)}]^* + c.c = 0. \end{aligned} \tag{3.70}$$

We now project on the acoustic velocity field $\mathbf{v} = \partial_t\tilde{\mathbf{u}} + c.c$ to both sides of Eq. (3.22) and integrate over the time interval T larger that the pump/Stokes optical cycle to

obtain

$$\begin{aligned} & b(\frac{\Omega^2}{T}\iint_T [u_i]^* \partial_j \eta_{ijkl} \partial_k u_l \; dsdt) \\ & + \partial_z b\big[\frac{\mathcal{P}^{(\mathrm{ac})} + i\mathcal{P}^{(\mathrm{ac,loss})}}{2}\frac{i\Omega}{T}\iint_T (C_{ijkz} - i\Omega\eta_{ijkz})[u_i]^* \partial_j u_k dsdt\big] \\ & + \partial_t b[\frac{-2\Omega^2}{T}\iint_T \rho(|u_i|^2 dsdt) + (i\Omega)\iint [u_i]^* \eta_{ijkl}\partial_k u_l \; dsdt] \\ & - \frac{i\Omega}{T}\iint_T u_i^* . \tilde{f}_i A^{(1)}[A^{(2)}]^* dsdt + c.c = 0, \end{aligned} \tag{3.71}$$

where we have neglected higher order time and spacial derivatives. Equation (3.71) can be further simplified by making some approximations. By expanding the coefficient of $\partial_z b$ we find that

$$\frac{i\Omega}{T}\iint_T \sum_i (C_{ijkz})\partial_j u_k [u_i]^* dsdt \approx \frac{\mathcal{P}^{(\mathrm{ac})}}{2}, \tag{3.72}$$

$$\frac{i\Omega}{T}\iint_T \sum_i (-i\Omega\eta_{ijkz})\partial_j u_k [u_i]^* dsdt \approx i\frac{\mathcal{P}^{(\mathrm{ac,loss})}}{2}. \tag{3.73}$$

Similar to the approach described for the electromagnetic part in section 3.2, if we neglect the acoustic loss Eq. (3.71) is simplified to

$$\partial_z b - \frac{1}{v_g^{(\mathrm{ac})}}\partial_t b = \frac{i\Omega Q_b}{\mathcal{P}^{(\mathrm{ac})} + i\mathcal{P}^{(\mathrm{ac,loss})}} A^{(1)}[A^{(2)}]^*, \tag{3.74}$$

where Q_b is the overlap integral expressed by

$$Q_b = \int \mathbf{f}.\mathbf{u}^* \; ds. \tag{3.75}$$

By including the acoustic loss in Eq. (3.74) we have

$$\begin{aligned} \partial_z b - \frac{1}{v_g^{(\mathrm{ac})}}\partial_t b + \alpha_{\mathrm{ac}} b &= \frac{-i\Omega Q_b}{\mathcal{P}^{(\mathrm{ac})} + i\mathcal{P}^{(\mathrm{ac,loss})}} A^{(1)}[A^{(2)}]^* \\ &\approx \frac{-i\Omega Q_b}{\mathcal{P}^{(\mathrm{ac})}} A^{(1)}[A^{(2)}]^*, \end{aligned} \tag{3.76}$$

where α_{ac} is the linear loss coefficient expressed by

$$\begin{aligned} \alpha_{\mathrm{ac}} &= \frac{\Omega^2}{\mathcal{P}^{(\mathrm{ac})} + i\mathcal{P}^{(\mathrm{ac,loss})}} \int [u_i]^* \partial_j \eta_{ijkl} \partial_k u_l \; ds \\ &\approx \frac{\Omega^2}{\mathcal{P}^{(\mathrm{ac})}} \int [u_i]^* \partial_j \eta_{ijkl} \partial_k u_l \; ds. \end{aligned} \tag{3.77}$$

3.7.1 Relation between the defined overlap integrals

We here derive the relation between the introduced overlap integrals Q_1,Q_2 and Q_b using the energy conservation in the system. The total energy in a waveguide is the sum of optical and mechanical energies denoted by $\mathcal{E}_\mathrm{opt}$ and $\mathcal{E}_\mathrm{mech}$, respectively

$$\mathcal{E}_\mathrm{tot} = \mathcal{E}_\mathrm{opt} + \mathcal{E}_\mathrm{mech}. \tag{3.78}$$

Moreover, $\mathcal{E}_\mathrm{ac}$ is the sum of kinetic and stored energy. We here neglect the temperature variation and assume that waveguide is an isolated system. Consequently, $\mathcal{E}_\mathrm{tot}$ is constant. Then, any change in the optical energy results in a change in the mechanical energy

$$\Delta\mathcal{E}_\mathrm{mech} + \Delta\mathcal{E}_\mathrm{opt} = 0. \tag{3.79}$$

Assuming that the total and angular momentum do not change then the mechanical work must correspond to the change in the optical energy:

$$W = \frac{1}{T_\mathrm{ac}} \int_\mathrm{Tac} \mathbf{U}.\mathbf{F}\ ds = \frac{1}{2}\Delta\mathcal{E}_\mathrm{opt}, \tag{3.80}$$

where the fraction $\frac{1}{2}$ is because only half of the $\Delta\mathcal{E}_\mathrm{opt}$ contributes as a kinetic energy and the other half is stored in the system as an elastic energy. Now we assume that the optical fields are perturbed due to the acoustic waves. Then, $\Delta\mathcal{E}_\mathrm{opt}$ can be expanded by using the perturbed fields $\Delta\mathbf{E}$ and $\Delta\mathbf{D}$

$$\begin{aligned}
\Delta\mathcal{E}_\mathrm{opt} =& \frac{1}{T_\mathrm{opt}}\Big(\int_{T_\mathrm{opt}} (\mathbf{E}+\Delta\mathbf{E})\cdot(\mathbf{D}+\Delta\mathbf{D})\ ds - \int_{T_\mathrm{opt}} (\mathbf{E}\cdot\mathbf{D})\ dsdt\Big) \\
&\approx \frac{1}{T_\mathrm{opt}}\Big(\int_{T_\mathrm{opt}} (\Delta\mathbf{E}\cdot\mathbf{D} + \Delta\mathbf{D}\cdot\mathbf{E})\ dsdt\Big) \\
&= \frac{1}{T_\mathrm{opt}}\Big(\int_{T_\mathrm{opt}} \Big(\big(A^{(1)}[A^{(2)}]^* b^* [\Delta\tilde{\mathbf{e}}^{(1)}]^* \cdot \tilde{\mathbf{d}}^{(1)} + A^{(1)}[A^{(2)}]^* b^* \Delta\tilde{\mathbf{e}}^{(2)} \cdot [\tilde{\mathbf{d}}^{(2)}]^* + c.c\big) \\
&+ \big(A^{(1)}[A^{(2)}]^* b^* [\tilde{\Delta\mathbf{d}}^{(1)}]^* . \tilde{\mathbf{e}}^{(1)} + A^{(1)}[A^{(2)}]^* b^* \tilde{\Delta\mathbf{d}}^{(2)} \cdot [\tilde{\mathbf{e}}^{(2)}]^* + c.c\big)\Big)\ dsdt \\
&= A^{(1)}[A^{(2)}]^* b^* (Q_1^* + Q_2) + c.c.
\end{aligned} \tag{3.81}$$

Now by substituting Eq. (3.81) into Eq. (3.80) and using Eq. (3.15) and Eq. (3.69), we have

$$Q_\mathrm{b} = \int \mathbf{f}.\mathbf{u}^*\ ds = \frac{1}{2}\big(Q_1^* + Q_2\big). \tag{3.82}$$

Since $Q_1 = Q_2^*$ (see section 3.6), then

$$Q_\mathrm{b} = Q_1^* = Q_2. \tag{3.83}$$

3.8 Optical forces in waveguides

In SBS optical forces drive the acoustic fields. These forces, which are generated as a result of pump/Stokes interference, are mainly of two types; electrostriction and radiation pressure. We here describe the characteristics and physics of these forces in detail.

3.8.1 Electrostrictive force

Electrostriction is the tendency of materials to be expanded–or contracted– in the presence of optical fields [73]. Electrostrictive forces are quadratically dependent on the optical fields.

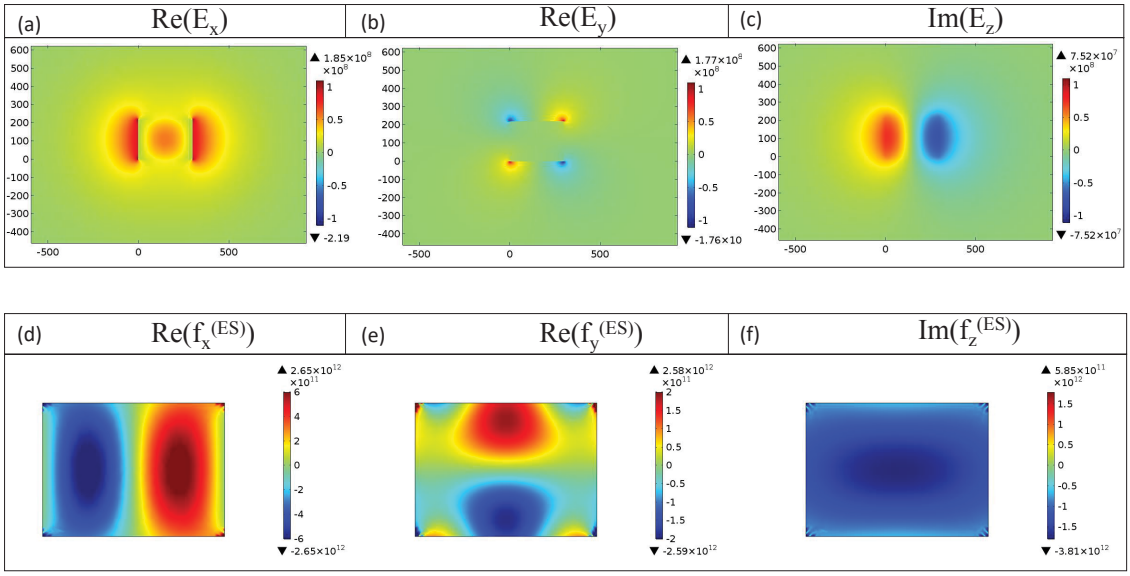

Figure 3.7 : The field components (a)ReE_{x}, (b)ReE_{y} and (c)ImE_{z} of the fundamental optical mode in a suspended silicon waveguide with cross section dimensions 300 [nm] × 220 [nm]. Electrostrictive force components (d) $\mathrm{Re}\left(\mathrm{f}_{\mathrm{x}}^{(\mathrm{ES})}\right)$ (e) $\mathrm{Re}\left(\mathrm{f}_{\mathrm{y}}^{(\mathrm{ES})}\right)$ and (f) $\mathrm{Im}\left(\mathrm{f}_{\mathrm{z}}^{(\mathrm{ES})}\right)$ in an intra mode BSBS process. Pump and Stokes optical modes carry fundamental mode as shown in (a–c).

In order to characterize the effect of electrostriction we assume that the waveguide relative permittivity is changed by $\Delta\epsilon_{ij}$ because of applying electrostriction

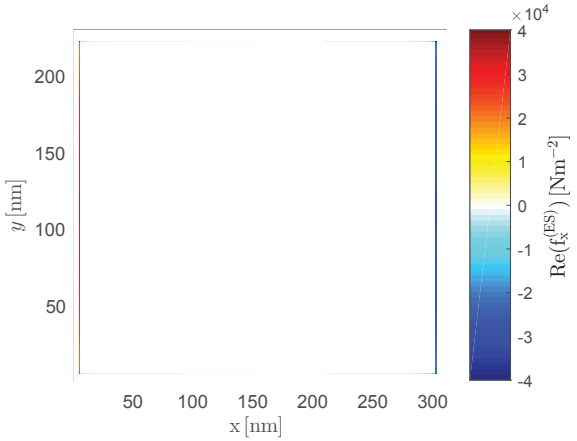

(a)

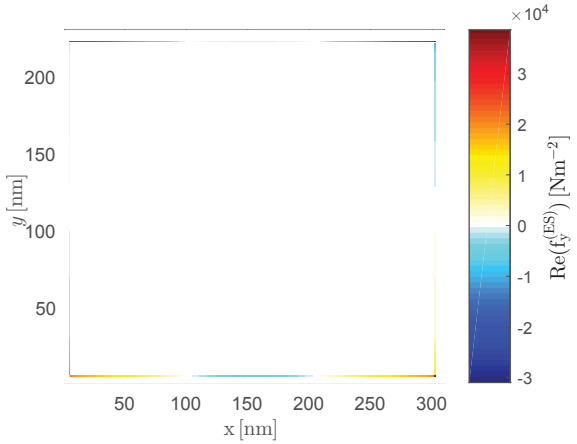

(b)

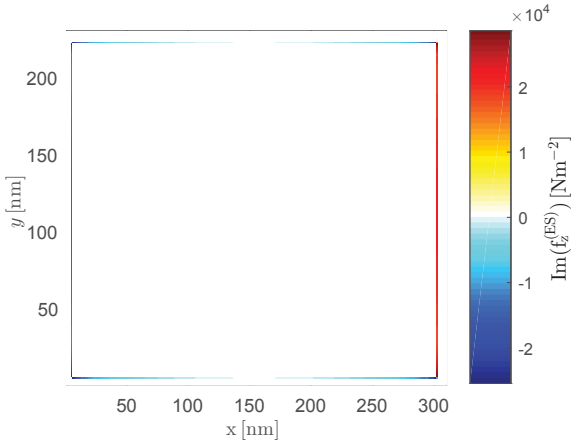

(c)

Figure 3.8 : Electrostrictive boundary forces in intra mode BSBS process in the suspended silicon waveguide with geometry and optical mode profile described in Fig. 3.7.

waveguide. Then the electromagnetic energy $\mathcal{E}$ is changed by

$$\delta\mathcal{E} = \frac{1}{2}\epsilon_0 \Delta\epsilon_{ij} E_j E_i, \tag{3.84}$$

where $\Delta\epsilon_{ij}$ is expressed in terms of the mechanical strain and the photoelastic constant by Eq. (3.55) The electrostrictive stress is then defined as variation of the ratio of energy density with mechanical strain. Using Eq. (3.84) the components of electrostrictive stress tensor can be expressed by

$$\sigma_{ij} = \frac{\partial\mathcal{E}}{\partial S_{mn}} = -\frac{1}{2}\epsilon_{ik} p_{klmn} \epsilon_{lj} E_i E_j. \tag{3.85}$$

The stress tensor in Eq. (3.85) can be further simplified in the case of isotropic and also cubic materials

$$\begin{aligned} \sigma_{ij}^{(\mathrm{es})} &= -\frac{1}{2}\epsilon_0 \epsilon^2 p_{ijkl} E_k E_l \\ &= -\epsilon_0 \epsilon^2 p_{ijkl} \tilde{e}_k^{(1)} [\tilde{e}_l^{(2)}]^*, \end{aligned} \tag{3.86}$$

where we have assumed that material relative permittivity is isotropic. In Eq. (3.86) we have only written the harmonics varying with the acoustic frequency Ω. Then $\delta\mathcal{E}$ is [80]

$$\delta\mathcal{E} = \sigma_{ij}\delta S_{ij}^* = -f_i^{(\mathrm{ES})} \delta u_i^*, \tag{3.87}$$

where $f_i^{(\mathrm{ES})}$ is defined as the electrostrictive force component — in $\mathrm{N/m^3}$ — which can be expressed by

$$\begin{aligned} f_i^{(\mathrm{ES})} &= -\frac{\partial\mathcal{E}}{\partial u_i^*} \\ &= -\frac{\partial}{\partial u_i^*}(\sigma_{ij} S_{ij}^*) \\ &= -\frac{\partial}{\partial j}\left(\frac{\partial j}{\partial u_i^*}\sigma_{ij}\frac{\partial u_i^*}{\partial j}\right) = -\partial_j \sigma_{ij}. \end{aligned} \tag{3.88}$$

These force components are computed for a rectangular suspended silicon nanowire with cross section dimensions 300[nm] × 220[nm] in Fig. 3.7(d-f). We have assumed an intramode BSBS process with the pump mode profiles shown in Fig. 3.7(a-c). Then the energy density — in J/m — calculated over the waveguide cross section is

$$\begin{aligned} \int \delta\mathcal{E}\ ds = Q_1^{(\mathrm{ES})} &= \int \sigma_{ij} S_{ij}^*\ ds \\ &= -\epsilon_0 \int n^4 \tilde{e}_k^{(1)} p_{klij} [\tilde{e}_l^{(2)}]^* \partial_i [u_j]^*\ ds \\ &= \epsilon_0 \int \partial_j (n^4 p_{ijkl} \tilde{e}_k^{(1)} [\tilde{e}_l^{(2)}]^*) u_i^*\ ds. \end{aligned} \tag{3.89}$$

where n is the waveguide refractive index. Equation Eq. (3.89) is identical to the overlap integral of Eq. (3.57) in which the contribution of electrostriction in the waveguide body, away from the boundaries was calculated.

A similar approach can be applied to determine the contribution of the electrostrictive boundary forces. For this, the optical force density due to the electrostriction, $F_i^{(\mathrm{ESP})}$ — in N/m^2 — is

$$F_i^{(\mathrm{ESP})} = -(\sigma_{ij}^{(\mathrm{w})} - \sigma_{ij}^{(\mathrm{b})})n_j, \tag{3.90}$$

where n_j is the normal vector from the background to the waveguide. The force components corresponding to the case of waveguide with fundamental optical mode shown in Fig. 3.7(a-c) are depicted in Fig. 3.8.

Now the contribution of this force in the overlap integral is

$$\begin{aligned} Q_1^{(\mathrm{ESP})} &= \int \mathbf{F}^{(\mathrm{ESP})}.\mathbf{u}^* \; dl \\ &= -\int (\sigma_{ij}^{(\mathrm{w})} - \sigma_{ij}^{(\mathrm{b})})n_j u_i^* \; dl \\ &= \int_{A_2} \Bigg(\mathbf{n}.\big[(\epsilon^{(\mathrm{b})})^2\epsilon_0 \sum P_{ijkl}^{(\mathrm{b})} \partial_k u_l^* e_i^{(1,\mathrm{b})} e_j^{*,(2,\mathrm{b})} \hat{i} \\ &\quad - (\epsilon^{(\mathrm{w})})^2\epsilon_0 \sum P_{ijkl}^{(\mathrm{w})} \partial_k u_l^* e_i^{(1,\mathrm{w})} e_j^{*,(2,\mathrm{w})} \hat{i}\big] \Bigg) \; ds, \end{aligned} \tag{3.91}$$

which is identical to Eq. (3.68).

3.8.2 Radiation pressure

Radiation pressure is an electromagnetic force that appears due to the electric dipoles generated only on dielectric interfaces of a waveguide when light propagates. We here distinguish between the electrostrictive boundary forces and the force due to refractive index discontinuity on the waveguide boundaries.

The radiation pressure can be calculated by knowing the electromagnetic stress. There has been a long debate about the correct expressions for the electromagnetic stress as well as the electromagnetic momentum. We here do not intend to enter this controversy and only present the expression that is in compliance with our derivation for contribution of the radiation pressure in the overlap integral (see section 3.6.2). In previous studies [38, 40] the stress tensor derived by Minkowski was used which only accounts for the radiation pressure on waveguide boundaries. This means that the impact of electrostriction is required to be considered separately on waveguide

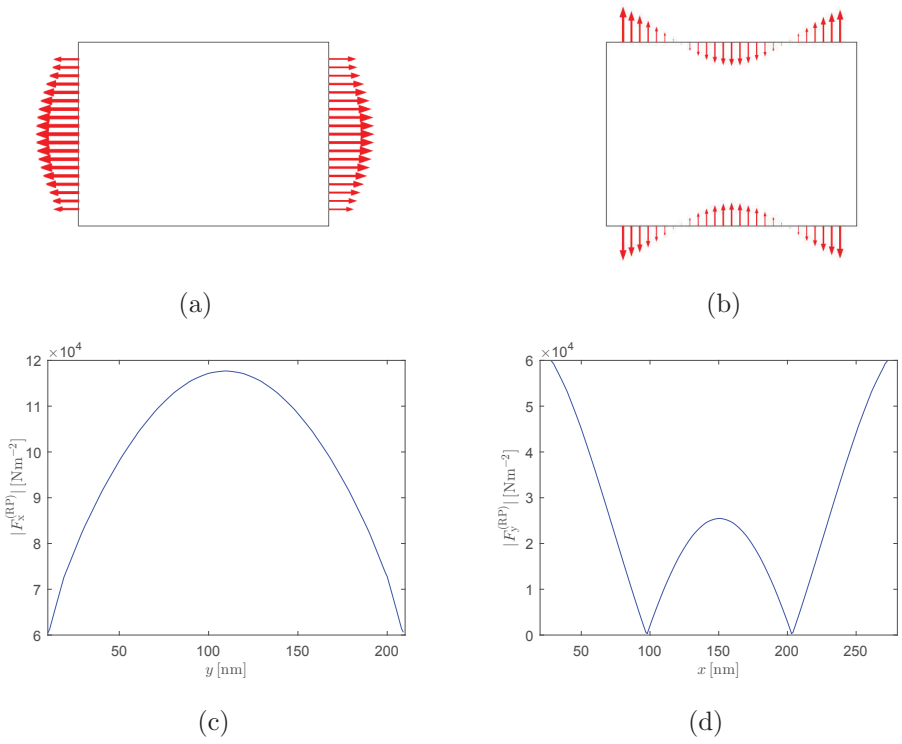

Figure 3.9 : Radiation pressure on boundaries of the suspended silicon waveguide with geometry and optical mode profile described in Fig. 3.7(a-c) in an intra mode BSBS process. (a) and (b) show the relative direction and magnitude of forces $F_{\mathrm{x}}^{(\mathrm{RP})}$ and $F_{\mathrm{y}}^{(\mathrm{RP})}$, respectively. (c) and (d) shows the absolute value of the two forces.

boundaries as demonstrated in the previous subsection. The components of the Minkowski stress tensor take the following form

$$T_{ij} = E_i D_j + H_i B_j - \frac{1}{2}\delta_{ij}(\epsilon_0\epsilon|\mathbf{E}|^2 + \mu_0\mu|\mathbf{H}|^2), \tag{3.92}$$

where E_i,D_j,H_j and B_j are the total electric and magnetic field components, δ_{ij} is the Kronecker delta and $|\mathbf{E}|$ and $|\mathbf{H}|$ are the total electric and magnetic fields denoted by

$$|\mathbf{E}|^2 = \sum_i |E_i|^2, \tag{3.93}$$

$$|\mathbf{H}|^2 = \sum_i |H_i|^2, \tag{3.94}$$

where $i \in \{x, y, z\}$ in Cartesian coordinates. In a non-magnetic waveguide, Eq. (3.92) can be further simplified to

$$T_{ij} = \frac{1}{\epsilon_0\epsilon}(\tilde{D}_i^{(1)}[\tilde{D}_j^{(2)}]^* + \tilde{D}_j^{(1)}[\tilde{D}_i^{(2)}]^*) - \delta_{ij}(\epsilon_0\epsilon\sum_k \tilde{E}_k^{(1)}[\tilde{E}_k^{(2)}]^*), \tag{3.95}$$

Now the optical force due to the radiation pressure can be expressed by

$$F_i^{(\mathrm{RP})} = \sum_j (T_{1ij} - T_{2ij})n_j, \tag{3.96}$$

in which n_j denotes the normal vector of the interface from material 1 to material 2. We use Eq. (3.96) to calculate the overlap integral on waveguide boundaries

$$\begin{aligned} Q^{(\mathrm{RP})} = &\int \mathbf{F}^{(\mathrm{RP})}.\mathbf{U}^*\, dl = \\ &\int_{\mathcal{C}} \big((n.\mathbf{u})(\epsilon^{(\mathrm{w})} - \epsilon^{(\mathrm{b})})\epsilon_0^{-1}(\mathbf{n}.[\tilde{\mathbf{d}}^{(1)}]^*)(\mathbf{n}.\tilde{\mathbf{d}^{(2)}}) + \\ &(\epsilon^{(\mathrm{w})} - \epsilon^{(\mathrm{b})})\epsilon_0(\mathbf{n}\times[\tilde{\mathbf{e}}^{(1)}]^*)(\mathbf{n}\times\tilde{\mathbf{e}}^{(2)})\big)dl. \end{aligned} \tag{3.97}$$

3.9 SBS gain in a translationally invariant waveguide in the steady state

In the stationary state Eq. (3.76),Eq. (3.53) and Eq. (3.54) are simplified to

$$\partial_z b + \alpha_{\mathrm{ac}} b = \frac{i\Omega Q_b}{\mathcal{P}^{(\mathrm{ac})} + i\mathcal{P}^{(\mathrm{ac,loss})}} A^{(1)}[A^{(2)}]^*, \tag{3.98}$$

$$\partial_z A^{(1)} + \frac{i\omega_1 Q_1}{\mathcal{P}^{(1)}} A^{(2)} b = 0, \tag{3.99}$$

$$\partial_z A^{(2)} + \frac{i\omega_2 Q_2}{\mathcal{P}^{(2)}} A^{(1)} b^* = 0. \tag{3.100}$$

We first find the acoustic envelope by solving the first order differential equation in Eq. (3.98)

$$\begin{aligned} b(z) &= \frac{i\Omega Q_b e^{\alpha_{\rm ac} z}}{\mathcal{P}^{(\rm ac)} + i\mathcal{P}^{(\rm ac,loss)}} \int A^{(1)}(z')[A^{(2)}(z')]^* e^{-\alpha_{\rm ac} z'}\, dz' \\ &= \frac{-i\Omega Q_b}{\alpha_{\rm ac}(\mathcal{P}^{(\rm ac)} + i\mathcal{P}^{(\rm ac,loss)})} A^{(1)}(z)[A^{(2)}(z)]^*, \end{aligned} \tag{3.101}$$

where we have assumed that the acoustic attenuation is much stronger than the optical envelope variations. Assuming that the optical mode powers $\mathcal{P}^{(1)}$ and $\mathcal{P}^{(2)}$ are 1 W, we substitute Eq. (3.101) into Eq. (3.53) and Eq. (3.54)

$$\partial_z A^{(1)} = -\mathbb{G}|A^{(2)}|^2 A^{(1)}, \tag{3.102}$$

$$\partial_z A^{(2)} = \mathbb{G}|A^{(1)}|^2 A^{(2)}, \tag{3.103}$$

where $\mathbb{G}$ is known as the SBS envelope gain in m^{-1}

$$\mathbb{G} = \frac{\omega\Omega|Q_{\rm b}|^2}{\alpha_{\rm ac}\mathcal{P}^{(\rm opt)}(\mathcal{P}^{(\rm ac)} + i\mathcal{P}^{(\rm ac,loss)})}, \tag{3.104}$$

where $\mathcal{P}^{(\rm opt)} = \mathcal{P}^{(1)} = |\mathcal{P}^{(2)}| = 1$ W and $\omega_1 \approx \omega_2 = \omega$. Equations (3.102) and (3.103) can also be expressed in terms of pump/Stokes powers.Using Eq. (3.14) we obtain

$$\partial_z P^{(1)} = -gP^{(1)}P^{(2)}, \tag{3.105}$$

$$\partial_z P^{(2)} = gP^{(1)}P^{(2)}, \tag{3.106}$$

where g is the SBS power gain in $\mathrm{W}^{-1}\mathrm{m}^{-1}$ denoted by

$$g = \frac{2\omega\Omega|Q_{\rm b}|^2}{\alpha_{\rm ac}\mathcal{P}^{(1)}\mathcal{P}^{(2)}(\mathcal{P}^{(\rm ac)} + i\mathcal{P}^{(\rm ac,loss)})} \tag{3.107}$$

Similar to Eq. (3.104) the optical modes are assumed to have unit powers. However, we put their notation in the equation to avoid misunderstanding about the unit of g. The SBS gain is also commonly in the literature to be expressed in units of mW^{-1}. This gain can then be determined by multiplying Eq. (3.107) by the waveguide effective mode area $A_{\rm eff}$

$$g'[\mathrm{mW}^{-1}] = gA_{\rm eff}. \tag{3.108}$$

The sign of the SBS gain in Eq. (3.107) depends on the type of SBS process (i.e. backward or forward). In backward SBS, $\mathcal{P}^{(2)} < 0$ and $\{\mathcal{P}^{(1)}, \mathcal{P}^{(ac)}\} > 0$ then $g < 0$. In FSBS, all the normalizing powers are positive which leads to a positive value of g.

Figure (3.10(a)) shows the BSBS gain $|g|$ in the waveguide with the geometry and fundamental optical mode represented in Fig. 3.7(a-c). In order to determine $\alpha_{\rm ac}$, we have assumed that the acoustic Q-factor $Q^{(\rm ac)}$ is 1000, which is a common value for silicon in the literature [38]. Then, assuming a linear acoustic dispersion we have

$$\alpha_{\rm ac} = \frac{q}{Q^{(\rm ac)}}. \tag{3.109}$$

Figure (3.10(b)) compares the contribution of electrostriction — inside the waveguide and on the boundaries — and radiation pressure in the total overlap integral Q_1. As can be seen at $\Omega \approx 80\text{GRads}^{-1}$ the effect of the two optical forces are destructive, hence the total gain is significantly reduced. A similar situation is observed for $\Omega \approx 120\text{GRads}^{-1}$.

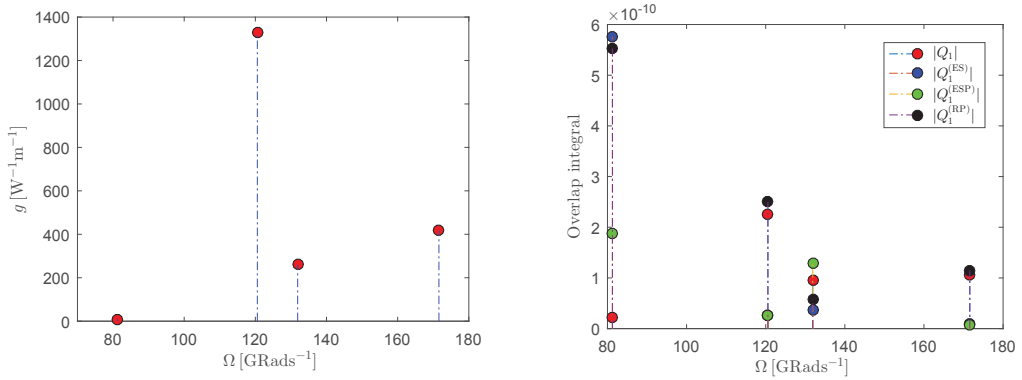

(a) (b)

Figure 3.10 : (a) Backward SBS gain for an intra mode coupling between pump and Stokes in the suspended silicon waveguide. (b) Absolute values of the overlap integrals Q_1, $Q^{(\rm ES)}$, $Q^{(\rm ESP)}$ and $Q^{(\rm RP)}$ for the BSBS process with the SBS gains shown in (a) . In both figures, the waveguide geometry and mode profiles are as shown in Fig. 3.7.

3.10 Coupled equations in the presence of linear loss

So far, we have neglected optical loss in our analysis. In this section we include the impact of linear loss to the coupled wave Eqs. (3.53) and (3.54). For this, we modify the displacement field $\mathbf{D}$ by including the loss terms. $\mathbf{D}$ in Eq. (3.3) can be expressed as [86]

$$\mathbf{D} = \epsilon_0 \mathbf{E} + \mathbf{P}_{\mathrm{L}} + \mathbf{P}_{\mathrm{NL}}, \tag{3.110}$$

where ϵ_0 is the vacuum permittivity and $\mathbf{P}_{\mathrm{L}}$ and $\mathbf{P}_{\mathrm{NL}}$ are the linear and nonlinear polarization vectors

$$\mathbf{P}_{\mathrm{L}}(x,y,z,t) = \epsilon_0 \int_{-\infty}^{t} \chi^{(1)}(t-t')\mathbf{E}(x,y,z,t')\ dt', \tag{3.111}$$

$$\begin{aligned}\mathbf{P}_{\mathrm{NL}} = \mathbf{P}_{\mathrm{NL}}^{(3)} + ... = \epsilon_0 \int_{-\infty}^{t}\int_{-\infty}^{t}\int_{-\infty}^{t} \\ \chi^{(3)}(t-t_1,t-t_2,t-t_3)\vdots\mathbf{E}(x,y,z,t_1)\mathbf{E}(x,y,z,t_2)\mathbf{E}(x,y,z,t_3)dt_1dt_2dt_3 + ...,\end{aligned} \tag{3.112}$$

where $\mathbf{P}_{\mathrm{NL}}^{(3)}$ is the polarization field generated due to the third order nonlinearity; $\chi^{(1)}$ and $\chi^{(3)}$ are first and third order susceptibilities which possess complex values and can be further expanded to their real and imaginary parts

$$\chi^{(n)} = \chi_{\mathrm{r}}^{(n)} + i\chi_{\mathrm{i}}^{(n)}, \tag{3.113}$$

where $\chi_{\mathrm{i}}^{(n)}$ accounts for the optical loss due to the material. The second — and in general even — order nonlinearities are absent in centrosymmetric crystals [87, 84]. In addition, the second order nonlinearity cannot satisfy the phase matching condition (Eq. (2.2)). Therefore, the third order nonlinearity is the lowest order nonlinearity that appears in symmetric crystals. We here specially focus on the third and fifth order effects, as they have considerably stronger impact than those of higher order nonlinearities.

The susceptibility $\chi^{(n)}$ is in general a frequency dependent quantity. In CW regime or quasi-CW — in which the optical pulse width is considerably larger than the electron and nuclei response —, we can assume χ^i to be non-dispersive [88]. Then, Eq. (3.111) and (3.112) reduce to

$$\mathbf{P}_{\mathrm{L}} = \epsilon_0 \chi^{(1)} \mathbf{E}(x,y,z), \tag{3.114}$$

$$\mathbf{P}_{\mathrm{NL}} = \sum_i \mathbf{P}_{\mathrm{NL}}^{(i)} = \epsilon_0 \chi^{(3)} \vdots \mathbf{E}(x,y,z)\mathbf{E}(x,y,z)\mathbf{E}(x,y,z) + ..., \tag{3.115}$$

We now substitute Eq. (3.114) and (3.115) in Eq. (3.110), to include the impact of optical loss in the coupled mode equations. We first assume that the impact of

third and higher order susceptibilities are negligible in a waveguide. This happens in a range of technologically important materials including chalcogenide, silica and silicon nitride in which only linear loss is significant. We then substitute Eq. (3.114) and (3.115) in Eq. (3.110), solve the wave equation Eq. (3.3). After simplifying, the final coupled envelope equations take the following form

$$\partial_z A^{(1)} + \tilde{\alpha}_1 A^{(1)} - (\frac{1}{v_{\mathrm{g}}^{(1)}} - \frac{1}{v_{\mathrm{g}}^{'(\mathrm{p})}})\partial_t A^{(1)} + \frac{i\omega_1 Q_1}{\mathcal{P}_1} A^{(2)} b = 0, \tag{3.116}$$

$$\partial_z A^{(2)} + \tilde{\alpha}_2 A^{(2)} - (\frac{1}{v_{\mathrm{g}}^{(2)}} - \frac{1}{v_{\mathrm{g}}^{'(2)}})\partial_t A^{(2)} + \frac{i\omega_2 Q_2}{\mathcal{P}_2} A^{(1)} b^* = 0, \tag{3.117}$$

where $\tilde{\alpha}_1(\tilde{\alpha}^2)$ is the linear loss coefficient for the pump (Stokes)

$$\tilde{\alpha}_i = -\frac{\omega_{\mathrm{i}} \mathcal{E}_{\mathrm{Loss}}^{(\mathrm{i})}}{2\mathcal{P}^{(\mathrm{i})}}, \tag{3.118}$$

in which $\mathcal{E}_{\mathrm{Loss}}^{(\mathrm{i})}$ is the mode energy per unit of propagation length that is dissipated due to the linear loss

$$\mathcal{E}_{\mathrm{Loss}}^{(\mathrm{i})} = 2\epsilon_0 \int \chi_{\mathrm{i}}^{(1)} |\tilde{\mathbf{e}}^{(\mathrm{i})}|^2 \, ds, \tag{3.119}$$

and the term $v_{\mathrm{g}}^{'(\mathrm{i})}$ is defined as

$$v_{\mathrm{g}}^{'(\mathrm{i})} = \frac{\mathcal{P}^{(\mathrm{i})}}{\mathcal{E}_{\mathrm{Loss}}^{(\mathrm{i})}}. \tag{3.120}$$

In deriving Eqs. (3.116) and (3.117) we have assumed that the displacement field perturbation only appears in the real components of the susceptibilities. Within the stationary state (i.e. $\partial_t = 0$) the coupled envelope equations can now be written as

$$\partial_z A^{(1)} + \tilde{\alpha}_1 A^{(1)} = -\mathbb{G} |A^{(2)}|^2 A^{(1)}, \tag{3.121}$$

$$\partial_z A^{(2)} + \tilde{\alpha}_2 A^{(2)} = \mathbb{G} |A^{(1)}|^2 A^{(2)}, \tag{3.122}$$

The coupled power equation can be obtained in a similar way as illustrated in Section 3.9

$$\partial_z P^{(1)} + \alpha_1 P^{(1)} = -g P^{(1)} P^{(2)}, \tag{3.123}$$

$$\partial_z P^{(2)} + \alpha_2 P^{(2)} = g P^{(1)} P^{(2)}, \tag{3.124}$$

where

$$\alpha_i = 2\tilde{\alpha}_i. \tag{3.125}$$

From Eqs. (3.123) and (3.124) the pump decays exponentially because of linear loss. In addition, the pump envelope also decreases due to the pump depletion to the Stokes (i.e. $-\mathbb{G}|A^{(2)}|^2A^{(1)}$). In practice, however, the impact of optical loss is significantly stronger on the pump than that of pump depletion. This is because in most experiments the Stokes is much smaller than the pump ($|A^{(2)}(z)| \ll |A^{(1)}(0)|$). Therefore, as long as the Stokes takes small values — or in other word, the small signal approximation is satisfied — we can neglect pump depletion. This trend does not apply for SBS lasers as Stokes envelope becomes comparable with the pump. We demonstrate this behavior in detail in Chapter 6 where we describe SBS lasers in ring resonators. Figure 3.11(a) shows the variation of the Stokes envelope due to BSBS in a waveguide with $\alpha = 1\,[\mathrm{dBcm}^{-1}]$ and $L = 4\,\mathrm{cm}$ for three different values of $|gP^{(1)}(0)|$. From the figure, when $|gP^{(1)}(0)| = 15\,[\mathrm{m}^{-1}]$ Stokes power decays steadily. This is because the pump power is below the critical value $|gP^{(1)}_{\mathrm{critical}}(0)| = 35.1798\,\mathrm{m}^{-1}$. As the input pump — or accordingly the SBS gain— approaches the critical value, $P^{(2)}(0)$ increases. When $|gP^{(1)}(0)| = 40\,[\mathrm{m}^{-1}]$ the input pump reaches the critical power. At this point, Stokes is first decreased but in the end is amplified. This loss is exactly canceled by the gain over the length of the waveguide. Finally for $|gP^{(1)}(0)| = 60\,[\mathrm{m}^{-1}]$ the power is well above the critical power, hence the Stokes power is amplified all through the waveguide.

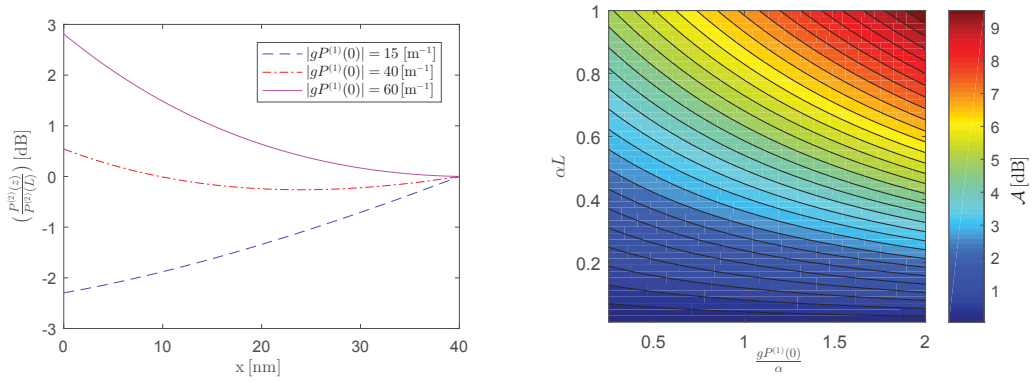

(a) (b)

Figure 3.11 : (a)Variation of Stokes power in BSBS process in a waveguide with $\alpha = 1[\mathrm{dBcm}^{-1}]$, L = 4 cm for $|gP^{(1)}(0)| = \{15, 40, 60\}\,[m^{-1}]$. (b) Stokes amplification $\mathcal{A}$ in [dB] as a function of αL and $\frac{gP^{(1)}(0)}{\alpha}$.

Equation (3.124) shows that the Stokes envelope decays due to the optical loss.

However, it also experiences amplification due to SBS. In the following we solve the coupled power equations assuming the small signal approximation. From Eq. (3.123) the pump power is

$$P^{(1)}(z) = P^{(1)}(0)e^{-\alpha_1 z}, \tag{3.126}$$

where $P^{(1)}(0)$ is the initial pump power launched to the waveguide at $z = 0$. By substituting Eq. (3.126) to Eq. (3.124) and solving the ODE, the Stokes power in BSBS is obtained by

$$P^{(2)}(z) = P^{(2)}(L)\exp[-\alpha_2(z-L) - \frac{gP^{(1)}(0)}{\alpha_1}(e^{-\alpha_1 z} - e^{-\alpha_1 L})], \tag{3.127}$$

where L is the length of the waveguide. The net Stokes amplification can then be expressed by

$$\mathcal{A} = \frac{P^{(2)}(0)}{P^{(2)}(L)} = \exp[\alpha_2 L - \frac{gP^{(1)}(0)}{\alpha_1}(1 - e^{-\alpha_1 L})]. \tag{3.128}$$

The contours in Fig. 3.11(b) shows the achievable Stokes amplification — in dB — as a function of αL and $|\frac{gP^{(1)}(0)}{\alpha_1}|$. In order to achieve amplification, the exponent in Eq. (3.128) must be greater than 1. This condition applies a minimum pump power corresponding to a given nonzero SBS gain and given waveguide length L, that is required to achieve Stokes amplification

$$P^{(1)}_{\text{critical}}(0) = \frac{|\alpha_1 \alpha_2 L|}{|g|(1 - e^{-\alpha_1 L})}. \tag{3.129}$$

Equation (3.129) shows that the pump power required for Stokes amplification is inversely proportional to SBS gain. Additionally, by increasing the waveguide length, the critical pump power increases.

3.11 Coupled equations in the presence of nonlinear loss

We here review the impact of third and fifth order nonlinearities in SBS. These effects have stronger loss effects than higher order nonlinearities in technologically important materials such as silicon which can also satisfy SBS phase matching conditions. Among diverse third order nonlinear processes, impact of Two Photon Absorption (TPA) is important. In TPA, two optical photons, each with an energy less than a direct band gap (E_g) but greater than $E_g/2$ are absorbed and release a free carrier(electron-hole pair), by exciting an electron from valance band to the conduction band [89]. The number of free carriers generated by TPA in a waveguide

provide additional optical absorption [88]. The free carrier induced by TPA is then a fifth order nonlinearity. In semiconductors such as silicon, FCA results in a larger loss than TPA itself.

In the following we include these two effects on coupled wave equations. We start by rewriting (3.2) as

$$\nabla \times \bar{\mathbf{H}} = \partial_t((\epsilon_0\epsilon + i\epsilon_0\chi_i^{(1)})\bar{\mathbf{E}}) + \bar{\mathbf{J}}^{(\mathrm{TPA})} + \bar{\mathbf{J}}^{(\mathrm{FCA})}, \tag{3.130}$$

where ϵ is the real part of the permittivity

$$\epsilon = \left(\chi_{\mathrm{r}}^{(1)} + \chi_{\mathrm{r}}^{(3)}\langle|\bar{\mathbf{E}}|^2\rangle_{T_{ac}} + \chi_{\mathrm{r}}^{(5)}\langle|\bar{\mathbf{E}}|^4\rangle_{T_{ac}}\right). \tag{3.131}$$

Two current densities $\bar{\mathbf{J}}^{(\mathrm{TPA})}$ and $\bar{\mathbf{J}}^{(\mathrm{FCA})}$ are defined in Eq. (3.130). The term $\bar{\mathbf{J}}^{(\mathrm{TPA})}$ denotes the optical loss caused by TPA. $\mathbf{J}^{(\mathrm{TPA})}$ can be expressed in terms of the third order susceptibility

$$\bar{\mathbf{J}}^{(\mathrm{TPA})} = \frac{\epsilon_0\chi_{\mathrm{i}}^{(3)}}{T_{\mathrm{ac}}}\int_{T_{\mathrm{ac}}} |\bar{\mathbf{E}}|^2\, dt. \tag{3.132}$$

The total power loss due to TPA can also be obtained by

$$P^{\mathrm{TPA}} = \int \sum^{\mathrm{TPA}} |\bar{\mathbf{E}}|^4\, dv, \tag{3.133}$$

where the coefficient $\sum^{\mathrm{TPA}}$ — which takes a real value — is defined by

$$\sum^{\mathrm{TPA}} = \epsilon_0\omega\chi_i^{(3)}. \tag{3.134}$$

In the case that Stokes is considerably weaker than pump, the TPA is dominantly of the degenerate type. For silicon at $\lambda = 1550\,\mathrm{nm}$, $\sum^{\mathrm{TPA}} \approx 2.87\times10^{-16}\mathrm{Wm^3V^{-4}}$ (See Appendix 3.14 for the derivation method). In the presence of pump and Stokes signals, the average power density dissipated by TPA is

$$\begin{aligned} P_{\mathrm{den}}^{\mathrm{TPA}} =& \langle\sum^{\mathrm{TPA}} |\bar{\mathbf{E}}|^4\rangle_{\mathrm{Tac}} = \\ & 2\sum^{\mathrm{TPA}}\Big[|A^{(1)}|^4(|\tilde{\mathbf{e}}^{(1)}.\tilde{\mathbf{e}}^{(1)}|^2 + 2|\tilde{\mathbf{e}}^{(1)}|^4) + |A^{(2)}|^4(|\tilde{\mathbf{e}}^{(2)}.\tilde{\mathbf{e}}^{(2)}|^2 + 2|\tilde{\mathbf{e}}^{(2)}|^4) + \\ & 2|A^{(1)}|^2|A^{(2)}|^2(|\tilde{\mathbf{e}}^{(1)}.\tilde{\mathbf{e}}^{(2)}|^2 + |\tilde{\mathbf{e}}^{(1)}|^2|\tilde{\mathbf{e}}^{(2)}|^2 + |\tilde{\mathbf{e}}^{(1)}.[\tilde{\mathbf{e}}^{(2)}]^*|^2)\Big]. \end{aligned} \tag{3.135}$$

The term $\bar{\mathbf{J}}^{(\mathrm{FCA})}$ in Eq. (3.130) is the loss due to the free carriers. In order to derive an expression for $\bar{\mathbf{J}}^{(\mathrm{FCA})}$ we assume that the guiding medium is like a plasma.

Then the current density of free carriers in a plasma can be determined by using the Drude-Sommmerfeld model (for the detail of calculation see the Appendix to Chapter 3 (Section 3.15))

$$\bar{\mathbf{J}}^{(\mathrm{FCA})} = Nq\bar{\mathbf{v}}, \tag{3.136}$$

where N is the carrier concentration, q electron charge and $\bar{v}$ is the carrier mobility. The intrinsic carrier concentration is usually weak enough to be neglected. It originates from thermal excitation of the free carriers from the valance band to the conductance band. However, the free carriers induced by TPA process can significantly increase n in Eq. (3.136). The dynamics of the free carrier concentration is expressed by the continuity equation [88]

$$\partial_t N = \frac{P_{\mathrm{den}}^{\mathrm{TPA}}}{2h\omega} - \frac{N}{\tau}, \tag{3.137}$$

where τ is carrier lifetime, h is Plank's constant and ω is the angular frequency. In the steady state regime (i.e. $\partial_t N = 0$), the free carrier concentration is obtained by

$$N = \frac{\tau}{2h\omega} P_{\mathrm{den}}^{\mathrm{TPA}}. \tag{3.138}$$

By substituting Eq. (3.138) in Eq. (3.136), we find

$$\bar{\mathbf{J}}^{(\mathrm{FCA})} = \frac{\bar{v}\tau}{2h\omega} P_{\mathrm{den}}^{\mathrm{TPA}} \bar{\mathbf{E}}. \tag{3.139}$$

We now use Eq. (3.130) together with the first Maxwell equation in the wave equation (Eq. (3.3)). After simplifying the expressions and dropping the higher order derivatives, the coupled envelope equations in the stationary state take the following form

$$\begin{aligned} &\partial_z A^{(1)} + \left(\tilde{\alpha}_1 + \tilde{\beta}_{11}|A^{(1)}|^2 + 2\tilde{\gamma}_{111}|A^{(1)}|^4\right)A^{(1)} \\ &\quad = -\left(2\tilde{\beta}_{12} + 4\tilde{\gamma}_{112}|A^{(1)}|^2 + 2\tilde{\gamma}_{122}|A^{(2)}|^2\right)|A^{(2)}|^2 A^{(1)} - \frac{i\omega_{\mathrm{p}} Q_1}{\mathcal{P}^{(1)}} A^{(2)} b, \end{aligned} \tag{3.140}$$

$$\begin{aligned} &\partial_z A^{(2)} + \left(\tilde{\alpha}_2 + \tilde{\beta}_{22}|A^{(2)}|^2 + 2\tilde{\gamma}_{222}|A^{(2)}|^4\right)A^{(2)} \\ &\quad = -\left(2\tilde{\beta}_{21} + 4\tilde{\gamma}_{221}|A^{(2)}|^2 + 2\tilde{\gamma}_{211}|A^{(1)}|^2\right)|A^{(1)}|^2 A^{(2)} - \frac{i\omega_{\mathrm{p}} Q_2}{\mathcal{P}^{(2)}} A^{(1)} b^*, \end{aligned} \tag{3.141}$$

where the factor $\tilde{\beta}_{ij}$ is denoted by

$$\tilde{\beta}_{ij} = \frac{1}{\mathcal{P}^{(i)}} \left(\int \sum^{\mathrm{TPA}} \left(|\tilde{\mathbf{e}}^{(i)}.[\tilde{\mathbf{e}}^{(j)}]^*|^2 + |\tilde{\mathbf{e}}^{(i)}.\tilde{\mathbf{e}}^{(j)}|^2 + |\tilde{\mathbf{e}}^{(i)}|^2 |\tilde{\mathbf{e}}^{(j)}|^2 \right) ds, \tag{3.142}$$

in which $\{i,j\} \in \{1,2\}$ and $\tilde{\gamma}_{ijk}$ is

$$\tilde{\gamma}_{ijk} = \frac{1}{\mathcal{P}^{(i)}} \int \sum^{\mathrm{FCA}} |\tilde{\mathbf{e}}^{(i)}|^2 \big(|\tilde{\mathbf{e}}^{(j)}.\tilde{\mathbf{e}}^{(k)}|^2 + |\tilde{\mathbf{e}}^{(j)}|^2 |\tilde{\mathbf{e}}^{(k)}|^2 + |\tilde{\mathbf{e}}^{(j)}.[\tilde{\mathbf{e}}^{(k)}]^*|^2 \big)\, ds. \tag{3.143}$$

The factor $\sum^{\mathrm{FCA}}$ in Eq. (3.143) is defined as

$$\sum^{\mathrm{FCA}} = \frac{\tau \bar{v}}{2\hbar\omega} \sum^{\mathrm{TPA}}. \tag{3.144}$$

For silicon at $\lambda = 1550\,\mathrm{nm}$, $\sum^{\mathrm{FCA}} \approx 1.51 \times 10^{-28}\,\mathrm{Wm^5V^{-6}}$ (See Appendix 3.15). The coupled power equations can be obtained by using the expression of the optical power in Eq. (3.14)

$$\begin{aligned} &\partial_z P^{(1)} + \big(\alpha_1 + \beta_{11} P^{(1)} + \gamma_{111} [P^{(1)}]^2\big) P^{(1)} \\ &\qquad = -\big(2\beta_{12} + 4\gamma_{112} P^{(1)} + \gamma_{122} P^{(2)} + \Gamma\big) P^{(1)} P^{(2)}, \end{aligned} \tag{3.145}$$

$$\begin{aligned} &\partial_z P^{(2)} + \big(\alpha_2 + \beta_{22} P^{(2)} + \gamma_{222} [P^{(2)}]^2\big) P^{(2)} \\ &\qquad = -\big(2\beta_{21} + 4\gamma_{221} P^{(2)} + \gamma_{211} P^{(1)} - \Gamma\big) P^{(1)} P^{(2)}, \end{aligned} \tag{3.146}$$

where the coefficients β_{ij} and γ_{ijk} are

$$\beta_{ij} = \frac{2\tilde{\beta}_{ij}}{\mathcal{P}^{(j)}}, \tag{3.147}$$

$$\gamma_{ijk} = \frac{2\tilde{\gamma}_{ijk}}{\mathcal{P}^{(j)} \mathcal{P}^{(k)}}, \tag{3.148}$$

which take real values and apply the impact of TPA and FCA (or FCA- induced by TPA) in the coupled power equations, respectively. In addition, the SBS power gain Γ is defined in Eq. (3.107) (i.e. $\Gamma = g$).

The loss terms in the left hand side of Eq. (3.145) and Eq. (3.146) are the contribution of linear loss, TPA and FCA in pump and Stokes powers, respectively. The sign of loss terms and Γ in the right hand side of Eq. (3.145) is always similar which means that both of the optical loss and SBS mechanism are reducing pump as it travels through a waveguide. In contrast, Γ always takes a opposite sign to that of loss terms, in the right hand side of Eq. (3.146). We finally note that the factors 2 and 4 in coupled equations are appeared due to the quadratic and cubic dependence of the TPA and FCA to the total electric field in a waveguide (see Eq. (3.135)).

3.11.1 Simplified equations for intramode SBS

We can further simplify Eq. (3.145) and Eq. (3.146) by making certain assumptions about the pump/Stokes optical modes and SBS interaction. In the case of intramode coupling — in both forward and Backward SBS — where pump and Stokes optical modes are identical, Eq. (3.142) and Eq. (3.143) are simplified to

$$\tilde{\beta}_{ij} = \frac{1}{\mathcal{P}^{(i)}}\Big(\int \sum^{\text{TPA}} \Big(|\tilde{\mathbf{e}}^{(i)}.\tilde{\mathbf{e}}^{(i)}|^2 + 2|\tilde{\mathbf{e}}^{(i)}|^4 \Big)\, ds, \tag{3.149}$$

$$\tilde{\gamma}_{ijk} = \frac{1}{\mathcal{P}^{(i)}} \int \sum^{\text{FCA}} |\tilde{\mathbf{e}}^{(i)}|^2 \big(|\tilde{\mathbf{e}}^{(i)}.\tilde{\mathbf{e}}^{(i)}|^2 + 2|\tilde{\mathbf{e}}^{(i)}|^4 \big)\, ds. \tag{3.150}$$

Assuming Forward SBS, where pump and Stokes co-propagate ($\mathcal{P}^{(1)} = \mathcal{P}^{(2)}$),

$$\begin{aligned} \alpha &= \alpha_1 = \alpha_2, \\ \beta &= \beta_{1j} = \beta_{2j}, \\ \gamma &= \gamma_{1jk} = \gamma_{2jk}. \end{aligned}$$

Then, assuming that , Eq. (3.145) and Eq. (3.146) can be rewritten as

$$\partial_z P^{(1)} + \big(\alpha + \beta P^{(1)} + \gamma [P^{(1)}]^2\big) P^{(1)} = -\big(2\beta + 4\gamma P^{(1)} + \gamma P^{(2)} + \Gamma\big) P^{(1)} P^{(2)}, \tag{3.151}$$

$$\partial_z P^{(2)} + \big(\alpha + \beta P^{(2)} + \gamma [P^{(2)}]^2\big) P^{(2)} = -\big(2\beta + 4\gamma P^{(2)} + \gamma P^{(1)} - \Gamma\big) P^{(1)} P^{(2)}. \tag{3.152}$$

Similarly, in the case of Backward SBS($\mathcal{P}^{(1)} = -\mathcal{P}^{(2)}$)

$$\begin{aligned} \alpha &= \alpha_1 = -\alpha_2, \\ \beta &= \beta_{1j} = -\beta_{2j}, \\ \gamma &= \gamma_{1jk} = -\gamma_{2jk}. \end{aligned}$$

3.12 Coupled equations: Solutions in the presence of nonlinear losses

In this section we describe the solution of derived coupled equations represented in Eq. (3.145) and (3.146) in a straight waveguide with length L. In general, the coupled envelope or power equations can be treated via numerical methods. We here assume that all linear and nonlinear loss coefficients are known to us. This requires that we choose those pump and Stokes optical modes which interact through the

SBS. Depending on the SBS process — forward or backward — the appropriate numerical approach differs. In BSBS where pump and Stokes are launched to a waveguide from different ends, the coupled equations form a two point boundary value problem. Among the existing numeric techniques for solving these boundary value problems, two distinct approaches of the shooting method and the relaxation method are used. We describe them in the following.

In FSBS, the pump and Stokes powers are known at $z = 0$. We can apply an iterative shooting method to compute the optical envelopes. The idea is to reduce the existing boundary value problem to an initial value problem, then to solve this iteratively to converge on a solution for which the boundary conditions are satisfied. Specifically, we begin with an estimate of the solution at one of the boundaries; we then "shoot" to the other boundary point by solving the governing differential equations. To do this we first consider the values of the pump and Stokes envelopes at $z = L$ as a two-entry column vector:

$$\mathbf{A} = \begin{bmatrix} A^{(1)}(z = L) & A^{(2)}(z = L) \end{bmatrix}^{\mathrm{T}}. \tag{3.153}$$

We begin by making an initial estimate for this quantity, which label $\mathbf{A}^{(0)}$. Then, we use a numerical technique — such as fourth-order Runge Kutta — to integrate along the waveguide and find the optical envelopes at $z = 0$ where the initial pump and Stokes are launched. The matrix $\mathbf{A}_0$ shows these numerically calculated envelopes

$$\mathbf{A}_0 = \begin{bmatrix} A^{(1)}(z = 0) & A^{(2)}(z = 0) \end{bmatrix}^{\mathrm{T}} \tag{3.154}$$

$$= f_{\mathrm{RK}}(\mathbf{A}). \tag{3.155}$$

where f_{RK} indicates the action of the Runge-Kutta algorithm integrating from $z = L$ to $z = 0$. The envelopes at $z = 0$ are known to us. We set these initial values in matrix $\mathbf{A}_0^{\mathrm{in}}$. If the initial guess for the envelopes at $z = L$ are the true values of pump and Stokes, the computed values of envelopes at $z = 0$ should be equal to the initial values. In general, we can describe the discrepancy between the values obtained using an error function

$$\mathcal{R}(\mathbf{A}) = \mathbf{A}_0 - \mathbf{A}_0^{\mathrm{in}}. \tag{3.156}$$

There are different multidimensional root-finding methods to minimize $\mathcal{R}$. Here we apply the globally convergent Newton's method. In this method the iteration step

for improving the initial guess is

$$\mathbf{A}^{(n+1)} = \mathbf{A}^{(n)} + \begin{bmatrix} J_{11} & J_{12} \\ J_{21} & J_{22} \end{bmatrix} \delta\mathbf{A}^{(n)}, \tag{3.157}$$

where $\delta\mathbf{A}^{(n)} = \begin{bmatrix} \Delta A^{(1)} & \Delta A^{(2)} \end{bmatrix}^{\mathrm{T}}$ at iteration number n. The components of the Jacobian can be found numerically as follows

$$J_{vw} \approx \frac{1}{\Delta A^{(v)}} \Big(\mathcal{R}\big(\mathbf{A}^{(n)} + \begin{bmatrix} \delta_{1w} & 0 \\ 0 & \delta_{2w} \end{bmatrix} \delta\mathbf{A}^{(n)}\big) - \mathcal{R}(\mathbf{A}^{(n)}) \Big), \tag{3.158}$$

where δ_{1w} and δ_{2w} denote the Kronecker delta.

A similar approach can be used in the case of BSBS. In that case the matrix $\mathbf{A}$ is defined by

$$\mathbf{A} = \begin{bmatrix} A^{(1)}(z=L) & A^{(2)}(z=0) \end{bmatrix}^{\mathrm{T}}. \tag{3.159}$$

The advantage of using this numerical method is that it can be used regardless of the type of loss and/or dispersion present in the waveguide.

3.13 Solution in the case of small signal approximation

There are certain situations in which analytic solutions are available for the represented coupled equation. Here, we assume that the Stokes is much smaller than the pump. This assumption enables us to neglect a number of loss terms in Eq. (3.145) and (3.146). We also make another assumption for BSBS equations in this section; in addition to the loss coefficients α, β and γ which are positive, we consider that $P^{(2)} > 0$, and $\Gamma > 0$ for BSBS. Within the Small Signal Approximation (SSA), intra-mode SBS can be expressed by

$$\partial_z P^{(1)} = -\big(\alpha + \beta P^{(1)} + \gamma [P^{(1)}]^2\big) P^{(1)}, \tag{3.160}$$

$$(-1)^n \partial_z P^{(2)} = \alpha P^{(2)} + \big(2\beta + \gamma P^{(1)} - \Gamma\big) P^{(1)} P^{(2)}, \tag{3.161}$$

where $n = 1, 2$ for forward and backward SBS, respectively. We first solve the pump equation to find

$$\begin{aligned} \frac{-1}{2} \ln(\alpha + \beta P^{(1)} + \gamma [P^{(1)}]^2) + \ln P^{(1)} - \frac{\beta}{\sqrt{4\alpha\gamma - \beta^2}} \arctan\Big(\frac{2\gamma P^{(1)} + \beta}{\sqrt{4\alpha\gamma - \beta^2}}\Big) \\ = -\alpha z + C_1', \end{aligned} \tag{3.162}$$

where C_1' is a constant to be determined after applying the boundary conditions. The TPA loss term is usually much weaker than the FCA and linear loss terms. Assuming that $\beta \ll 2\sqrt{\alpha\gamma}$ and $\alpha \ll \gamma$ — which normally occurs — then Eq. (3.162) is simplified to

$$\frac{[P^{(1)}]^2}{\alpha + \beta P^{(1)} + \gamma [P^{(1)}]^2} = C_1 e^{-2\alpha z}, \tag{3.163}$$

which can be used to derive the expression for the pump power

$$P^{(1)} = \frac{-\beta u - \sqrt{(\beta u)^2 - 4\alpha u(\gamma u - 1)}}{2(\gamma u - 1)}, \tag{3.164}$$

where $u = C_1 e^{-2\alpha z}$, with the constant C_1 obtained via

$$C_1 = \frac{[P^{(1)}(z=0)]^2}{\alpha + \beta P^{(1)}(z=0) + \gamma [P^{(1)}(z=0)]^2}. \tag{3.165}$$

We substitute Eq. (3.164) in Eq. (3.161) to find the Stokes power

$$\begin{aligned}(-1)^{(n)} \ln\big(\frac{P^{(2)}(z)}{P^{(2)}_{\text{ini}}}\big) &= \frac{\beta^2}{4\alpha\gamma}\big(\frac{1}{\gamma u - 1} - \frac{1}{\gamma u' - 1}\big) \\ &+ \frac{1}{2}\big(\ln(\frac{\gamma u - 1}{u}) - \ln(\frac{\gamma u' - 1}{u'})\big) + \frac{\beta}{\sqrt{\alpha}}\big(\frac{\sqrt{u(1-\gamma u)}}{1-\gamma u} - \sqrt{u'(1-\gamma u')}1 - \gamma u'\big) \\ &+ \frac{\beta(\Gamma+\beta)}{4\alpha\gamma}\ln\big(\frac{\gamma u - 1}{\gamma u' - 1}\big) + \frac{\Gamma+\beta}{2\sqrt{\gamma\alpha}}\big(\arcsin(2\gamma u - 1) - \arcsin(2\gamma u' - 1)\big),\end{aligned} \tag{3.166}$$

where $P^{(2)}_{\text{ini}} = P^{(2)}(z=0)$ for FSBS and $P^{(2)}_{\text{ini}} = P^{(2)}(z=L)$ for BSBS. In addition, $u' = C_1$ in FSBS and $u' = C_1 e^{-2\alpha L}$ in BSBS.

Figure (3.12) shows the variation of the Stokes power ratio $\frac{P^{(2)}(z)}{P^{(2)}(0)}$ in a FSBS process in a waveguide with $L = 4$cm for different values of SBS gain. As can be seen, for $g = 2500\,\text{W}^{-1}\text{m}^{-1}$ the impact of optical loss (here linear) is dominant and hence prevents Stokes amplification. For $g = 3500 - 4000\,\text{W}^{-1}\text{m}^{-1}$ Stokes is amplified although the maximum amplification is before $z = L$. We will discuss the optimal waveguide length to achieve maximum Stokes amplification.

3.13.1 Case study: Only linear loss and FCA exist in a waveguide

In the case that only linear and FCA loss terms play a role in the coupled equations, the expressions for pump and Stokes powers become much simpler. By assuming $\beta = 0$ in Eq. (3.160) and (3.161), and solving the pump equation, we find

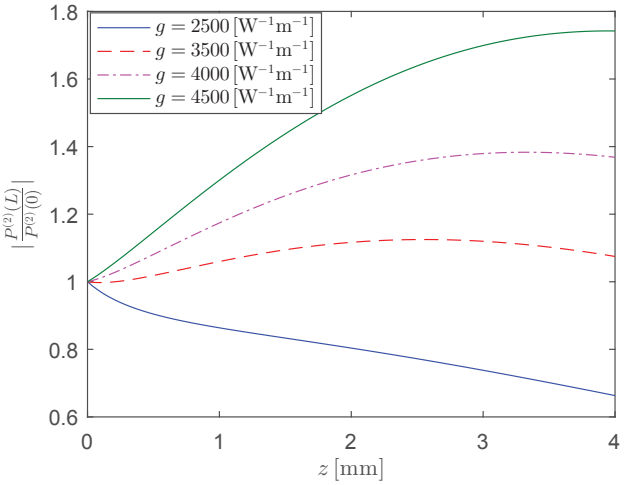

Figure 3.12 : Stokes power variation in a waveguide with $L = 4\,\mathrm{cm}$ in FSBS at different values of SBS gains. Small signal approximation is applied.

$$P^{(1)}(z) = \sqrt{\frac{\alpha}{\gamma}}\frac{1}{\sqrt{(1+U)e^{2\alpha z}-1}}, \tag{3.167}$$

where U is defined as the dimensionless quantity

$$U = \frac{\alpha}{\gamma}\frac{1}{[P^{(1)}(z=0)]^2}. \tag{3.168}$$

To find the Stokes gain we substitute (6.17) into (5.54). We then obtain

$$\begin{aligned}(-1)^n \ln\left(\frac{P^{(2)}(z)}{P^{(2)}_{\mathrm{ini}}}\right) = -\alpha z' + \frac{1}{2}\ln\big(\frac{U}{1+U-e^{-2\alpha z'}}\big) - \\ 2\mathcal{F}(\arctan(\sqrt{U}) - \arctan\big(\sqrt{(1+U)e^{2\alpha z'}-1}\big)),\end{aligned} \tag{3.169}$$

where $z' = L$ in FSBS and $z' = 0$ in BSBS. In addition, $\mathcal{F}$ denotes the SBS figure of merit as introduced in [48]

$$\mathcal{F} = \frac{\Gamma}{2\sqrt{\alpha\gamma}}. \tag{3.170}$$

Figures (3.13(a)) and (3.13(b)) show the Stokes amplification in BSBS as a function of αL and U for $\mathcal{F} = 1.5$ and $\mathcal{F} = 2$, respectively. The two figures clearly show that in the presence of nonlinear loss, there exist optimal parameters corresponding to each value of αL for which the Stokes amplification is maximum.

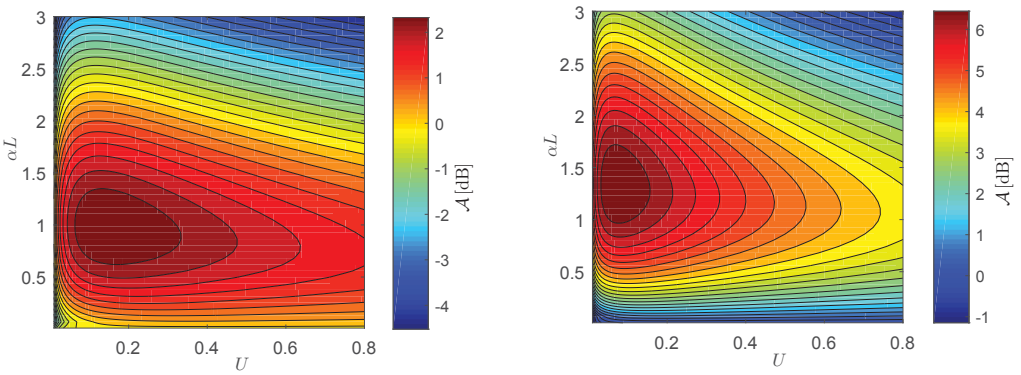

(a) (b)

Figure 3.13 : contours of Stokes amplification for a waveguide with (a) $\mathcal{F} = 1.5$ and (b) $\mathcal{F} = 2$ for a range of αL and U.

3.14 Appendix: Derivation of the coefficient $\sum^{\text{TPA}}$

In the following we derive an expression for $\sum^{\text{TPA}}$ in a bulky waveguide where optical modes propagate as a plane wave. We express the electric and magnetic components of a plane wave propagating along z as

$$\begin{aligned} \mathbf{E} &= \tilde{\mathbf{e}}^{(1)} + c.c \\ &= \frac{\eta}{2} e^{i\beta_1 z - i\omega_1 t} \hat{\mathbf{x}} + c.c, \end{aligned} \tag{3.171}$$

$$\begin{aligned} \mathbf{H} &= \tilde{\mathbf{h}}^{(1)} + c.c \\ &= 2e^{i\beta_1 z - i\omega_1 t} \hat{\mathbf{y}} + c.c, \end{aligned} \tag{3.172}$$

where η is the plane wave impedance denoted by

$$\eta = \sqrt{\frac{\mu_0}{\epsilon_0 \epsilon}}. \tag{3.173}$$

The envelope magnitude is chosen such that $\mathcal{P}^{(1)} = 1\,\text{W}$ in the cross section area $A = 1\text{m}^2$. Now by substituting into Eq. (3.147)

$$\begin{aligned} \beta_{11} &= \frac{2}{[\mathcal{P}^{(1)}]^2} \left(\int_A \sum^{\text{TPA}} \left(|\tilde{\mathbf{e}}^{(i)}.\tilde{\mathbf{e}}^{(i)}|^2 + 2|\tilde{\mathbf{e}}^{(i)}|^4 \right) ds \right. \\ &= \frac{\eta^2}{2} \int_A (2 \times 1 \times 1 + 1) \sum^{\text{TPA}} ds \\ &= \frac{3}{2} \eta^2 \sum^{\text{TPA}}, \end{aligned} \tag{3.174}$$

By rearranging Eq. (3.174) we obtain

$$\sum^{\text{TPA}} = \frac{2\beta_{11}}{3\eta^2}. \tag{3.175}$$

In the case of silicon, the value of β_{11} is measured to be $\beta_{11} = 5 \times 10^{-12}\text{mW}^{-1}$ [88]. Then by substituting in Eq. (3.175)

$$\sum^{\text{TPA}} = 2.87 \times 10^{-16}\,\text{Wm}^3\text{V}^4.$$

3.15 Appendix: Derivation of the coefficient $\sum^{\text{FCA}}$

The expression for the current density $\mathbf{J}^{\text{FCA}}$ in Eq. (3.136) is considered by assuming that the free carrier conductivity of a propagation medium behave like a plasma and therefore its properties can be characterized by Drude-Sommerfeld model. The carrier mobility $\bar{\mathbf{v}}$ is then expressed by

$$\bar{\mathbf{v}} = \frac{\gamma' q}{m(\omega^2 + (\gamma')^2)}\bar{\mathbf{E}}, \tag{3.176}$$

where γ' and m are material specifics. By substituting Eq. (3.176) into Eq. (3.136), the factor $\sum^{(}\text{FCA})$ is expressed by

$$\sum^{(\text{FCA})} = \frac{\gamma' q \tau}{2h\omega m(\omega^2 + (\gamma')^2)}. \tag{3.177}$$

In the case of silicon $\sum^{\text{TPA}} \approx 2.87 \times 10^{-16}\text{Wm}^3\text{V}^{-4}$ which is obtained by assuming the free carrier lifetime $\tau = 10\,\text{ns}$ which is reported for silicon at $\lambda = 1550\,\text{nm}$ [48]. We note that the carrier lifetime depends on material and waveguide geometry [90].

Chapter 4

SBS in hybrid slot waveguides

Figure 4.1 : Schematic of a silicon chalcogenide slot waveguide

This Chapter is based on the following paper:
Sayyed Reza Mirnaziry, Christian Wolff, MJ Steel, Benjamin J Eggleton, and Christopher G Poulton. Stimulated Brillouin scattering in silicon/chalcogenide slot waveguides. *Optics Express*, 24(5):4786–4800, 2016.

4.1 Introduction

A promising approach to co-localize optical and acoustic waves is to use multimaterial structures, whereby the mechanical or optical strengths of one material compensate for the corresponding weakness of the other. Within this category of multimaterial structures, slot waveguides, in which a large electric field can be concentrated within in a small area containing a material with a high nonlinearity and a relatively low refractive index, are particularly promising candidates [91]. Reports have shown that strong SBS gain, driven by radiation pressure, can theoretically be achieved in suspended silicon slot waveguides with an air gap between them [39]. Non-suspended slot waveguides, i.e. placed on a substrate, have previously been proven to significantly enhance nonlinearities in nanophotonic waveguides [39], have

a stable mechanical configuration and can be fabricated with current technology. An open question is whether material systems or parameters can be found such that useful SBS gain can be achieved in a non-suspended slot waveguide.

In this chapter, we study numerically and analytically SBS in hybrid silicon-chalcogenide slot waveguides. Chalcogenides are soft glasses with high nonlinearity and good acousto-optical properties that have been used in a number of applications [2]. We show that strong optical and acoustic mode confinement in a silicon-chalcogenide slot waveguide leads to a substantially increased SBS gain relative to suspended silicon structures [39, 38]. We optimize the waveguide dimensions for maximal gain and show that gains of up to 3300 $\mathrm{W}^{-1}\mathrm{m}^{-1}$ can be achieved in these geometries that is comparable to the gain of suspended silicon nanowire waveguides [38]. Additionally, we demonstrate that under certain conditions radiation pressure has no net effect on the gain. We show that increasing the structure symmetry can lead to further confinement of acoustic waves in the slot gap, thereby both increasing the SBS gain and leading to greater stability and protection against environmentally-induced losses. We analyze the conditions under which acoustic waves leak to the substrate, and examine this effect on the parameters available for SBS waveguide design. Furthermore, we examine the effect of losses on the SBS Stokes amplification, including the linear loss as well as nonlinear losses of two photon absorption (TPA) and TPA-induced free carrier absorption (FCA). We finally determine optimum pump and Stokes powers for initializing the SBS process as well as the optimum length for the designed waveguide.

4.2 Formalism

In the following we outline the formalism for computing SBS gain, in which the optomechanical coupling term is formulated using optical forces. A full discussion of the computation of SBS gain for high-contrast waveguides can be found in [92].

4.2.1 Definitions and gain

In SBS, pump photons with angular frequency of ω_p are red-shifted to Stokes photons with angular frequency ω_s ($\omega_s < \omega_p$) and simultaneously phonons with an angular frequency Ω are generated. Momentum and energy conservation determine

how optical/acoustic frequencies and wavenumbers are interrelated:

$$\Omega = \omega_p - \omega_s, \tag{4.1}$$

$$q = \beta_p - \beta_s, \tag{4.2}$$

where q, β_{p} and β_{s} are the acoustic, optical pump and Stokes wavenumbers, respectively [39].

The pump and Stokes waves can co-propagate (Forward SBS, FSBS)- or contra-propagate (Backward SBS, BSBS). They can also carry different optical modes (intermode coupling) or identical modes (intramode coupling) [38]. In the following, we choose the case of BSBS as an example. The governing equations for the optical powers, taking into account optical loss, are [48] (See Section 3.11)

$$\frac{\partial P_p}{\partial z} + (\alpha_p + \beta P_p + \gamma P_p^2)P_p = -(2\beta + 4\gamma P_p + \gamma P_s + \Gamma)P_p P_s, \tag{4.3}$$

$$\frac{\partial P_s}{\partial z} + (\alpha_s + \beta P_s + \gamma P_s^2)P_s = -(2\beta + 4\gamma P_s + \gamma P_p - \Gamma)P_p P_s, \tag{4.4}$$

where P_p and P_s are the pump and Stokes powers, respectively, and Γ is the SBS gain. The coefficients α_p, α_s, γ and β correspond to linear and nonlinear optical losses (See Section 3.11.1). According to Eqs. (4.3,4.4) the pump decreases continuously along the direction of propagation (the z-axis), while the Stokes wave grows in the opposite direction. In practice, however, the Stokes amplification is limited by optical losses. Therefore, the SBS gain should be large enough to compensate losses and amplify Stokes. The SBS gain is given by [92](See 3.107)

$$\Gamma = \frac{2\Omega\omega|Q_c|^2}{\alpha_{ac}\mathcal{P}^{\mathrm{p}}\mathcal{P}^{\mathrm{s}}\mathcal{P}^{\mathrm{ac}}}, \tag{4.5}$$

where ω is the angular optical frequency ($\omega_p \approx \omega_s = \omega$) and α_{ac} is acoustic decay parameter. The pump, Stokes and acoustic modes are assumed to be normalized to the unit powers $\mathcal{P}^{\mathrm{p}}$,$\mathcal{P}^{\mathrm{s}}$ and $\mathcal{P}^{\mathrm{ac}}$, respectively. The overlap integral Q_c expresses the interaction between optical force $\mathbf{F}$ and acoustic displacement fields $\mathbf{u}$. Q_c is given by [92](See Section 3.7)

$$Q_c = \int \mathbf{F} \cdot \mathbf{u}^* \mathrm{dA}, \tag{4.6}$$

in which the integral extends over the waveguide cross section.

4.2.2 Optical parameters of SBS gain

Two dominant forces with comparable magnitudes co-exist in nonmagnetic integrated waveguides; electrostriction and radiation pressure [10]. Both forces depend

Table 4.1 : Related permittivity, photo-elastic coefficients– in Voigt notation – and material symmetry of materials used in the proposed structures [38].

Material 1	Relative permittivity ϵ_r	Photoelastic coefficients p_{11}	p_{12}	p_{44}	material symmetry
Si	12.25	-0.09	0.017	-0.051	Cubic
As_2S_3	5.65	0.25	0.24	0.005	Amorphous
SiO_2	2.25	0.121	0.27	-0.075	Amorphous

quadratically on the electric field. Electrostriction is the quadratic response of mechanical strain to an applied electric field and can be observed in all materials [84]. The i^{th} component of the electrostrictive force can be found by [40](See Section 3.8)

$$F_i = -\sum_{ij} \frac{\partial}{\partial j}\sigma_{ij}, \tag{4.7}$$

where σ_{ij} is the electrostrictive stress given by

$$\sigma_{ij} = -\frac{1}{2}\epsilon_0\epsilon_r^2 \sum_{kl} p_{ijkl}E_kE_l, \tag{4.8}$$

with the relative permittivity ϵ_r and the fourth rank photoelastic tensor p_{ijkl}. The sum extends over all Cartesian field components. The electric field E_k in Eq. (4.8) is of the form

$$E_k = \{a_p(z,t)\tilde{E}_k^{(p)}e^{(\mathrm{i}\beta_\mathrm{p}\mathrm{z}-\mathrm{i}\omega_\mathrm{p}\mathrm{t})} + a_s(z,t)\tilde{E}_k^{(s)}e^{(\mathrm{i}\beta_\mathrm{s}\mathrm{z}-\mathrm{i}\omega_\mathrm{s}\mathrm{t})}\} + \text{c.c.}, \tag{4.9}$$

where $\tilde{E_k}^{(p)}$ and $\tilde{E_k}^{(s)}$ are the k^{th} component of pump and Stokes electric field modes and $a_p(z,t)$ and $a_s(z,t)$ are the corresponding optical mode envelopes [92]. The optical properties of materials used in the proposed waveguides of our paper are given in Table 4.1 [40].

Radiation pressure acts only on boundaries where electric/magnetic properties change. Unlike electrostriction – which appears in the bulk – radiation pressure is an edge effect. The components of this force are expressed as [38](See Section 3.8)

$$F_i = \sum_j (T_{2ij} - T_{1ij})n_j, \tag{4.10}$$

where n_j is the normal vector of the interface from material 1 to material 2 and T_{ij} are the components of Maxwell's stress tensor

$$T_{ij} = \epsilon_r \epsilon_0 (E_i E_j - \frac{1}{2}\delta_{ij}|\mathbf{E}|^2) + \mu_r \mu_0 (H_i H_j - \frac{1}{2}\delta_{ij}|\mathbf{H}|^2), \tag{4.11}$$

where $\mathbf{E}$ and $\mathbf{H}$ are the total electric and magnetic fields, respectively. For translationally invariant waveguides, only the transverse components of this force with respect to the waveguide direction contribute to SBS.

It may be expected that waveguides with high refractive index materials provide strong optical forces that lead to high SBS gains [Eq. (4.8)]. However, the situation is more complex. First, dielectric materials with high refractive index do not necessarily exhibit a strong photoelastic effect. Second, optical forces might cancel each other on waveguide boundaries. This situation might occur because electrostriction and radiation pressure are of similar order of magnitude in integrated waveguides. Third, a large overlap integral (Q_c) is the result of constructive contribution of both optical forces and acoustic displacement fields. Therefore, even if the forces are strong, weak acoustic fields lead to a small Q_c. Consequently, the acoustic properties of the propagation medium and the acoustic mode profiles play a significant role in enhancing SBS interactions.

The acoustic waves in waveguides are excited within SBS by optical forces that satisfy the phase matching condition (Eqs. (4.1) and (4.2)). The corresponding waves satisfy the acoustic wave equation [80](See Section 3.3):

$$\rho \frac{\partial^2 u_i}{\partial t^2} = \left(\sum_{jkl} \frac{\partial}{\partial j} \left(C_{ijkl} S_{kl} + \eta_{ijkl} \frac{\partial S_{kl}}{\partial t} \right) \right) + F_i, \tag{4.12}$$

where u_i, S_{kl} and F_i are the components of acoustic displacement fields, the mechanical strain tensor and the driving force, respectively and ρ, C_{ijkl} and η_{ijkl} denote the mass density, the stiffness and the viscosity coefficients of the propagation medium [80]. The viscosity damping defines the linewidth of the SBS response. The displacement fields therefore attenuate with the damping coefficient α_{ac} throughout the waveguide length

$$\alpha_{ac} = \frac{\Omega \mathcal{E}^{\mathrm{ac}}}{Q \mathcal{P}^{\mathrm{ac}}}, \tag{4.13}$$

where $\mathcal{E}^{\mathrm{ac}}$ is the energy of the acoustic mode per unit length of waveguide and Q is the mechanical quality factor. For acoustic waves traveling longitudinally in an axially invariant waveguide Eq. (4.13) can be simplified to $\alpha_{ac} = q/Q$ where we

Table 4.2 : Material density and stiffness constants– in Voigt notation – for materials used in the proposed structures[80].

Material	Density	Stiffness constants		
	ρ[Kg/m^3]	C_{11}[Pa]	C_{12}[Pa]	C_{44}[Pa]
Si	2329	2.17×10^{11}	4.83×10^{10}	6.71×10^{10}
As_2S_3	3210	2.10×10^{10}	8.36×10^{9}	6.34×10^{9}
SiO_2	2201	7.85×10^{10}	1.61×10^{10}	3.12×10^{10}

have assumed that acoustic dispersion is linear. The mechanical quality factor in complicated waveguide structures is frequency dependent and can be approximately measured, for example by observing the spectra of Stokes waves of a chip-scale structure [93]. We assume a Q-factor of 1000, which has been used in Ref. [38, 94], to compare our results with these related works. The critical acoustic properties of materials used in our proposed waveguides are listed in Table 4.2.

4.3 Slot waveguide on substrate

We begin by describing the main characteristics of a hybrid silicon-chalcogenide glass slot waveguide. As can be seen in Fig. 4.2, the slot is composed of two identical silicon beams placed on a SiO_2 substrate. The gap is filled with As_2S_3 glass. We assume that the waveguide is axially infinite; We will apply limitations on power and waveguide length in Section 5.

The high index of silicon provides optical confinement in the slot. To provide acoustic confinement, one should add a less stiff material than silica in the slot or the acoustic waves will leak into the substrate. For this purpose, we choose As_2S_3 glass which has low stiffness constants (see Table 4.2), however other choices of soft glass are possible. The silica substrate makes the structure stable and realistic. It should be noted that the presence of a substrate prevents the confinement of standing acoustic phonons required for forward SBS.

Among several optical modes that can propagate in the structure, the fundamental mode with the mode profile shown in Fig. 4.2 is interesting as it has comparatively large intensity in the gap. This results in a strong overlap between the optical and acoustic fields. To find the modes in the waveguide we have used the finite element solver COMSOL. We here focus on the situation of intramode coupling between the

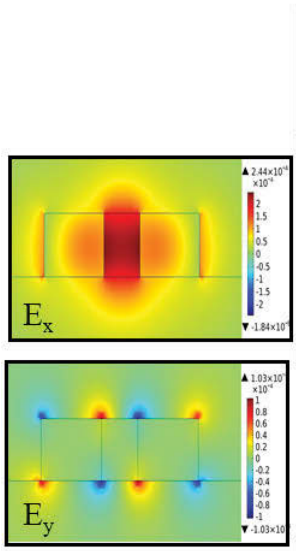

	U_x	U_y	U_z	Acoustic Frequency [GHz]
Mode 1				5.53
Mode 2				7.11
Mode 3				7.48

Figure 4.2 : Hybrid silicon chalcogenide slot waveguide on a silica substrate. Top panel: sketch of the geometry. Bottom panel: The transverse profile of the fundamental optical mode as well as the displacement field components and the acoustic frequency of three lowest order acoustic modes that can propagate in the waveguide. The waveguide dimensions are $a = 250\,\text{nm}$, $b = 190\,\text{nm}$ and $c = 150\,\text{nm}$.

pump and Stokes waves where both waves are in the fundamental mode.

At the optical wavelength $\lambda = 1550$ nm several acoustic modes can be excited. The lowest order modes are shown in Fig. 4.2. As can be seen in the figure, the acoustic modes are mainly localized in the gap. It is possible to excite any acoustic modes that satisfy the phase matching conditions and have appropriate symmetry [95]. However, it should be noted that only a few modes can produce large amount of gain. In Fig. 4.3 the total SBS gain of the slot waveguide shown in Fig. 4.2 is depicted for the acoustic modes. According to the gain results, one can

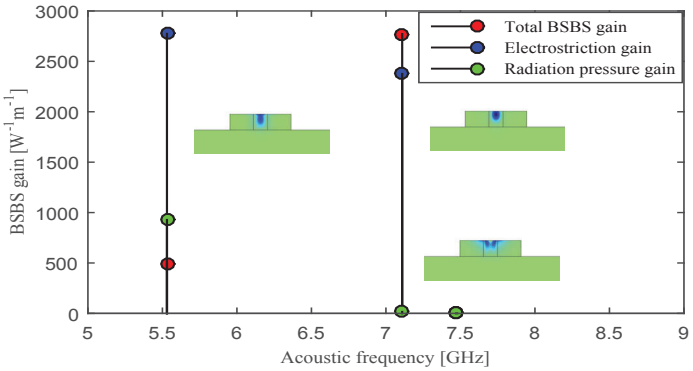

Figure 4.3 : BSBS gain of the acoustic modes described in Fig.4.2. The gain is obtained by assuming the acoustic quality factor of 1000. The profile of acoustic power is shown for the three lowest modes.

see that although the geometry, pump and Stokes powers and optical frequency are identical for all 3 modes, SBS gain is severely affected by the mode profiles. While the third mode produces no gain the mode at $f = 7.11$ GHz in Fig. 4.2 provides the largest amount of gain of all the modes. We choose this mode and determine SBS gain in the slot.

We first study the effect of gap size on the SBS gain. We assume that the dimensions of the silicon beams are fixed at a = 250 nm and b = 190 nm and the gap width varies. The SBS gain is shown in Fig. 4.4(a). In the figure, the total SBS gain that includes the contribution of both electrostriction and radiation pressure is shown as a red curve for gap widths ranging from 90 nm to 260 nm. The SBS gain due to the contribution of the optical forces are depicted for comparison.

We see in Fig. 4.4(a) that the overall gain in the slot waveguide is mainly the re-

sult of electrostrictive forces. The gain of radiation pressure is small but in combination with electrostriction, it considerably modifies the total gain due to the quadratic dependence of the gain to the overlap integral, Q_c [see Eq. (4.5)]. The total gain rises steeply from 965 $W^{-1}m^{-1}$ for $c = 85\,nm$ to 3020 $W^{-1}m^{-1}$ for $c = 200\,nm$ then it falls off gradually as the gap width is further increased. This decreasing trend can be understood by noticing that the optical/acoustic field intensities decrease in the slot region as its width is increased and hence, reduces the overlap integral Q_c. At $c = 200\,nm$ the gain has a value comparable with the values reported for silicon nanowires [38].

We observe a cutoff in the gain as the gap width reduces to c = 85 nm. This happens as a result of hybridization of the acoustic mode with Rayleigh surface waves. To understand the impact of the silica substrate through mode hybridization it is helpful to study how the acoustic frequency changes as the gap width is reduced.

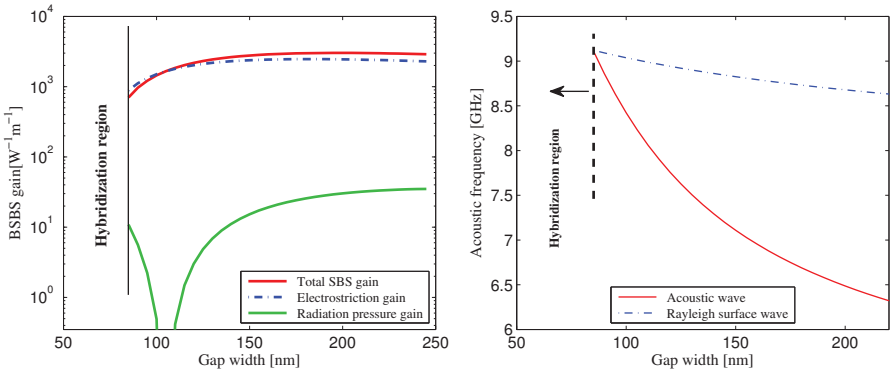

(a) (b)

Figure 4.4 : (a) BSBS gain (red graph) in slot waveguide with $a = 250\,nm$ and $b = 190\,nm$ in a logarithmic scale . Gain is obtained only for the high gain acoustic mode. The green (blue) curve shows the gain when only radiation pressure (electrostriction) is considered in calculations. (b) Variation of acoustic frequency of the acoustic mode with slot gap width (blue curve) in Rayleigh surface waves. The red curve shows variations of the frequency as the slot gap varies from 240 nm to 85 nm assuming that $a = 250\,nm$ and $b = 190\,nm$.

The blue curve in Fig. 4.4(b) shows the frequency of the Rayleigh surface waves corresponding to the acoustic wave number assuming the substrate to be semi-infinite. The red curve represents the frequency of guided acoustic modes. As the gap width decreases the guided mode approaches the Rayleigh waves' dispersion

curve until both curves intersect at 85 nm. In practice the meeting point would be slightly offset since the dispersion of surface waves is modified by the presence of the slot. This means that the acoustic mode inside the gap hybridizes with the acoustic surface mode and hence SBS gain drops heavily (Fig. 4.4(a)). Hybridization of confined acoustic modes in the gap with the acoustic surface waves also prevents FSBS occurring in the slot structure shown in Fig. 4.2.

4.3.1 Cancellation of radiation pressure

An interesting point in Fig. 4.4(a) is that at $c \approx 130$ nm the total gain becomes equal to the electrostriction gain. This means that the radiation pressure has no effect on the overall gain. To explain this we look at the interactions between force components and acoustic mode. Figure 4.5(a) shows the transverse components of the Maxwell stress tensor. The corresponding optical forces appear on the waveguide boundaries where the gradient of the Maxwell stress tensor is nonzero. In Fig. 4.5(b) the green and black arrows show the transversal acoustic displacement field $\mathbf{u}$ and the transverse components of the Maxwell stress tensor T_{xx} and T_{yy}.

The distribution of the force and displacement fields are shown in Fig. 4.5(b). As a rough approximation we assume that an average optical force as well as average acoustic fields exist at each boundaries as shown in the figure. As can be seen in Fig. 4.5(a) the applied force $\mathbf{F}$ on the vertical walls of gap interact with corresponding displacement fields that leads to $\int \mathbf{F} \cdot \mathbf{u}^* dy > 0$. Similarly, $\int \mathbf{F} \cdot \mathbf{u}^* dx < 0$ on top and bottom of the slot. Thus, the overlap integral encounters a destructive contribution of radiation pressure and the acoustic displacement fields on the slot boundaries.

By assuming a constant pump and Stokes power, if the gap width increases, the field intensities and hence their corresponding optical and acoustic power densities decrease. Consequently, the overlap integral falls at each boundary [Fig. 4.5b (left)]. However, as the gap width increases, the overlap integral does not change considerably on these walls. In contrast, on the vertical boundaries not only the product density has decreased, but also the value of overlap integral is decreased [Fig. 4.5b (right)]. Thus, at a particular gap width, the value of overlap integral on the horizontal boundaries exactly cancels that of the vertical walls.

4.3.2 Geometry optimization

Thus far, we have assumed that the silicon beams in our structure have fixed dimensions. We now seek the optimum size of the waveguide to deliver maximum

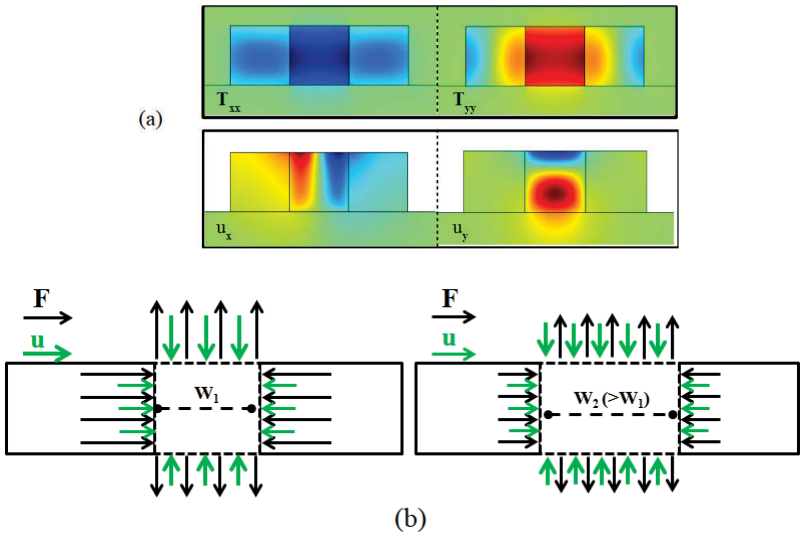

Figure 4.5 : Interactions of radiation pressure and acoustic displacement fields in the overlap integral. (a) The transverse boundary forces due to Pressure (i.e T_{xx} and T_{yy}). (b) The product of $\mathbf{F} \cdot \mathbf{u}^*$ is positive (negative) in vertical (horizontal) gap wall, regardless of the gap width. As the gap width increases, $\int \mathbf{F} \cdot \mathbf{u}^* dy$ decreases on the vertical walls [see Fig. 4.5.b (right and left)]. However, the integral does not change on horizontal walls i.e reduction in the overlap integral is compensated as the gap width is enlarged.

SBS gain. We keep the configuration symmetry (i.e similar silicon beams) so that only three free parameters remain for the optimization: silicon width, height and the gap width. We concentrate on two situations: First, the waveguide height is fixed at 220 nm (a realizable dimension with current fabrication technology) and we vary the beam and gap. Second, we fix the gap width at 200 nm and seek optimum dimensions for the silicon beams. The results are shown in Fig. 4.6(a,b).

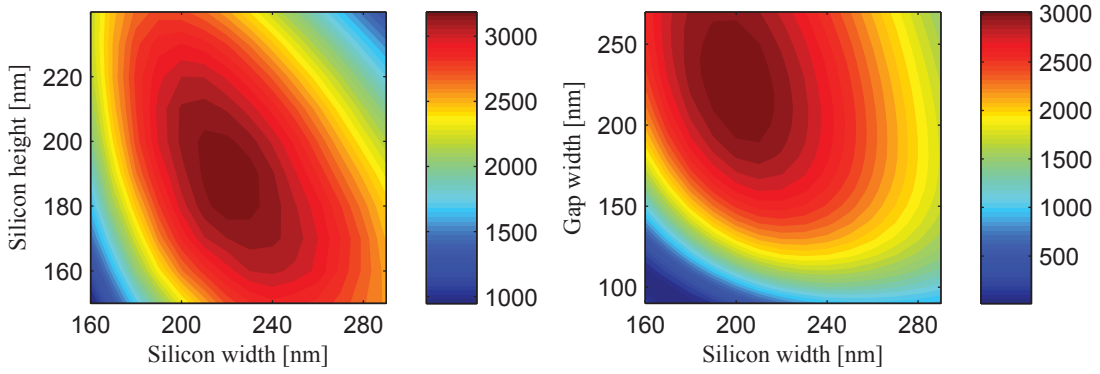

Figure 4.6 : BSBS gain in [$W^{-1}m^{-1}$] for a slot waveguide with (a) $c = 200\,nm$ and (b) $b = 220\,nm$.

One can see that high SBS gains up to about 3300 $W^{-1}m^{-1}$ can be achieved from the slot waveguide. We note that by increasing the gap width the optical and acoustic power densities are decreased in the gap which cause reduction in the total BSBS gain. However, the total powers increase in the gap. This variation — in the distribution of the modal fields — is shown in Fig. 4.7 where the normalized optical and acoustic field components E_z and U_z together with the optical and acoustic power densities are represented.

4.4 Slot waveguides with silica cover

We have seen (Fig. 4.4(a)) that the gain in the slot waveguides mainly comes from the effect of electrostriction. Since the relevant acoustic mode is largely longitudinal the term $F_z u_z^*$ forms the dominant contribution to the overlap integral Q_c in Eq. (4.5). This suggests a way to enhance the overlap integral and hence increase the gain. As we see in Fig. 4.8, F_z is symmetric and is mainly concentrated in the middle of the gap. That is because the small difference between the refractive index of silica and air causes the optical fields and their corresponding forces to be distributed

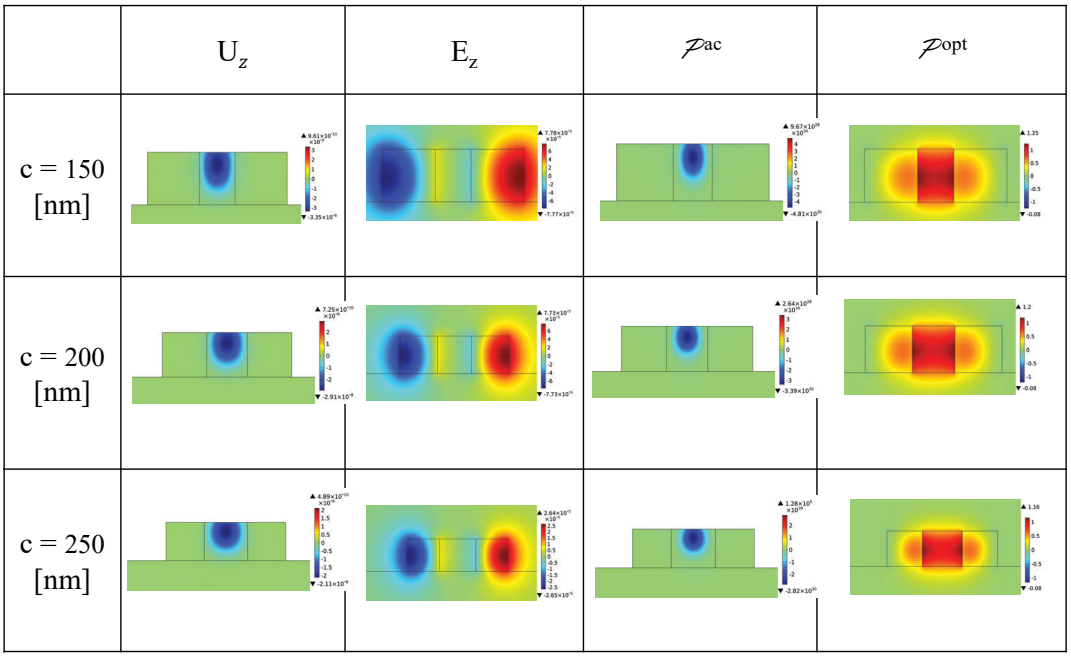

Figure 4.7 : Profiles of optical and acoustic modes corresponding to the largest BSBS gain in a silicon chalcogenide slot waveguide with $a = 220\,\text{nm}$ and $a = 220\,\text{nm}$ at the the gap widths c =150 nm, 200 nm and 250 nm. The field components are normalized to 1 W.

almost symmetrically -with a slight tendency toward the substrate. In contrast, a considerable vertical asymmetry in acoustic fields is observable (Fig. 4.8). Since the

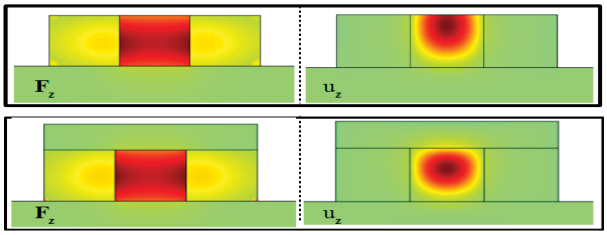

Figure 4.8 : Transverse profile of the electrostrictive force component F_z (left) and the acoustic displacement field u_z for a slot waveguide and a slot with silica cover. It is clearly visible that the SiO_2 cover shifts the maximum of u_z down to the slot center.

acoustic field intensity is large on open boundaries u_z is concentrated mainly toward the upper gap boundary. However this component (u_z) interacts with an optical force component that is not strong on top of the gap. A similar weak interaction happens between the electrostrictive force and displacement field in the middle of gap.

The contribution to Q_c can be increased by adding a silica layer on top of the slot. The displacement fields then shift down toward the gap center, thereby increasing the interaction [Fig. 4.8].

In Fig. 4.9 one can see that the gain is increased markedly by increasing the covering layer thickness. The maximum gain is increased from about 3020 $W^{-1}m^{-1}$ for an ordinary slot waveguide to roughly 4500 $W^{-1}m^{-1}$ for a slot with a silica layer with 150 nm thickness. We note that the contribution of the electrostriction and radiation pressure in the total gain is similar to the slot waveguide with no top layer; By increasing the gap width, the overlap integral is reduced which causes decrease in the BSBS gain. In addition, the increasing rate of the gain becomes small as the layer thickness increases. Figure Fig. 4.9(b) shows the gain variation in the slot with cover thickness in the slot with $a = 250$ nm, $b = 190$ nm and $c = 160$ nm.

4.5 Impact of optical losses

Several types of linear and nonlinear optical losses are important in semiconductor-based waveguides. Linear loss originates mainly from waveguide surface rough-

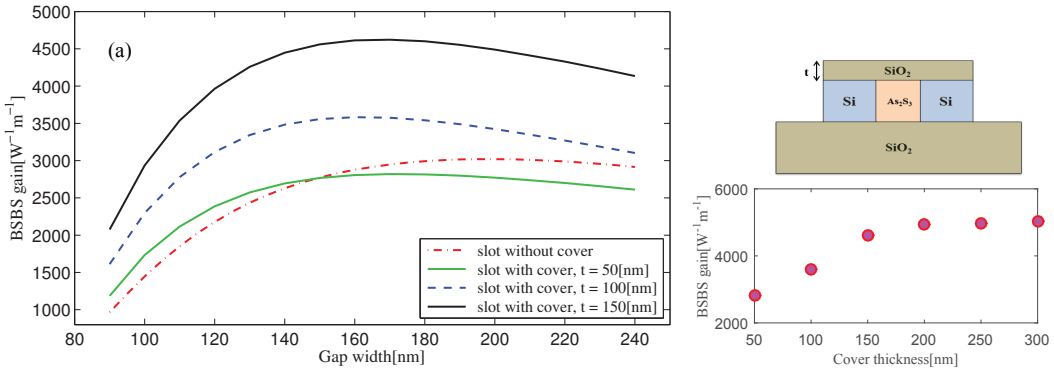

(a) (b)

Figure 4.9 : (a) Comparison of the BSBS gain for silica cover layers with thicknesses 0 nm, 50 nm, 100 nm and 150 nm in a slot waveguide with $a = 250$ nm and $b = 190$ nm. The sketch of the geometry is shown on the right side. (b) Variation of BSBS gain in a slot with the gap width of $c = 160$ nm and similar silicon beam dimensions as in (a).

ness (in bulky waveguides, intrinsic loss constitutes the linear loss term). In waveguides composed of materials with strong odd order optical susceptibilities — such as silicon — multi-photon absorption mechanisms including two photon absorption (TPA) affect SBS interactions [48]. TPA also creates free carriers if the photon's energy exceeds half the material band gap [88] thereby TPA-induced free carrier absorption (FCA) can contribute significantly to the overall optical loss of the waveguide.

Here, we discuss the effect of linear and nonlinear losses on SBS. By applying the small signal approximation, i.e assuming that $P_p(z) \gg P_s(z)$ throughout the waveguide those terms containing higher orders Stokes power as well as the terms with negligible coefficients can be ignored from Eqs. (4.3) and (4.4) [48, 96]. As a result, the coupled equations for a BSBS process with intramode coupling in the presence of linear, TPA and FCA losses are simplified to

$$\frac{\partial P_p}{\partial z} = -(\alpha + \beta P_p + \gamma P_p^2)P_p, \tag{4.14}$$

$$\frac{\partial P_s}{\partial z} = \alpha P_s + (-\Gamma + 2\beta)P_p P_s + \gamma P_p^2 P_s, \tag{4.15}$$

According to Eq. (4.15) to achieve Stokes amplification the following condition must

be satisfied

$$\gamma P_p^2 + (-\Gamma + 2\beta)P_p + \alpha < 0. \tag{4.16}$$

This inequality, specifies upper and lower limits for pump powers leading to Stokes amplifications

$$p_p^{\min} = \frac{-(-\Gamma + 2\beta) - \sqrt{(-\Gamma + 2\beta)^2 - 4\gamma\alpha}}{2\gamma}, \tag{4.17}$$

$$p_p^{\max} = \frac{-(-\Gamma + 2\beta) + \sqrt{(-\Gamma + 2\beta)^2 - 4\gamma\alpha}}{2\gamma}, \tag{4.18}$$

Since the pump power is a real valued quantity, $(\Gamma - 2\beta > 2\sqrt{\alpha\gamma})$ is a necessary requirement for Stokes amplification. This condition has been used previously for defining the figure of merit for SBS [96]:

$$\mathcal{F} = \frac{\Gamma - 2\beta}{2\sqrt{\alpha\gamma}}. \tag{4.19}$$

From Eq. (4.18) one can also see that as long as $p_p^{\min} < P_p < p_p^{\max}$, the Stokes wave is amplified. Since the pump amplitude decreases along the waveguide length, the optimum value for the initial pump power is

$$P_{opt} = p_p^{\max} = \sqrt{\frac{\alpha}{\gamma}} \left(\mathcal{F} + \sqrt{\mathcal{F}^2 - 1} \right). \tag{4.20}$$

Optical losses give us criteria to find the optimum waveguide length. If $\beta \ll 2\sqrt{\alpha\gamma}$ then the optimal length of the structure can be obtained by

$$\mathrm{L_{opt}} = \frac{1}{2\alpha} \ln \left(\frac{p_p^{\max}}{p_p^{\min}} \right) = \frac{1}{2\alpha} \ln \left(\frac{\mathcal{F} + \sqrt{\mathcal{F}^2 - 1}}{\mathcal{F} - \sqrt{\mathcal{F}^2 - 1}} \right),$$

where the derivation of Eq. (4.21) is provided in the Appendix.

4.5.1 Computation of nonlinear losses in slot waveguides

We now examine the impact of nonlinear optical losses on the Stokes amplification in hybrid slot waveguides. Since loss causes reduction in the Stokes signal, only slot configurations with large SBS gains maintain Stokes amplification. We study two geometries: An ordinary slot waveguide and a slot with a silica cover with thickness of $t = 150\,\mathrm{nm}$. In both waveguides, we choose Si beams with square cross section ($a = b = 220\,\mathrm{nm}$). We assume the linear loss to take the values $\alpha = 2.3\ \mathrm{m^{-1}}$ ($\approx 0.1\ \mathrm{dBcm^{-1}}$) and $\alpha = 11.5\ \mathrm{m^{-1}}$ ($\approx 0.5\ \mathrm{dBcm^{-1}}$). We computed

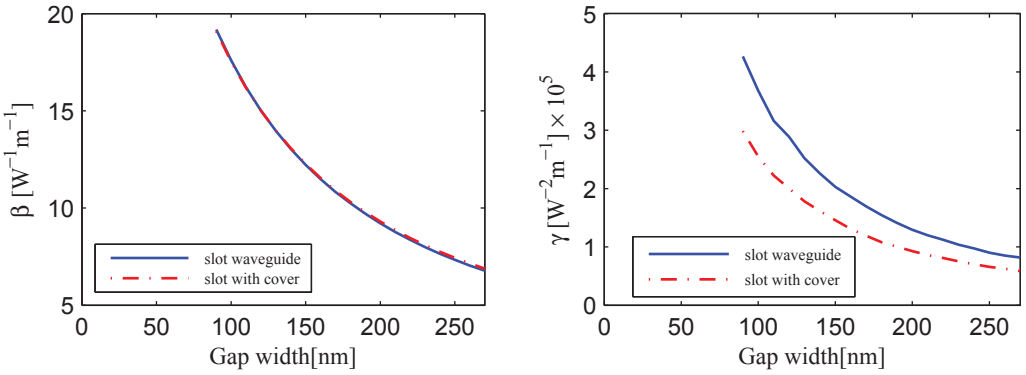

(a) (b)

Figure 4.10 : Nonlinear loss coefficients β and γ for two slot waveguides as a function of the gap size. The red curves in (a) and (b) shows the loss coefficients for slot with $a = 220\,\text{nm}$ and $b = 220\,\text{nm}$, the blue curve shows the same for a waveguide with a silica cover with 150nm thickness.

the loss coefficients β and γ for both structures and plot them in Fig. 4.10. The figure shows that slots with larger gap widths are better candidates since the loss absorption coefficients decrease in both structures.

To obtain Stokes amplification the power growth due to SBS gain must compensate the power reduction caused by optical loss. The figure of merit Eq. (4.19) for the two designs is plotted for the two waveguides in Fig. 4.10. Fig. 4.11 illustrates that although both structures produce fairly large amounts of SBS gain, the optical losses prevent Stokes amplification for a range of gap widths. We have seen in Section 4.5 that a net stokes amplification is only possible for $\mathcal{F} > 1$; greater values of $\mathcal{F}$ lead to stronger Stokes amplifications. According to Fig. 4.11(a) Stokes is not amplified in the slot waveguide with gap widths smaller than 170 nm if $\alpha = 11.5\ \text{m}^{-1}$. It is noteworthy that the figure of merit is dominated by loss coefficients rather than the SBS gain. Although the SBS gain decreases for both waveguides at larger gap widths, this is overcompensated by an even faster decrease in β and γ. Finally we study the maximally realizable Stokes amplification. By solving Eq. (4.15) numerically [48] or analytically the Stokes amplification can be computed

$$\mathcal{A}(L, Ps(0)) = 10\log_{10}(Ps(0)/Ps(L)), \tag{4.21}$$

where L is the waveguide length. It should be noted that this amplification was found within a small signal approximation. This indicates that the amplified Stokes

power should not exceed range of applicability of small signal approximation shown in Ref. [48]. For $Ps(z) \leqq 10^{-4} P_p(z)$ throughout the waveguide, initial Stokes levels above

$$P_s(L) = P_{opt} \times 10^{-(4+0.1A)}, \tag{4.22}$$

can be expected to lead to amplification saturation. Stokes amplification for both covered and non-covered structures are depicted in Fig. 4.11(b). These results indicate that Stokes amplification in the slot structure can be considerably enhanced by using larger gap widths.

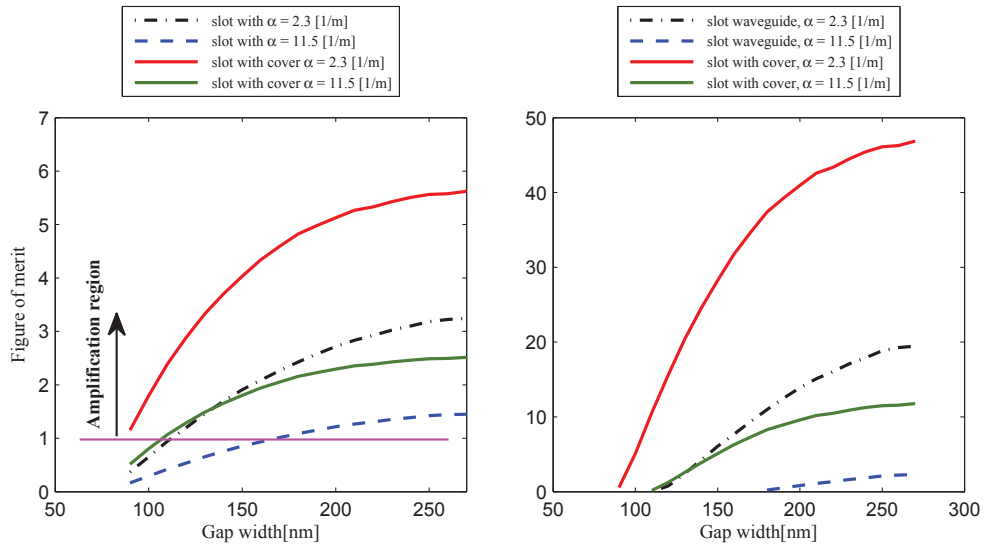

(a) (b)

Figure 4.11 : (a) The Figure of merit for four slot waveguides, including two slots and two slots with silica cover ($t = 150\,\text{nm}$). The silicon beams have fixed dimensions for all the structures ($a = 220\,\text{nm}$ and $b = 220\,\text{nm}$). The linear loss of $\alpha = 2.3\ \text{m}^{-1}$ and $\alpha = 11.5\ \text{m}^{-1}$ are considered in finding the figures of merit. (b) The Stokes amplification corresponding to the waveguides described in (a). The waveguides have optimum lengths.

4.6 Conclusion

We investigated theoretically and numerically silicon chalcogenide slot waveguides for enhancing stimulated Brillouin scattering. We selected this multimaterial structure because of its capacity to highly confine both optical and acoustic modes.

We showed that these features in a silicon-chalcogenide slot waveguide leads to levels of SBS gain that are promising for on-chip SBS applications. To investigate this we studied how the acoustic fields, as well as the optical forces contribute to the overall SBS gain. We found that the radiation pressure contribution to the overall gain switches from destructive to constructive as the gap size is increased with a cross-over point around $c = 100\,\mathrm{nm}$. Slot waveguides with silica cover were introduced to further improve the SBS gain. Finally, we studied the impact of optical loss in the structure that is used in determining the Stokes amplification and we showed that by increasing the gap size, we achieve considerable improvement in the Stokes amplification.

In our work, the acoustic Q-factor was assumed to be constant at 1000. This is a reasonable value which has been reported for silicon nanowires. Although in practice one might find different value for this quantity, this changes the value of SBS gain however, the overall variation of the gain with respect to the cross-sectional dimensions- remains unchanged. We also mentioned that in the presence of nonlinear loss, the Stokes amplification is only achievable if the SBS figure of merit becomes grater than one. Moreover, the impact of nonlinear loss applied strict limitations on the input pump power and the total length which considering them ensures obtaining maximum Stokes amplifications. Although these limits had been numerically demonstrated in [96], we here derived their exact analytic expressions.

4.7 Appendix: The derivation of the optimum waveguide length

In the following we derive the optimum waveguide length presented in Eq. (4.21) by the coupled equations of Eqs. (4.3) and (4.4). The solution of (4.3) takes the following form

$$\frac{1}{2}\ln\left(\frac{{P_p}^2}{\alpha_p+\beta P_p+\gamma {P_p}^2}\right)-\frac{\beta}{\sqrt{4\alpha\gamma-\beta^2}}\tan^{-1}\left(\frac{2\gamma P_p+\beta}{\sqrt{4\alpha\gamma-\beta^2}}\right)=-\alpha z+\mathrm{k}_1. \quad (4.23)$$

By assuming that $\beta \ll 2\sqrt{\alpha\gamma}$, the second term in the left hand side of Eq. (4.23) becomes negligible. Therefore, the equation takes the form

$$\frac{{P_p}^2}{\alpha+\beta P_p+\gamma {P_p}^2}=\mathrm{k}_2\mathrm{e}^{-2\alpha z}, \quad (4.24)$$

where k_1 and k_2 are constants and are decided by the initial boundary conditions. The pump power varies from $p_p^{\max}$ at the beginning of the waveguide, to $p_p^{\min}$ at the end of the waveguide.

$$\frac{(p_p^{\max})^2}{\alpha+\beta p_p^{\max}+\gamma(p_p^{\max})^2}=\mathrm{k}_2, \quad (4.25)$$

$$\frac{(p_p^{\min})^2}{\alpha+\beta p_p^{\min}+\gamma(p_p^{\min})^2}=\mathrm{k}_2\mathrm{e}^{-2\alpha \mathrm{L}_{\mathrm{opt}}}. \quad (4.26)$$

Since $p_p^{\min}$ and $p_p^{\max}$ are roots of the Eq. (4.16), then we can simplify Eqs. (4.26) and (4.25) to take the form

$$\frac{(p_p^{\max})^2}{-(\Gamma+\beta)p_p^{\max}}=\mathrm{k}_2, \quad (4.27)$$

$$\frac{(p_p^{\min})^2}{-(\Gamma+\beta)p_p^{\min}}=\mathrm{k}_2\mathrm{e}^{-2\alpha \mathrm{L}_{\mathrm{opt}}}. \quad (4.28)$$

Finally by dividing Eq. (4.28) to Eq. (4.27) we have

$$\mathrm{L}_{\mathrm{opt}}=\frac{1}{2\alpha}\ln\left(\frac{p_p^{\max}}{p_p^{\min}}\right).$$

Chapter 5

SBS amplifiers in integrated ring resonators

This Chapter is based on the following paper:

Sayyed Reza Mirnaziry, Christian Wolff, MJ Steel, Benjamin J Eggleton, and Christopher G Poulton. Stimulated Brillouin scattering in integrated ring resonators. *JOSA B*, 34(5):937–949, 2017.

Chapter 6

SBS lasing in ring resonators

This Chapter is based on the following paper:
Sayyed Reza Mirnaziry, Christian Wolff, Blair Morrison, MJ Steel, Benjamin J Eggleton, and Christopher G Poulton. Lasing in ring resonators by Stimulated Brillouin scattering in the presence of nonlinear loss. Submitted to *Optics Express*.

In this Chapter we concentrate on employing ring resonators as stimulated Brillouin scattering lasers rather than amplifiers — discussed in the previous Chapter.

6.1 Introduction

Of particular interest is the use of SBS in integrated platforms, which give significant advantages in terms of stability and device size [2]. Although the SBS gain can be significantly enhanced in nanowire waveguides [10], achieving useful levels of Stokes amplification still requires relatively high pump powers and waveguide lengths on the order of centimeters [46, 57]. One way of circumventing these limitations is to use high quality-factor integrated ring resonators, where the build-up of power in on-resonance pump and Stokes waves can dramatically improve input power requirements. Ring resonators are commonly employed to enhance nonlinear effects in a range of photonics applications [110, 111, 112], and recent experiments have demonstrated SBS in hybrid silicon-chalcogenide racetrack structures [50] and Whispering Gallery Mode (WGM) resonators [113]. The combination of a high-Q cavity and gain also opens up the possibility of SBS lasing, which is essential for many of the proposed SBS-based applications [114, 115]; SBS lasing has thus far been demonstrated in fibre ring structures[51, 62], and integrated ring resonators have recently been proposed both for SBS-based amplification [49, 116] and for lasing [8, 117].

Despite these recent studies, a quantitative picture of the physics of SBS lasing in integrated ring resonators, including such important effects as nonlinear losses, does not yet exist in the literature. Although several papers give expressions for the lasing threshold for the closely-related case of Raman scattering (see for example [118, 119])

and these expressions have been used (though without a formal derivation) in SBS lasing experiments [50], it is not known in which situations these formulas can be correctly applied, and a full derivation of the lasing threshold for SBS in integrated ring structures is currently lacking. As a result it is sometimes not clear as to exactly when lasing occurs for SBS, as distinct from regimes where the Stokes signal is strongly amplified. This distinction is particularly problematic in semiconductor platforms, in which nonlinear losses, in particular Free-Carrier Absorption (FCA), can significantly affect the physics of the SBS interaction and will strongly affect the achievable SBS gain [48]. In the case of straight waveguides, nonlinear losses lead to the existence of an optimal waveguide length for SBS gain, as well as a maximum amplification of the Stokes signal; it is not immediately clear how these effects carry over to ring resonators, and how these losses affect the transition from SBS amplification to SBS lasing.

Here we theoretically and numerically investigate SBS lasing in ring resonators in the presence of linear and nonlinear optical loss. This analysis provides a better understanding of the lasing mechanism in rings with materials such as silicon or germanium in which higher order optical losses are non-negligible. We adopt the formalism outlined in [49, 116], in which techniques were given for the computation of SBS in the amplification regime. Building on that work, we here study the different regimes of operation of the ring while focussing on the transition between amplification and lasing, and compute the threshold powers for this transition in the presence of nonlinear losses. We derive analytic expressions for the lasing threshold and investigate the effect of nonlinear losses. This derivation follows that of [120], in which the threshold is derived without noise initiation of the Stokes. While the derivation of the lasing threshold follows from a small-signal approximation, we also provide and analyse a full model including the large signal terms, and compute the Stokes amplification and the Stokes output power for realistic ring resonator parameters. These results can therefore be used for resonator design and for comparison with experimental results. We also discuss the physics of SBS lasing in rings: in rings with nonlinear loss we show that there exists a finite power interval over which lasing occurs; we compute this interval and provide design parameters that can be used for SBS-based ring resonator structures. Our study is in particular useful for realizing SBS lasing in chip scale devices. It provides sufficient information about optimum cavity inputs/outputs as well as the required physical parameters, optical and acoustic properties in a ring configuration to be used in designing integrated

racetrack resonators for SBS lasing.

6.2 Geometry and numerical computations

Following [49, 116], we consider the geometry of a ring resonator sketched in Fig. 6.1. A ring of length L is coupled to a single straight waveguide via a coupling region; for the sake of simplicity we assume that the SBS gain occurs only in the ring section and not in the coupler. Here we consider the backward SBS process, in which input pump $P_{\mathrm{p}}^{\mathrm{in}}$ and Stokes $P_{\mathrm{s}}^{\mathrm{in}}$ contra-propagate; the forward SBS process can be handled using the same formalism, appropriately modified to account for the different propagation direction. This modification however, does not lead to a change in the magnitude of resultant threshold powers or in output Stokes demonstrated in this paper, assuming identical gain, loss coefficients, coupling and physical properties (i.e. ring length) in the Forward SBS process to those of backward SBS.

Throughout this investigation we are assuming that the pump and the Stokes are aligned to two cavity modes, and that the free-spectral-range (FSR) of the ring is equal to an integer multiple of the Brillouin shift. Resonant coupling Brillouin lasers are in particular efficient — in terms of the required pump power to achieve lasing — for chip scale ring resonators in which pump and Stokes frequencies are designed to lie on close resonances of the cavity. In practice nonlinear dispersion (Kerr, free-carrier dispersion, and frequency pulling due the phase shift arising from the SBS process itself) as well as thermal effects can result in a change in the FSR of the cavity, however for typical power levels (as discussed in [13, 116]) such changes are far smaller than the SBS linewidth and can be neglected. The absolute values of the cavity mode frequencies are however expected to shift markedly. We therefore assume that active stabilisation of the pump is used to track the frequency of the cavity mode; the shift of the Stokes frequency will then automatically continue to lie on-resonance. Note that this implicitly assumes that the variation in pump power is slow enough to accommodate thermal effects; throughout this paper we therefore operate in the quasi-CW regime, in which it is assumed that the pulse lengths are much longer than the phonon lifetime — in most platforms this is on the order of 10 ns. A study of full dynamic response, including the stability, of these devices we leave to future investigations.

The powers in the pump and Stokes within the ring are then governed by the equations [48](See Section 3.11)

$$\frac{dP_{\rm p}}{dz} = -(\alpha + \beta P_{\rm p} + \gamma P_{\rm p}^2)P_{\rm p} - (2\beta + 4\gamma P_{\rm p} + \gamma P_{\rm s} + \Gamma)P_{\rm p}P_{\rm s}, \quad (6.1)$$

$$\frac{dP_{\rm s}}{dz} = (\alpha + \beta P_{\rm s} + \gamma P_{\rm s}^2)P_{\rm s} + (2\beta + 4\gamma P_{\rm s} + \gamma P_{\rm p} - \Gamma)P_{\rm p}P_{\rm s}, \quad (6.2)$$

where $P_{\rm p}$ and $P_{\rm s}$ are the circulating pump and Stokes powers, respectively; α, β and γ are the linear, TPA and FCA-induced loss coefficients respectively, and Γ is the SBS gain expressed in units of $\mathrm{W^{-1}m^{-1}}$. We also note that pump and Stokes powers take positive values in our model, as opposed to the formalism where counter-propagating waves have negative powers [48]. We have assumed here also that both pump and Stokes are in the same optical mode, and so the nonlinear coefficients are identical in both equations; this is realistic given the close spectral spacing of pump and Stokes for the SBS interaction, but could be generalized at the expense of complicating the formulation. Furthermore, in Eqs. (6.1) and (6.2) we have not considered noise, as arising from spontaneous emission or from thermal phonons. As a result, this model does not allow noise-related predictions, such as the linewidth in the lasing regime. The focus of this work is to study the dependence of the lasing threshold on the various system parameters including coupling, nonlinear loss and pump power. A corresponding study of the noise properties, beginning from the coupled amplitude equations, is beyond the scope of this current work.

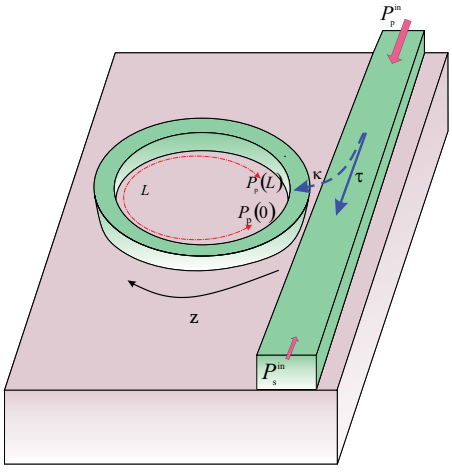

Figure 6.1 : Schematic of a ring resonator in vicinity of a straight coupler.

On resonance, the values of the pump power at the beginning ($z = 0$) and at the

end ($z = L$) of the ring segment are related to the input pump power by [49, 116]

$$P_{\mathrm{p}}^{\mathrm{in}} = \frac{1}{|\kappa|^2}\left(\sqrt{P_{\mathrm{p}}(0)} - |\tau|\sqrt{P_{\mathrm{p}}(L)}\right)^2, \tag{6.3}$$

where κ and τ are the complex envelope coupling coefficients as depicted in Fig. 6.1, related by $|\tau|^2 + |\kappa|^2 = 1$ [121, 120]. Similarly, the values of the Stokes are related via the coupling region by

$$P_{\mathrm{s}}^{\mathrm{in}} = \frac{1}{|\kappa|^2}\left(\sqrt{P_{\mathrm{s}}(L)} - |\tau|\sqrt{P_{\mathrm{s}}(0)}\right)^2. \tag{6.4}$$

In writing equations Eqs. (6.3) and (6.4) we have implicitly assumed the coupling coefficients κ and τ are the same for both pump and Stokes and do not change with frequency over very small (GHz) ranges studied here. The system of equations (6.1-6.4) encapsulates the physics of the ring operation: the input pump is transferred to the ring at $z = 0$, experiences both linear and nonlinear loss as well as loss to the other mode, and then is partially transferred to the output. The Stokes on the other hand is input at $z = L$ and experiences gain with decreasing z, as well as linear and nonlinear loss.

Figure 6.2 shows the output Stokes power resulting from the numerical solution of Eq. (6.1)-(6.4), for a ring resonator with (a) linear losses only, and (b) with both linear and nonlinear losses. To solve these equations we apply the numerical approach presented in [49, 116] in which pump and Stokes are computed using an iterative shooting technique, by which the differential equations are solved at each step of the iteration using a Runge-Kutta method, and the mismatch in the boundary conditions becomes a measure of the closeness to the true solution. In Fig. 6.2(a) the output Stokes is computed for a ring with $\Gamma = 500$ W^{-1}m^{-1} keeping the coupling constant fixed at $\kappa = 0.31$ and changing the values of αL in order to highlight the impact of the linear loss. A clear threshold pump power can be seen, denoted by a sharp increase in Stokes power; the value of this threshold increases with the linear loss. The effect of nonlinear losses can be seen in the example shown in Fig. 6.2(b). Here we have assumed that $\alpha L = 0.2$; $\gamma = 1.8 \times 10^5$ W^{-2}m^{-1}, $L = 10.879$ mm, $\Gamma = 4000$ W^{-1}m^{-1}, which are close to experimentally-realisable values for a silicon nanophotonic waveguide, and we have neglected TPA ($\beta = 0$ W^{-1}m^{-1}), which has a negligible direct effect on SBS in silicon. The Stokes power is depicted as a function of input pump power for different values of the ratio between input pump and Stokes, denoted by $R = P_{\mathrm{s}}^{\mathrm{in}}/P_{\mathrm{p}}^{\mathrm{in}}$. In order to have an idea for the order of magnitude of R

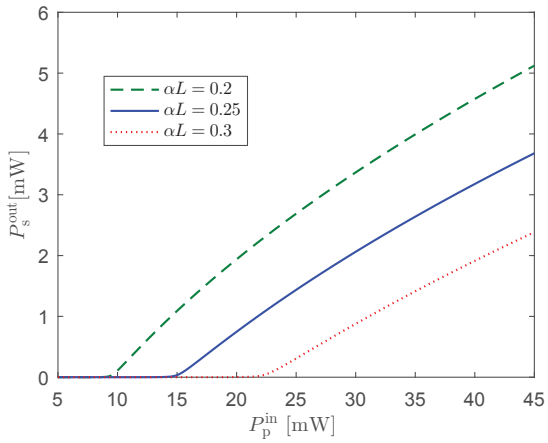

(a)

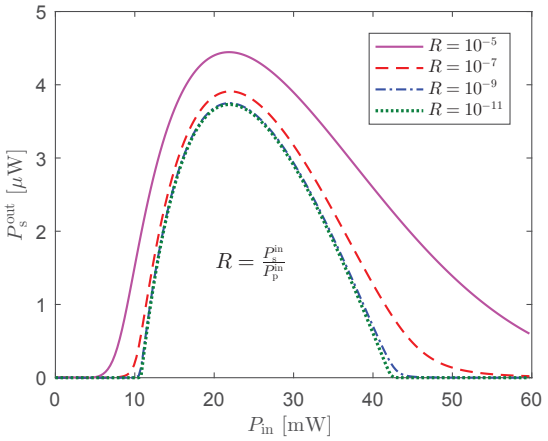

(b)

Figure 6.2 : Output Stokes power as a function of input pump power at the lasing region and resonant condition in the presence of (a) linear losses and (b) both linear and nonlinear losses. In (a) $\Gamma = 500$ W^{-1}m^{-1}, $R = 10^{-11}$ and $\kappa = 0.31$. In (b) $\alpha L = 0.2$; $\gamma = 1.8\times10^{5}$ W^{-2}m^{-1}, $\beta = 10$ W^{-1}m^{-1}, $\kappa = 0.16$ and $\Gamma = 4000$ W^{-1}m^{-1}. The length $L = 10.879$ mm corresponds a ring resonator with free spectral range equal to a Brillouin frequency shift of 10 GHz.

in the lasing regime, we can assume that only a single Stokes photon is initializing the lasing. Then

$$R = \frac{P_{\rm s}^{\rm in}}{P_{\rm p}^{\rm in}} = v_{\rm g}\frac{hf_{\rm s}}{P_{\rm p}^{\rm in}}, \tag{6.5}$$

where $v_{\rm g}$ is the optical group velocity and $hf_{\rm s}$ is the Stokes photon energy (h Plank's constant and $f_{\rm s}$ Stokes frequency). As in the linear case (Fig. 6.2(b)), the Stokes increases rapidly with the input pump beyond threshold. This trend however is reversed after the Stokes power rises to a maximum value; thereafter, the Stokes power decreases as nonlinear losses begin to dominate. For smaller power ratios R, the Stokes falls abruptly to negligible values once a second, higher threshold is crossed. For higher power ratios, we see that there is no distinct threshold, instead we find that with increasing pump power the amplification of the Stokes signal decreases steadily.

Both thresholds are associated with transitions between lasing and amplification regimes. In the amplification regime the output Stokes is proportional to the input Stokes signal, with gain arising from SBS-induced transfer of energy from the pump. In the lasing regime an infinitely small Stokes signal can generate a finite Stokes output — in a real device, this input Stokes would arise from quantum fluctuations. In this situation the Stokes signal is necessarily far smaller than the pump, and so it is useful to consider the Small Signal Approximation (SSA); under this approximation Eqs. (6.1) and (6.2) take the simpler form of [48]

$$\frac{dP_{\rm p}(z)}{dz} = -\Big(\alpha + \beta P_{\rm p}(z) + \gamma P_{\rm p}^2(z)\Big)P_{\rm p}(z), \tag{6.6}$$

$$\frac{dP_{\rm s}(z)}{dz} = \Big(\alpha + \gamma P_{\rm p}^2(z) - (\Gamma - 2\beta)P_{\rm p}(z)\Big)P_{\rm s}(z). \tag{6.7}$$

The lasing threshold corresponds to input pump powers for which the Stokes output, when computed using the SSA, tends to infinity. This divergence means that the final value of the Stokes signal, as arising from the full equations (6.1) and (6.2), cannot in principle depend on the strength of an initial small signal.

6.3 Thresholds for rings with linear loss only

We can gain insight into the values at which the thresholds occur by considering the loss and gain mechanisms that act on the Stokes signal within the ring. There

are different regimes of behaviour, depending on the value of the round-trip envelope gain G of the Stokes, defined as

$$G = \sqrt{\frac{P_s(0)}{P_s(L)}}\,. \tag{6.8}$$

The different modes of operation are reflected in the overall change of the Stokes signal as it passes through the entire device. The net Stokes amplification through the bus, defined as the ratio of output Stokes power from the bus to the input Stokes power, can be expressed as a function of G by[49, 116]:

$$\mathcal{A} := \frac{P_{\rm s}^{\rm out}}{P_{\rm s}^{\rm in}} = \left|\frac{|\tau| - G}{1 - |\tau|G}\right|^2, \tag{6.9}$$

For a ring with linear losses we find three different regimes of operation, depending on the value of G in the SSA. Figure 6.3(a) shows these regimes schematically as a function of input pump power. For $G < 1$, the output Stokes is attenuated ($\mathcal{A} < 1$) because the power conversion from SBS is still too weak to achieve any Stokes enhancement. For values $1 < G < 1/|\tau|$, the SBS gain mechanism is strong enough to compensate the optical losses in the cavity, but is not strong enough for lasing to occur. This is the amplification region, in which the output Stokes from the ring will be proportional to the input Stokes, with amplification factor $\mathcal{A} > 1$ taking a finite value greater than 1. The amplification region has been explored in detail in [49, 116]. As G approaches $1/|\tau|$ the net Stokes amplification tends towards infinity, so that a finite Stokes value is attained even for a vanishingly small input Stokes signal. The input pump power for which this occurs is the lasing threshold. If we include the impact of pump depletion (thereby abandoning the SSA) by solving Eqs. (6.1) and (6.2), we find that G remains below $1/|\tau|$ for all pump powers, and therefore from Eq. (6.9) the Stokes amplification saturates (as shown by the solid line in Fig. 6.3(a)). However to compute the lasing threshold the SSA is sufficient: a general expression for G in the case of the SSA can be obtained by writing Eq. (6.7) as $\frac{dP_{\rm s}}{dz} = -g(z)P_{\rm s}$, where $g(z) = \big(\alpha + \gamma P_{\rm p}^2(z) - (\Gamma - 2\beta)P_{\rm p}(z)\big)$, so that

$$G = \exp\left[\frac{1}{2}\int_0^L g(z)dz\right]. \tag{6.10}$$

Combining Eq. (6.9) and Eq. (6.10), the most general condition for the lasing threshold is then

$$|\tau| \exp\left[\frac{1}{2}\int_0^L g(z)dz\right] = 1. \tag{6.11}$$

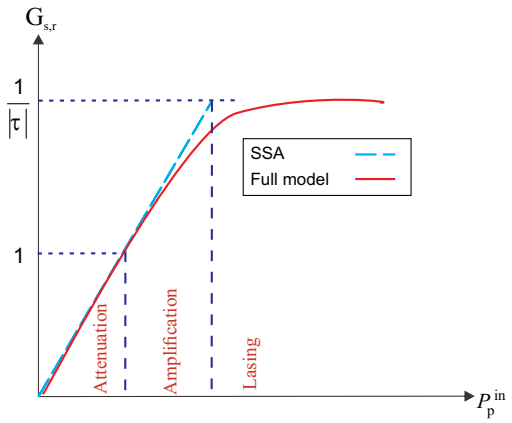

(a)

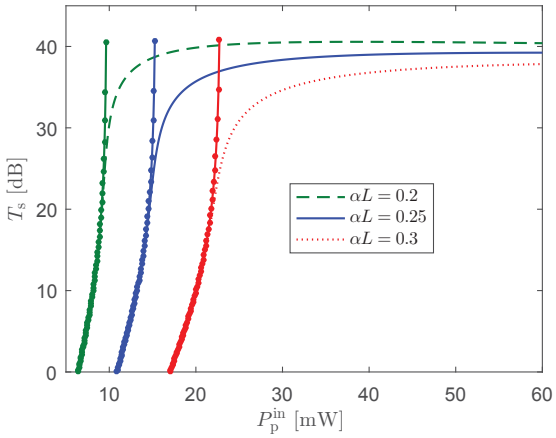

(b)

Figure 6.3 : (a) Schematic variation of the round-trip gain in a ring resonator with linear loss within the SSA and full model. (b) The corresponding Stokes total amplification of a ring resonator with the parameters described in Fig. 6.2(a). The solid circle lines show $\mathcal{A}$ for the small signal model.

Figure 6.3(b) compares the Stokes amplification $\mathcal{A}$ predicted by the full model to the amplification computed with the SSA using the parameters illustrated in Fig. 6.2(a). From the figure it can be seen that the lasing threshold is a monotonic function of the linear loss and shifts to larger pump powers as αL increases and more power is required to compensate the loss. The maximum amplification however does not significantly vary with loss and is mainly a function of coupling coefficients and the power ratio R[49, 116].

An analytic expression for the small signal G can be derived in the linear case; by solving Eq. (6.6) for $\beta = 0$ and $\gamma = 0$, then substituting into Eq. (6.7) [49, 116], we find that:

$$G = \exp\big[-\frac{\alpha L}{2} + \frac{\Gamma}{2\alpha} P_{\mathrm{p}}(0)(1 - e^{-\alpha L})\big]. \tag{6.12}$$

Now by substituting G into Eq. (6.11) and using Eq. (6.3), the lasing threshold is given by

$$P_{\mathrm{p}}^{\mathrm{in,th}} = \frac{\big(\alpha L - 2\ln|\tau|\big)}{(1 - e^{-\alpha L})} \frac{\alpha}{\Gamma} \frac{(1 - |\tau| e^{(-\alpha L/2)})^2}{|\kappa|^2}, \tag{6.13}$$

Figure 6.4(a) shows the contours of normalized pump power $P_{\mathrm{p}}^{\mathrm{in,th}} \frac{\Gamma}{\alpha}$ as a function of αL and $|\kappa|$. We have assume that αL varies between 0 and 1; the reason for this is that for $L = 1\,\mathrm{cm}$ — which is corresponding to a Brillouin frequency of about 10 GHz in conventional waveguides — then α varies between 0 dBCm^{-1} to $\sim$ 4.35 dBCm^{-1} as a typical range for the linear loss coefficient. While Fig. 6.4(a) takes into account the SBS lasing, we note that very similar contours are also obtained for the required Stokes power to initialize Stokes amplification [49, 116]. From the figure the threshold power increases with αL as additional power is needed to overcome the losses in the ring. Similarly, the threshold power decreases with the SBS gain (because a higher gain will compensate losses at lower power levels), however achieving lasing is feasible at any value of Γ. We also note that, for a given value of αL, the threshold experiences a minimum as a function of the coupling coefficient $|\kappa|$ at the critical coupling point. Below and above this point the ring is under/over-coupled and the total pump power in the ring will be reduced in comparison to the critical point.

In practice, one has to measure the optical loss and coupling parameters of a ring to be able to determine threshold by Eq. (6.13). While there are methods to evaluate these quantities [122], Eq. (6.13) can also be expressed in terms of the

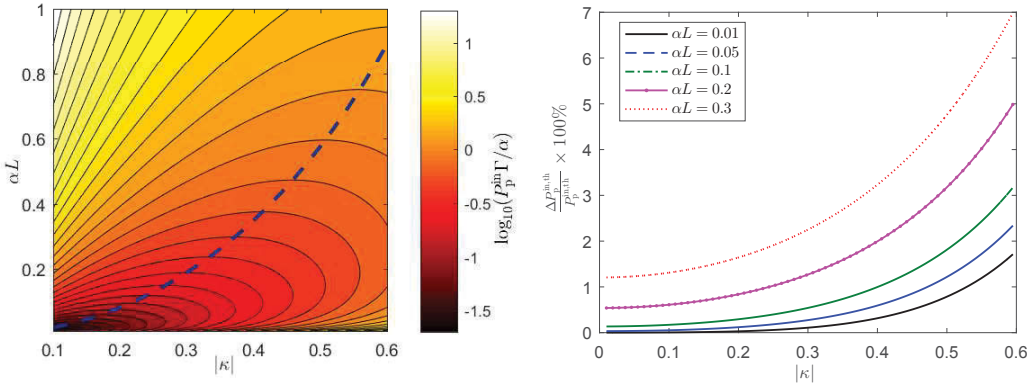

(a) (b)

Figure 6.4 : (a) Contours of the lasing threshold as a function of αL and the coupling coefficient. The dashed line shows the critical coupling. (b) The threshold difference $\Delta P_{\mathrm{p}}^{\mathrm{in,th}}$ between the power obtained by Eq. (6.13) with the threshold estimated from 6.15, plotted for a range of the coupling coefficient $|\kappa|$ and for different values of αL. $\Delta P_{\mathrm{p}}^{\mathrm{in,th}}$ is normalized to the exact theoretical value of the threshold (i.e. Eq. (6.13)) and is plotted in percentage.

optical quality factor[118, 119]. The loaded Q factor of the ring can be calculated via (see the Appendix)

$$Q_L = \frac{\sqrt{2}\pi L n_{\mathrm{eff}}}{2\lambda} \frac{\sqrt{1+|\tau|^2 e^{-\alpha L}}}{1-|\tau| e^{-\frac{\alpha L}{2}}}, \tag{6.14}$$

where n_{eff} is the effective index of the ring. Now assuming $\alpha L \ll 1$ and small $|\kappa|$, Eq. (6.13) simplifies to

$$P_{\mathrm{p}}^{\mathrm{in,th}} = \frac{\pi^2 n_{\mathrm{eff}}^2}{\lambda^2} \frac{L}{\Gamma} Q_{\mathrm{c}} \frac{1}{Q_{\mathrm{L}}^3}, \tag{6.15}$$

where Q_{c} is the Q factor due to the coupling which is given by

$$Q_{\mathrm{c}} = \frac{\sqrt{2}\pi L n_{\mathrm{eff}}}{2\lambda} \frac{\sqrt{1+\tau^2}}{1-\tau}. \tag{6.16}$$

Equation (6.15) has also been derived in [118] for Raman sources: it shows the inverse square dependency of the threshold power to the loaded Q-factor in the case where $Q_{\mathrm{L}} = Q_{\mathrm{c}}$. Figure 6.4(b) shows the difference between the threshold results obtained by Eq. (6.13) and Eq. (6.15) for different values of αL. Here, $\Delta P_{\mathrm{p}}^{\mathrm{in,th}} = P_{\mathrm{p}}^{\mathrm{in,th}}$[Eq. (6.13)] $- \mathrm{P}_{\mathrm{p}}^{\mathrm{in,th}}$[Eq. (6.15)] which is normalized to $P_{\mathrm{p}}^{\mathrm{in,th}}$[Eq. (6.13)]. From the figure, there is a very good agreement between the threshold values for small

values of αL and $|\kappa|$ because Eq. (6.15) is obtained based on these assumptions. $\Delta P_{\mathrm{p}}^{\mathrm{in,th}}$ then grows for larger loss and coupling coefficients.

6.4 Thresholds for rings with both linear and nonlinear losses

We have seen in Section 2 that the round-trip gain G is greatly affected by the degree of optical loss in the ring. Depending on the strength of nonlinear loss relative to the linear loss, three different scenarios can be attained for the round trip gain. These situations are shown schematically in Fig. 6.5(a). The first possibility is that the nonlinear loss is negligible at weak pump powers, leading to a similar threshold to that of the linear case, but dominates as the pump power increases. Within the SSA there are two lasing thresholds (pink dashed lines): the SBS gain mainly compensates the linear loss to reach the lower lasing threshold, while for higher powers the nonlinear loss term γP_{p}^2 grows quadratically with the pump power until it is comparable with α in Eq. (6.7), upon which the second threshold is reached. This leads to a finite lasing interval for the ring; while within the SSA the Stokes power tends to infinity on the edges of this interval (and is not physically meaningful within the interval itself), in the full model G is prevented by the loss terms from reaching the line $1/|\tau|$ and hence the output Stokes power remains finite. This behaviour is shown by numerical calculations of a case study in Fig. 6.5(b), in which the lasing interval is clearly seen as the flat region for the output Stokes signal. The Stokes is shown for different values of R; while this formally represents an input Stokes seed, this can be shown to be equivalent to a distributed initiation via spontaneous emission [123].

In the second scenario, the effect of nonlinear loss grows such that it is comparable with the linear loss at the first threshold, and both effects combine to compensate the gain for a single power (green lines in Fig. 6.5(a)). In this situation lasing will only formally occur for a single input power; beyond this point nonlinear effects will dominate the behaviour. In this situation certain signatures of lasing, such as a linear increase beyond threshold, will not appear — as shown in Fig. 6.5(c) the Stokes power remains flat at the threshold and decreases thereafter.

In the third scenario (Fig. 6.5(a), blue line) the value of the round trip gain is clamped by the nonlinear terms to values below the line $1/|\tau|$. In this case the nonlinear losses dominate to the extent that lasing is entirely forbidden. Amplification of the Stokes signal is still however possible if G takes values larger than unity. This

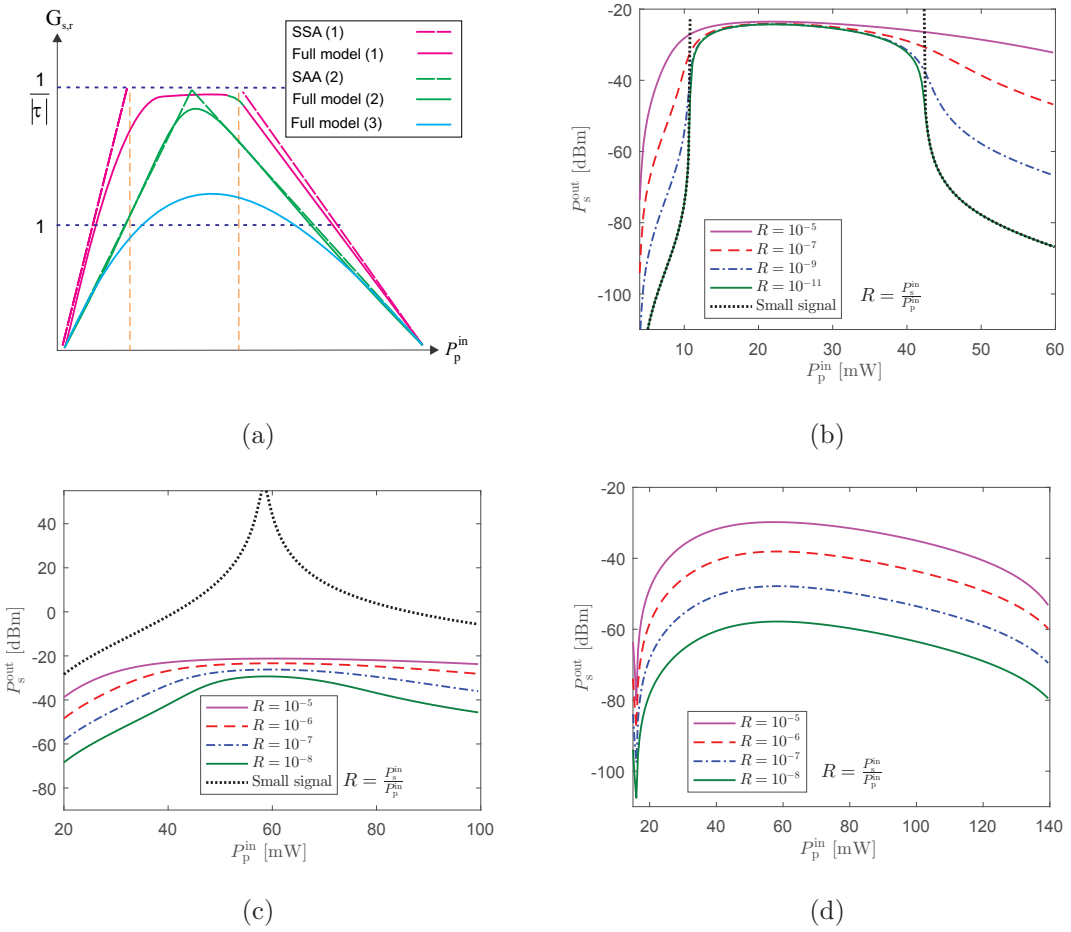

Figure 6.5 : (a) Schematic variation of the round-trip gain in a ring resonator with nonlinear loss in three different operating regimes shown in pink (with two lasing thresholds), green (with single threshold) and blue (no lasing). Dashed lines show the result of the small signal model and the solid lines are expected in the full model. (b) An example of the Stokes output power for a ring with two lasing thresholds. The black dotted lines shows the SSA. The results of the full model are also shown for different values of the power ratio R. for a ring with the SBS gain and loss parameters described in Fig. 6.2(b). (c) The Stokes output power for a ring with parameters which leads to a single lasing threshold. $\Gamma = 5970$ W^{-1}m^{-1}; $|\kappa| = 0.24$; $\alpha = 40.9$ m^{-1} and $\gamma = 1.8 \times 10^5$ W^{-2}m^{-1}. (d) The Stokes output power in a ring with parameters that leads to only Stokes amplification. $\Gamma = 5700$ W^{-1}m^{-1} and the loss and coupling parameters are as in (c).

is shown in Fig. 6.5(d), in which the output Stokes grows in proportion to the input Stokes.

Analytic expressions

We now derive expressions for the round trip gain G, and threshold powers, for the case of rings having both linear and nonlinear losses. As in the linear case, the starting point for threshold calculations is the SSA. In the following we neglect the TPA coefficient β as this loss term is small compared to FCA loss in technologically important semiconductors such as silicon. Following the notation in [49, 116] we define a dimensionless parameter $V = P_{\mathrm{p}}(0)\sqrt{\frac{\gamma}{\alpha}}$ which is a normalised measure of the power in the ring. The governing equation for the pump (6.6) can be solved analytically; the solution is

$$P_{\mathrm{p}}(z) = \sqrt{\frac{\alpha}{\gamma}}\frac{V}{\sqrt{(1+V^2)e^{2\alpha z} - V^2}}. \tag{6.17}$$

Now by substituting into Eq. (6.7), G is given by

$$G = \left(\frac{1}{V^2 + 1 - V^2 e^{-2\alpha L}}\right)^{\frac{1}{4}} \exp\left[-\frac{\alpha L}{2} - \mathcal{F}\arctan\left(\frac{V - V\sqrt{(V^2+1)e^{2\alpha L} - V^2}}{V^2 + \sqrt{(V^2+1)e^{2\alpha L} - V^2}}\right)\right], \tag{6.18}$$

where $\mathcal{F} = \frac{\Gamma}{2\sqrt{\alpha\gamma}}$ is the SBS nonlinear figure of merit[48].

Unlike Eq. (6.12), G is now a complicated function of three parameters V, αL and $\mathcal{F}$. To evaluate the lasing threshold, we substitute Eq. (6.18) into Eq. (6.10) and then use Newton's method to determine the solutions of Eq. (6.11). Figure 6.6 shows the contours of $V^{\min}$ and $V^{\max}$, corresponding to the first and second lasing threshold respectively, as functions of the universal ring parameters αL and κ, for typical SBS Figures of Merit $\mathcal{F} = 1.1$ ((a),(b)) and $\mathcal{F} = 1.5$ ((c),(d)). It can be seen in Figs. 6.6(a) and 6.6(b) that for a constant αL, $V^{\min}$ increases while $V^{\max}$ decreases with the coupling coefficient $|\kappa|$. This can be understood from the interpretation of $V^{\min,\max}$ as measuring the minimum/maximum powers permissible for lasing in the ring: as the coupling increases toward the critical coupling point, the overall power in the ring increases, making it easier to achieve lasing if only linear losses are dominant, but harder if nonlinear losses are significant. As we approach the amplification region $V^{\min}$ and $V^{\max}$ become closer: the lasing power interval

becomes smaller until there only exists a single threshold. The interval is widest in the weakly-coupled regime; this is therefore the most promising configuration for SBS lasing in the presence of nonlinear loss. In addition, comparing the contours of V^{th} at $\mathcal{F} = 1.1$ with the ones in $\mathcal{F} = 1.5$ reveals that SBS lasing can be achieved across wider ranges of αL and $|\kappa|$ for larger values of $\mathcal{F}$. In addition, the lasing power interval in weakly-couled regimes is further expanded.

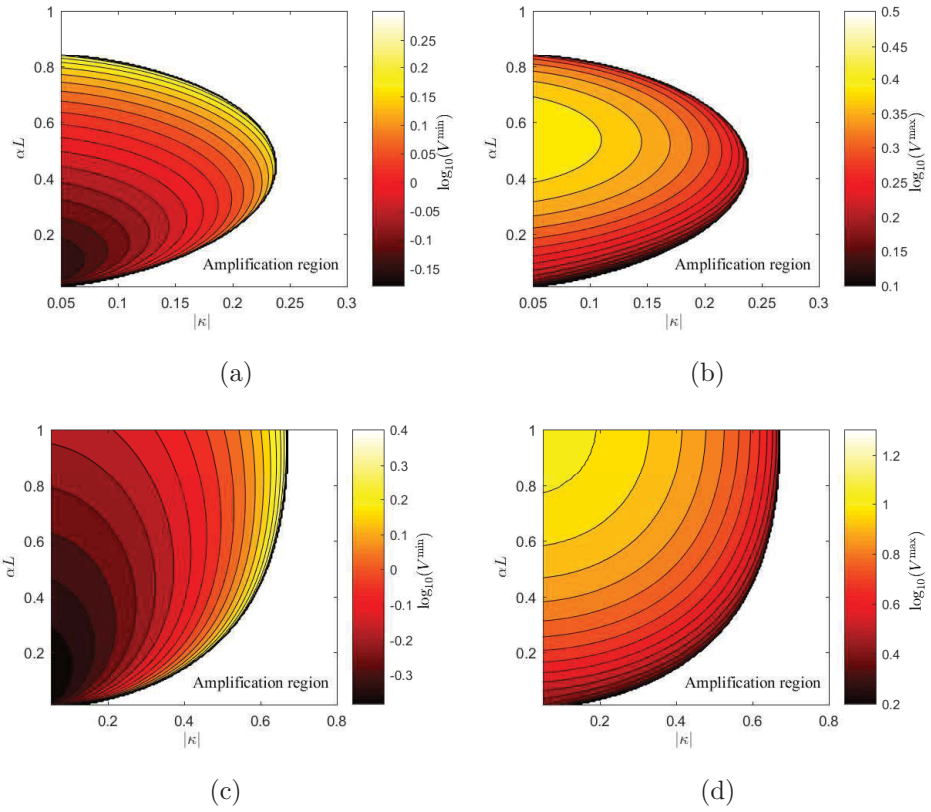

Figure 6.6 : $V^{\min}$ and $V^{\max}$ at the lasing threshold as a function of κ and αL for (a,b) $\mathcal{F} = 1.1$ and (c,d) $\mathcal{F} = 1.5$.

The quantity V^{th}, defined as either $V^{\min}$ or $V^{\max}$ as required, can be used to determine the threshold pump power required for lasing. By substituting Eq. (6.17) into Eq. (6.3), the lasing threshold(s) can be expressed in terms of input pump power

$$P_{\mathrm{p}}^{\mathrm{in,th}} = \sqrt{\frac{\alpha}{\gamma}} \frac{V^{\mathrm{th}}}{\sqrt{|\kappa|}} \left(1 - |\tau| \sqrt[4]{\frac{1}{((V^{\mathrm{th}})^2 + 1)e^{2\alpha L} - (V^{\mathrm{th}})^2}} \right), \tag{6.19}$$

Assuming that the physical parameters of the ring remain fixed and hence the ratio α/γ remains constant, we see that $P_{\mathrm{p}}^{\mathrm{in,th}}$ is approximately proportional to V^{th}. For

a given figure of merit, a low ratio of α/γ leads to a smaller threshold power as well as a smaller threshold interval, as measured in terms of the parameters of the ring. In Fig. 6.7 the lasing thresholds are computed for ring resonators with $\mathcal{F} = 1.1$ (Fig. 6.7(a) and 6.7(b)) and $\mathcal{F} = 1.5$ (Fig. 6.7(c) and 6.7(d)). In these examples we have assumed $\alpha/\gamma = 2 \times 10^{-4}$ W^2. It can be seen that for a given coupling coefficient, as αL increases both upper and lower thresholds shift to higher powers to compensate linear (for lower threshold) and nonlinear (for upper threshold) losses. We also note that although the minimum (maximum) lasing threshold at larger values of $\mathcal{F}$, becomes smaller (larger) in weakly-coupled rings.

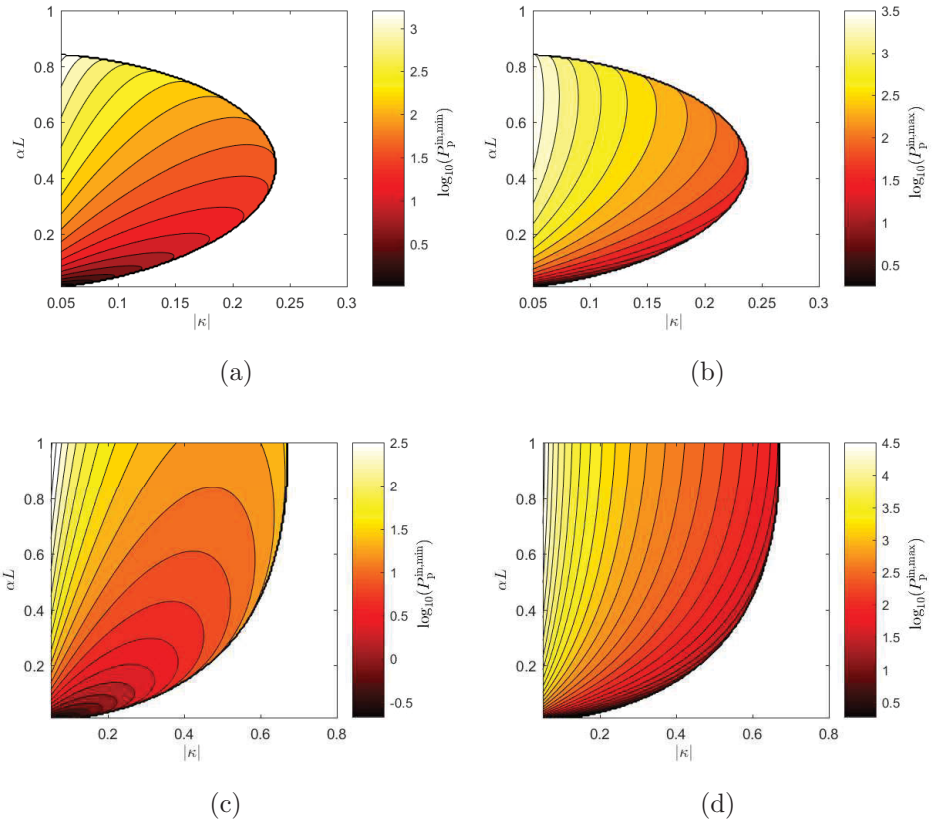

Figure 6.7 : Minimum/Maximum values of the lasing threshold in mW as a function of κ and αL for $\mathcal{F} = 1.1$ (a,b) and $\mathcal{F} = 1.5$ (c,d) for $\frac{\alpha}{\gamma} = 2 \times 10^{-4}$W^2.

For a given coupling coefficient the lasing power interval is larger for larger values of $\mathcal{F}$. This is shown in Fig. 6.8 where $\mathcal{F}$ takes four different values, 1.1, 1.25, 1.5 and 1.75. As the SBS figure of merit becomes smaller, given a constant coupling coefficient $|\kappa|$, both thresholds are increased because additional power is required to compensate the loss. In addition the threshold interval becomes smaller because

the range of powers required to compensate both linear and nonlinear losses in the ring decreases. As the nonlinear loss coefficient γ approaches zero, the SBS figure of merit $\mathcal{F}$ grows without bound and the power required to attain the upper threshold tends to infinity.

While in the case of linear loss, the Stokes output steadily increases with the input pump, in rings with nonlinear loss there exists a maximum attainable Stokes power within the lasing threshold interval. The SSA can be used to estimate the corresponding pump power to the maximum Stokes in the lasing regime. The general approach is that we look for the pump power at which the round-trip gain (6.12) reaches its maximum within the SSA. Within this assumption, the value of G in the lasing threshold interval exceeds $1/|\tau|$, and so does not have a physical meaning (because G will be clamped by the nonlinear losses to values below $1/|\tau|$). However as a first estimate this maximum can be expected to occur at a pump power close to the true maximum value of G, because it is at this power that the overall SBS gain in the ring attains its highest value. Figure 6.9(a) shows the normalized pump power corresponding to the maximum output Stokes in the lasing regime as a function of αL and $\mathcal{F}$. We note that the Stokes output at this pump power is a function of the power ratio R as well as loss and SBS gain coefficients which can be in general evaluated numerically by solving Eqs. (6.1) and (6.2). The white area on left hand side of the contours is the amplification region. Figure 6.9(b) shows the computed value of the maximum Stokes power for a weak input Stokes power. These calculations are performed in the limit that the input Stokes is extremely weak (1 pW in these calculations), and show the maximum output power that can be obtained in the lasing regime, as a consequence of the higher-order loss terms. It can be seen that for a certain αL by increasing $\mathcal{F}$ the output Stokes first starts increasing. Whether a larger figure of merit is obtained by increasing the SBS gain or by reducing the nonlinear loss, this will lead to an increase in the round trip gain G as it shifts toward $1/|\tau|$, thereby enhancing the Stokes output. At larger values of $\mathcal{F}$ however, nonlinear losses — including small and large signal terms in Eqs.(6.1) and (6.2) — prevent further enhancement of G. Thus, the output Stokes does not change although a larger pump power is required to compensate the nonlinear losses (see Fig. 6.9(a)).

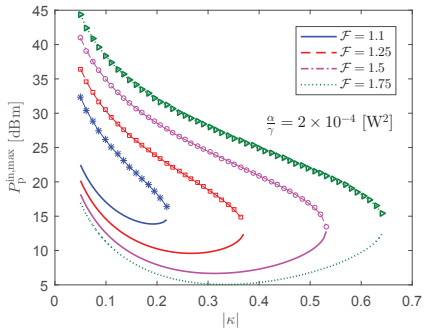

Figure 6.8 : Lasing thresholds as a function of the coupling coefficient for different values of $\mathcal{F}$. αL is assumed to be 0.3 and $\alpha/\gamma = 2 \times 10^{-4}$ W^2.

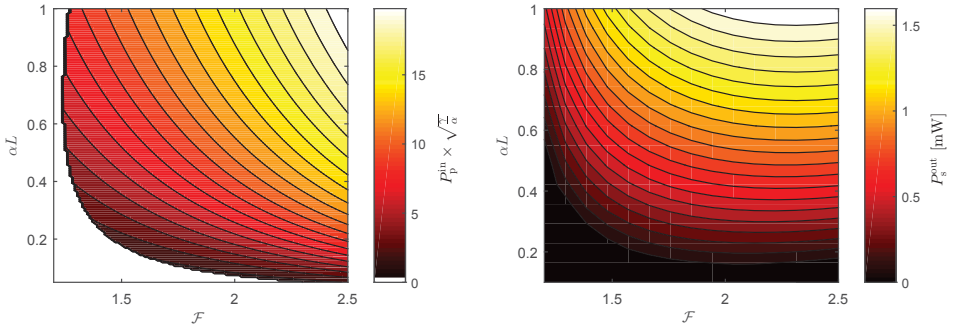

(a) (b)

Figure 6.9 : The normalized input pump power corresponding to the maximum Stokes output in the lasing regime for a range of αL and SBS figure of merit. $|\tau|$ is assumed to be 0.9. (b) The maximum Stokes output in mW. The initial Stokes is assumed to be 1 pW.

6.5 Conclusion

We investigated the SBS lasing in integrated ring resonator at the resonance frequency. We provided numerical and analytic tools to evaluate the lasing threshold in rings with respect to SBS gain, loss and coupling properties. Moreover, useful expressions were derived and examined for the lasing threshold in different situations by assuming both small and large Stokes signal. In the case of nonlinear losses, we showed that three different scenarios are conceivable for the lasing in ring; First there exists a finite lasing power interval at which the output Stokes signal varies merely with the pump power in the small signal model; second lasing can only take place at a single pump power; third lasing does not occur. For the case of the first scenario, we evaluated the pump power corresponding to the maximum Stokes output.

6.6 Appendix: The derivation of the optical quality factor

We include here a brief derivation of the expression in Eq. (6.14) for the Quality factor, because it helps clarify the assumptions we have made. The pump transmission $T_{\rm p}$ of a ring resonator is given by [49, 116]

$$T_{\rm p} = \frac{(|\tau| - e^{-\frac{\alpha L}{2}})^2 + |\tau| e^{-\frac{\alpha L}{2}} (\frac{\Delta\theta}{2})^2}{(1 - |\tau| e^{-\frac{\alpha L}{2}})^2 + |\tau| e^{-\frac{\alpha L}{2}} (\frac{\Delta\theta}{2})^2}, \tag{6.20}$$

where $\Delta\theta = n_{\rm eff}\Delta\omega L/c$ is the phase change over a single round trip, which is a function of frequency ω, ring length L and the effective index $n_{\rm eff}$ (c is the speed of light). To find the full width at half maximum (FWHM), the transmission must be equal to

$$T_{\rm p} = \frac{1}{2}\big(T_{\rm max} + T_{\rm min}\big), \tag{6.21}$$

where $T_{\rm max}$ ($T_{\rm min}$) is the maximum (minimum) pump power transmission in the spectrum, given by

$$T_{\rm max} = \left(\frac{|\tau| + e^{-\frac{\alpha L}{2}}}{1 + |\tau| e^{-\frac{\alpha L}{2}}}\right)^2, \quad T_{\rm min} = \left(\frac{|\tau| - e^{-\frac{\alpha L}{2}}}{1 - |\tau| e^{-\frac{\alpha L}{2}}}\right)^2. \tag{6.22}$$

The phase angle corresponding to the FWHM, $\Delta\theta_{\rm FWHM}$ can then be obtained by substituting Eq. (6.21) in Eq. (6.20) and rearranging the equation

$$\Delta\theta_{\rm FWHM} = \frac{2\sqrt{2}(1 - 1|\tau| e^{-\frac{\alpha L}{2}})}{\sqrt{1 + |\tau|^2 e^{-\alpha L}}}. \tag{6.23}$$

Now the Q factor can be expressed as

$$Q_{\rm L} = \frac{\omega_0}{\Delta\omega_{\rm FWHM}} = \frac{\sqrt{2}\pi L n_{\rm eff}}{2\lambda} \frac{\sqrt{1 + |\tau|^2 e^{-\alpha L}}}{1 - |\tau| e^{-\frac{\alpha L}{2}}},$$

where $\Delta\omega_{\rm FWHM}$ is the linewidth and ω_0 is the pump resonance frequency.

Chapter 7

Conclusion

In this thesis, we studied stimulated Brillouin scattering in a number of potentially interested integrated structures. We used several analytic and numeric approaches to evaluate a broad range of SBS parameters such as gain, optical forces, pump and Stokes variations and optical-acoustic overlaps in the proposed geometries. In addition, we made some improvement in evaluating the optimized values of some relevant quantities in order to maximize the output Stokes power.

We studied SBS in silicon chalcogenide slot waveguides and showed that it is capable of providing optical and acoustic confinement, thus increasing the overlap between these fields. We identified those optical/acoustic modes with constructive interference in this mechanically robust structure and calculated SBS gain for a range of gap and slot widths to find the optimized geometry. The gain could increase to about $3300\,\mathrm{W^{-1}m^{-1}}$ in intra mode BSBS which is comparable with the values reported for suspended silicon nanowires in BSBS process. We also performed small signal analysis to determine the impact of nonlinear loss on the waveguide. For this, TPA and FCA induced by TPA coefficients were calculated for a range of waveguide dimensions. We also determined the optimum pump power and waveguide length as a function of SBS figure of merit. These expression are not specified to this waveguide and can be used regardless of configuration. Finally, we showed that a thin silica layer on top of the slot can significantly increase the SBS gain to $5000\,\mathrm{W^{-1}m^{-1}}$ — for 200 nm layer thickness — while reducing the nonlinear losses. This boosted the figure of merit and consequently the output Stokes power.

Straight waveguides with large SBS gain — such as our proposed slot — are appropriate candidates for applications, particularly when there is no strict limit due to the loss on size of a device. This is because the optimal waveguide length can reach several centimeters in conventional straight waveguides. If there exists only linear loss, then waveguide length is limited by the pump power corresponding to overheating. However, in the presence of nonlinear losses, any improvement on SBS figure of merit — either by reducing linear or nonlinear loss, or increasing the

SBS gain — leads to increase in optimal waveguide length for achieving maximum amplification. One way to reduce the waveguide length is to realize SBS in high Q factor structures.

We therefore performed an extensive study of SBS in integrated racetrack ring resonators. We combined coupled envelope equations with the resonator coupling equations and studied SBS in the steady state in the amplification regime. We first demonstrated amplification and determined the ring output in the presence of linear and nonlinear losses. In the presence of linear loss, we derived an expression to find the minimum pump power required to obtain amplification in a ring resonator. Then we studied a more realistic model by including the impact of pump depletion and showed that the overall Stokes gain depends on the power ratio between input pump and Stokes. In addition, the maximum amplification happens when the round-trip gain approaches $1/|\tau|$. In rings with nonlinear losses, we used a numeric approach to compute the Stokes and pump powers. We also studied rings within small signal approximation and derived conditions for critical coupling as well as analytic equations to evaluate Stokes transmission as a function of loss and SBS figure of merit. Finally, we analyzed the impact of physical parameters (thermal and length) as well as dispersion (Kerr nonlinearity and free carrier dispersion) on variation of free spectral range and consequently on SBS. We showed that the Kerr effect is usually weak and can be neglected provided that the pump and Stokes frequencies can be tuned to the cavity resonances. We derived conditions for all these parameters to ensure that they have negligible impact on SBS amplification.

Although SBS amplification in rings is interesting, these structures are usually studied for lasing purposes. We used our results and formulation in Chapter 5 as a foundation to study SBS lasing with ring resonators.

For rings in the lasing regime, we derived a general condition of SBS lasing in terms of round trip gain and applied it to evaluate SBS in rings with various loss mechanisms. We derived the threshold pump power in the presence of linear loss and showed that the common empirical expressions reported in the literature can lead to an inaccurate estimation of the required pump power. We also demonstrated possible scenarios of SBS lasing in the presence of nonlinear losses; in contrast to rings with linear losses, there exists a pump power interval at which lasing takes place when this interval becomes too small, then the ring falls into the amplification regime or even attenuates the Stokes. While using the numerical techniques to

illustrate large signal case studies, we provided analytic expressions for small signal investigations. We derived the threshold power and showed its variation as a function of loss and coupling parameters. Then we estimated the minimum and maximum pump power corresponding to the threshold interval. We finally showed that there exists an optimum pump power in this interval that results in the maximum Stokes power. We computed this pump power and its corresponding output Stokes for a range of SBS figures of merit and linear loss.

Future work and outlook

In this work we studied SBS in the steady state regime. This assumption allowed us to make the following simplifications; first we could neglect the time varying terms in the coupled equations. Second, we could simplify the time domain integral expressions for the polarization vectors. This is valid provided that susceptibilities are non-dispersive, which is reasonable if the optical envelope is CW or at least, contains long time optical pulses longer than the phonon lifetime. Second, in deriving the TPA and FCA coefficients, we determined the carrier concentration of a propagation medium in the steady state. In nanophotonic devices which operate with optical pulses, the full characteristics of SBS interactions still need to be explored. Although some aspects of dynamic SBS interactions — in the presence of optical pulses — such as optical threshold and gain linewidth are addressed for optical fibers [124], a detailed framework is required for integrated photonic waveguides.

There are interesting configurations for SBS applications which are not yet studied. In the coupled mode theory, we assumed that a waveguide is translationally invariant over its length. Therefore, the optical/acoustic modes were assumed to be unchanged through the waveguide. However, in tapered waveguides for instance, this is not the case. SBS can also be studied in periodic structures; it has been proposed to measure band gaps in phononic crystals used to realize dual acoustic-optical devices[125, 126].

With regard to SBS in resonators, we limited our studies to racetrack resonators. In addition, we have assumed that the ring is connected to a bus via a single coupling region. There exists other interesting ring configurations such as multi-ring resonators and add-drop rings that can bring further complexity in analysis while providing new potentials for tailoring SBS interactions.

A full investigation of the SBS lasing of resonators is still lacking. There are

various types of cavity resonators to study; some of them — such as microspheres and microdisks [118] — have already been explored. In Chapter 6 we assumed the SBS linewidth to be infinitely small. The measured values for silicon rings, for instance shows that it is of the order of a few ten kilo Hertz [53]. Using the wave approach, one can calculate the lasing linewidth for case studies by knowing structural and optical properties of ring. New models can be developed to account thermal phonons to compute the linewidth and possibly reduce it to the Schawlow-Townes limit.

Throughout this work, we studied SBS in short-infrared regime. However, investigations can be extended to other frequency ranges. The impact of optical frequency on the SBS gain is shown in Eq. (3.107), however, a more important change occurs when it comes to the impact of nonlinear losses. Today, there is an increasing interest toward tailoring SBS in higher wavelengths; Mid-IR, for instance is a promising frequency range for SBS in materials such as germanium in which TPA and therefore FCA-induced by TPA are negligible. Similar studies on silicon have shown potentials for further investigations [96]. In these cases, additional nonlinear loss mechanisms such as three — and even higher — photon absorptions might be required to include in the coupled equations.

Bibliography

[1] S. V. Gaponenko, *Introduction to nanophotonics*. Cambridge University Press, 2010.

[2] B. J. Eggleton, C. G. Poulton, and R. Pant, "Inducing and harnessing stimulated Brillouin scattering in photonic integrated circuits," *Advances in Optics and Photonics*, vol. 5, no. 4, pp. 536–587, 2013.

[3] M. Damzen, V. Vlad, A. Mocofanescu, and V. Babin, *Stimulated Brillouin scattering: fundamentals and applications*. CRC press, 2003.

[4] Z. Zalevsky and I. Abdulhalim, *Integrated nanophotonic devices*. Elsevier, 2014.

[5] M. Nikles, L. Thévenaz, and P. A. Robert, "Simple distributed fiber sensor based on Brillouin gain spectrum analysis," *Opt. Lett.*, vol. 21, no. 10, pp. 758–760, 1996.

[6] A. Byrnes, R. Pant, E. Li, D.-Y. Choi, C. G. Poulton, S. Fan, S. Madden, B. Luther-Davies, and B. J. Eggleton, "Photonic chip based tunable and reconfigurable narrowband microwave photonic filter using stimulated Brillouin scattering," *Opt. Express*, vol. 20, no. 17, pp. 18 836–18 845, 2012.

[7] H. G. Winful, I. V. Kabakova, and B. J. Eggleton, "Model for distributed feedback Brillouin lasers," *Opt. Express*, vol. 21, no. 13, pp. 16 191–16 199, Jul 2013.

[8] F. De Leonardis, B. Troia, R. A. Soref, and V. M. Passaro, "Theoretical demonstration of Brillouin lasing effect in racetrack resonators based on germanium waveguides in the mid-infrared," *Opt. Lett.*, vol. 41, no. 2, pp. 416–419, 2016.

[9] M. Kang, A. Nazarkin, A. Brenn, and P. S. J. Russell, "Tightly trapped acoustic phonons in photonic crystal fibres as highly nonlinear artificial Raman oscillators," *Nat. Phys.*, vol. 5, no. 4, pp. 276–280, 2009.

[10] P. T. Rakich, C. Reinke, R. Camacho, P. Davids, and Z. Wang, "Giant enhancement of stimulated Brillouin scattering in the subwavelength limit," *Phys. Rev. X*, vol. 2, no. 1, p. 011008, 2012.

[11] C. J. Sarabalis, J. T. Hill, and A. H. Safavi-Naeini, "Guided acoustic and optical waves in silicon-on-insulator for Brillouin scattering and optomechanics," *APL Photonics*, vol. 1, no. 7, p. 071301, 2016.

[12] R. Pant, C. G. Poulton, D.-Y. Choi, H. Mcfarlane, S. Hile, E. Li, L. Thevenaz, B. Luther-Davies, S. J. Madden, and B. J. Eggleton, "On-chip stimulated Brillouin scattering," *Opt. Express*, vol. 19, no. 9, pp. 8285–8290, 2011.

[13] S. R. Mirnaziry, C. Wolff, M. Steel, B. J. Eggleton, and C. G. Poulton, "Stimulated Brillouin scattering in silicon/chalcogenide slot waveguides," *Opt. Express*, vol. 24, no. 5, pp. 4786–4800, 2016.

[14] C. Wolff, R. Soref, C. Poulton, and B. Eggleton, "Germanium as a material for stimulated Brillouin scattering in the mid-infrared," *Opt. Express*, vol. 22, no. 25, pp. 30 735–30 747, 2014.

[15] M. Cardona and R. Merlin, "Light scattering in solids ix," in *Light Scattering in Solid IX*. Springer, 2006, pp. 1–14.

[16] E. Gross, "Change of wave-length of light due to elastic heat waves at scattering in liquids," *Nature*, vol. 126, no. 201, p. 400, 1930.

[17] R. Chiao, C. Townes, and B. Stoicheff, "Stimulated Brillouin scattering and coherent generation of intense hypersonic waves," *Phys. Rev. Lett.*, vol. 12, no. 21, p. 592, 1964.

[18] R. G. Brewer and K. E. Rieckhoff, "Stimulated Brillouin scattering in liquids," *Phys. Rev. Lett.*, vol. 13, no. 11, p. 334, 1964.

[19] J.-Z. Zhang and R. K. Chang, "Generation and suppression of stimulated Brillouin scattering in single liquid droplets," *J. Opt. Soc. Am. B*, vol. 6, no. 2, pp. 151–153, 1989.

[20] E. Hagenlocker and W. Rado, "Stimulated Brillouin and Raman scattering in gases," *Appl. Phys. Lett.*, vol. 7, no. 9, pp. 236–238, 1965.

[21] E. Ippen and R. Stolen, "Stimulated Brillouin scattering in optical fibers," *Appl. Phys. Lett.*, vol. 21, no. 11, pp. 539–541, 1972.

[22] R. H. Stolen, "The early years of fiber nonlinear optics," *J. Lightwave Technol.*, vol. 26, no. 9, pp. 1021–1031, 2008.

[23] A. Kobyakov, M. Sauer, and D. Chowdhury, "Stimulated Brillouin scattering in optical fibers," *Advances in optics and photonics*, vol. 2, no. 1, pp. 1–59, 2010.

[24] R. Shelby, M. Levenson, and P. Bayer, "Guided acoustic-wave Brillouin scattering," *Phys. Rev. B*, vol. 31, no. 8, p. 5244, 1985.

[25] D. Culverhouse, F. Farahi, C. Pannell, and D. Jackson, "Potential of stimulated Brillouin scattering as sensing mechanism for distributed temperature sensors," *Electron. Lett.*, vol. 25, no. 14, pp. 913–915, 1989.

[26] Z. Ou, X. Bao, Y. Li, B. Saxena, and L. Chen, "Ultranarrow linewidth Brillouin fiber laser," *IEEE Photon. Technol. Lett.*, vol. 26, no. 20, pp. 2058–2061, 2014.

[27] K. S. Abedin, "Brillouin amplification and lasing in a single-mode as 2 se 3 chalcogenide fiber," *Opt. Lett.*, vol. 31, no. 11, pp. 1615–1617, 2006.

[28] P. Dainese, P. S. J. Russell, N. Joly, J. Knight, G. Wiederhecker, H. L. Fragnito, V. Laude, and A. Khelif, "Stimulated Brillouin scattering from multi-ghz-guided acoustic phonons in nanostructured photonic crystal fibres," *Nature Phys.*, vol. 2, no. 6, pp. 388–392, 2006.

[29] P. Dainese, P. S. J. Russell, G. S. Wiederhecker, N. Joly, H. L. Fragnito, V. Laude, and A. Khelif, "Raman-like light scattering from acoustic phonons in photonic crystal fiber," *Opt. Express*, vol. 14, no. 9, pp. 4141–4150, 2006.

[30] J. E. McElhenny, *Acoustic waves in small-core photonic crystal fibers: An investigation through Brillouin scattering.* Lehigh University, 2009.

[31] J.-C. Beugnot, T. Sylvestre, D. Alasia, H. Maillotte, V. Laude, A. Monteville, L. Provino, N. Traynor, S. F. Mafang, and L. Thévenaz, "Complete experimental characterization of stimulated Brillouin scattering in photonic crystal fiber," *Opt. Express*, vol. 15, no. 23, pp. 15 517–15 522, 2007.

[32] L. Zou, X. Bao, and L. Chen, "Brillouin scattering spectrum in photonic crystal fiber with a partially germanium-doped core," *Opt. Lett.*, vol. 28, no. 21, pp. 2022–2024, 2003.

[33] C. Fortier, J. Fatome, S. Pitois, F. Smektala, G. Millot, J. Troles, F. Désévédavy, P. Houizot, L. Brilland, and N. Traynor, "Experimental investigation of Brillouin and Raman scattering in a 2sg sulfide glass microstructured chalcogenide fiber," *Opt. Express*, vol. 16, no. 13, pp. 9398–9404, 2008.

[34] J. E. McElhenny, R. K. Pattnaik, J. Toulouse, K. Saitoh, and M. Koshiba, "Unique characteristic features of stimulated Brillouin scattering in small-core photonic crystal fibers," *J. Opt. Soc. Am. B*, vol. 25, no. 4, pp. 582–593, 2008.

[35] D. Elser, U. Andersen, A. Korn, O. Glöckl, S. Lorenz, C. Marquardt, and G. Leuchs, "Reduction of guided acoustic wave Brillouin scattering in photonic crystal fibers," *Phys. Rev. Lett.*, vol. 97, no. 13, p. 133901, 2006.

[36] S. Yang, H. Chen, C. Qiu, M. Chen, M. Chen, S. Xie, J. Li, and W. Chen, "Slow-light delay enhancement in small-core pure silica photonic crystal fiber based on Brillouin scattering," *Opt. Lett.*, vol. 33, no. 2, pp. 95–97, 2008.

[37] N. A. Olsson and J. P. V. D. Ziel, "Fibre Brillouin amplifier with electronically controlled bandwidth," *Electron. Lett.*, vol. 22, no. 9, pp. 488–490, April 1986.

[38] W. Qiu, P. T. Rakich, H. Shin, H. Dong, M. Soljačić, and Z. Wang, "Stimulated Brillouin scattering in nanoscale silicon step-index waveguides: a general framework of selection rules and calculating sbs gain," *Opt. Express*, vol. 21, no. 25, pp. 31 402–31 419, Dec 2013.

[39] R. Van Laer, B. Kuyken, D. Van Thourhout, and R. Baets, "Analysis of enhanced stimulated Brillouin scattering in silicon slot waveguides," *Opt. Lett.*, vol. 39, no. 5, pp. 1242–1245, 2014.

[40] P. T. Rakich, P. Davids, and Z. Wang, "Tailoring optical forces in waveguides through radiation pressure and electrostrictive forces," *Opt. Express*, vol. 18, no. 14, pp. 14 439–14 453, 2010.

[41] R. Pant, E. Li, D.-Y. Choi, C. Poulton, S. J. Madden, B. Luther-Davies, and B. J. Eggleton, "Cavity enhanced stimulated Brillouin scattering in an

optical chip for multiorder stokes generation," *Opt. Lett.*, vol. 36, no. 18, pp. 3687–3689, 2011.

[42] J. Kim, M. C. Kuzyk, K. Han, H. Wang, and G. Bahl, "Non-reciprocal Brillouin scattering induced transparency," *Nat. Phys.*, vol. 11, 2015.

[43] G. Bahl, M. Tomes, F. Marquardt, and T. Carmon, "Observation of spontaneous Brillouin cooling," *Nat. Phys.*, vol. 8, 2012.

[44] G. Bahl, J. Zehnpfennig, M. Tomes, and T. Carmon, "Stimulated optomechanical excitation of surface acoustic waves in a microdevice," *Nat. Commun.*, vol. 2, 2011.

[45] C. Wolff, B. Stiller, B. J. Eggleton, M. J. Steel, and C. G. Poulton, "Cascaded forward Brillouin scattering to all stokes orders," *New J. Phys.*, vol. 19, no. 2, p. 023021, 2017.

[46] R. Van Laer, B. Kuyken, D. Van Thourhout, and R. Baets, "Interaction between light and highly confined hypersound in a silicon photonic nanowire," *Nat. Photonics*, vol. 9, no. 3, pp. 199–203, 2015.

[47] E. A. Kittlaus, H. Shin, and P. T. Rakich, "Large Brillouin amplification in silicon," *Nat. Photon.*, vol. 10, 2016.

[48] C. Wolff, P. Gutsche, M. J. Steel, B. J. Eggleton, and C. G. Poulton, "Impact of nonlinear loss on stimulated Brillouin scattering," *J. Opt. Soc. Am. B*, vol. 32, no. 9, pp. 1968–1978, 2015.

[49] S. R. Mirnaziry, C. Wolff, M. Steel, B. J. Eggleton, and C. G. Poulton, "Stimulated Brillouin scattering in integrated ring resonators," *J. Opt. Soc. Am. B*, vol. 34, no. 5, pp. 937–949, 2017.

[50] B. Morrison, A. Casas-Bedoya, G. Ren, K. Vu, Y. Liu, A. Zarifi, T. G. Nguyen, D.-Y. Choi, D. Marpaung, S. J. Madden, A. Mitchell, and B. J. Eggleton, "Compact Brillouin devices through hybrid integration on silicon," *Optica*, vol. 4, no. 8, pp. 847–854, Aug 2017.

[51] L. Stokes, M. Chodorow, and H. Shaw, "All-fiber stimulated Brillouin ring laser with submilliwatt pump threshold," *Opt. Lett.*, vol. 7, no. 10, pp. 509–511, 1982.

[52] S. Smith, F. Zarinetchi, and S. Ezekiel, "Narrow-linewidth stimulated Brillouin fiber laser and applications," *Opt. Lett.*, vol. 16, no. 6, pp. 393–395, 1991.

[53] N. T. Otterstrom, R. O. Behunin, E. A. Kittlaus, Z. Wang, and P. T. Rakich, "A silicon Brillouin laser," *arXiv preprint arXiv:1705.05813*, 2017.

[54] N. Dostart, S. Kim, and G. Bahl, "Giant gain enhancement in surface-confined resonant stimulated Brillouin scattering," *Laser Photon. Rev.*, vol. 9, no. 6, pp. 689–705, 2015.

[55] J. Li, H. Lee, and K. J. Vahala, "Microwave synthesizer using an on-chip Brillouin oscillator," *Nat. Commun.*, vol. 4, 2013.

[56] P. Del'Haye, S. A. Diddams, and S. B. Papp, "Laser-machined ultra-high-q microrod resonators for nonlinear optics," *Appl. Phys. Lett.*, vol. 102, no. 22, p. 221119, 2013.

[57] M. Merklein, A. Casas-Bedoya, D. Marpaung, T. F. Büttner, M. Pagani, B. Morrison, I. V. Kabakova, and B. J. Eggleton, "Stimulated Brillouin scattering in photonic integrated circuits: novel applications and devices," *IEEE J. Sel. Top. Quantum Electron.*, vol. 22, no. 2, pp. 336–346, 2016.

[58] D. Marpaung, B. Morrison, M. Pagani, R. Pant, D.-Y. Choi, B. Luther-Davies, S. J. Madden, and B. J. Eggleton, "Low-power, chip-based stimulated Brillouin scattering microwave photonic filter with ultrahigh selectivity," *Optica*, vol. 2, no. 2, pp. 76–83, 2015.

[59] W. Zhang and R. A. Minasian, "Widely tunable single-passband microwave photonic filter based on stimulated Brillouin scattering," *IEEE Photon. Technol. Lett.*, vol. 23, no. 23, pp. 1775–1777, 2011.

[60] B. Morrison, D. Marpaung, R. Pant, E. Li, D.-Y. Choi, S. Madden, B. Luther-Davies, and B. J. Eggleton, "Tunable microwave photonic notch filter using on-chip stimulated Brillouin scattering," *Opt. Commun.*, vol. 313, pp. 85–89, 2014.

[61] H. Jiang, D. Marpaung, M. Pagani, K. Vu, D.-Y. Choi, S. J. Madden, L. Yan, and B. J. Eggleton, "Wide-range, high-precision multiple microwave frequency measurement using a chip-based photonic Brillouin filter," *Optica*, vol. 3, no. 1, pp. 30–34, 2016.

[62] J. C. Yong, L. Thévenaz, and B. Y. Kim, "Brillouin fiber laser pumped by a dfb laser diode," *J. Lightwave Technol.*, vol. 21, no. 2, p. 546, 2003.

[63] E. Garmire, "Perspectives on stimulated Brillouin scattering," *New J. Phys.*, vol. 19, no. 1, p. 011003, 2017.

[64] J. Li, H. Lee, and K. J. Vahala, "Low-noise Brillouin laser on a chip at 1064 nm," *Opt. Lett.*, vol. 39, no. 2, pp. 287–290, 2014.

[65] Z. Zhu, D. J. Gauthier, and R. W. Boyd, "Stored light in an optical fiber via stimulated Brillouin scattering," *Science*, vol. 318, no. 5857, pp. 1748–1750, 2007.

[66] A. M. Weiner, D. Leaird, D. Reitze, and E. G. Paek, "Spectral holography of shaped femtosecond pulses," *Opt. Lett.*, vol. 17, no. 3, pp. 224–226, 1992.

[67] M. Eisaman, A. André, F. Massou, M. Fleischhauer *et al.*, "Electromagnetically induced transparency with tunable single-photon pulses," *Nature*, vol. 438, no. 7069, p. 837, 2005.

[68] C.-H. Dong, Z. Shen, C.-L. Zou, Y.-L. Zhang, W. Fu, and G.-C. Guo, "Brillouin-scattering-induced transparency and non-reciprocal light storage," *Nat. Commun.*, vol. 6, p. 6193, 2015.

[69] M. Merklein, B. Stiller, K. Vu, S. J. Madden, and B. J. Eggleton, "An on-chip multi-wavelength photonic-phononic memory," in *Lasers and Electro-Optics (CLEO), 2016 Conference on.* IEEE, 2016, pp. 1–2.

[70] Y. Shi, Z. Yu, and S. Fan, "Limitations of nonlinear optical isolators due to dynamic reciprocity," *Nat. Photonics*, vol. 9, no. 6, pp. 388–392, 2015.

[71] J. Kim, S. Kim, and G. Bahl, "Complete linear optical isolation at the microscale with ultralow loss," *Scientific Reports*, vol. 7, 2017.

[72] X. Huang and S. Fan, "Complete all-optical silica fiber isolator via stimulated Brillouin scattering," *J. Lightwave Technol.*, vol. 29, no. 15, pp. 2267–2275, 2011.

[73] R. W. Boyd, "Nonlinear optics," in *Handbook of Laser Technology and Applications (Three-Volume Set).* Taylor & Francis, 2003, pp. 161–183.

[74] A. Corvo and A. Gavrielides, "Forward stimulated Brillouin scattering," *J. Appl. Phys.*, vol. 63, no. 11, pp. 5220–5227, 1988.

[75] J. Sipe and M. Steel, "A hamiltonian treatment of stimulated Brillouin scattering in nanoscale integrated waveguides," *New J. Phys.*, vol. 18, no. 4, p. 045004, 2016.

[76] R. Van Laer, R. Baets, and D. Van Thourhout, "Unifying Brillouin scattering and cavity optomechanics," *Phys. Rev. A*, vol. 93, p. 053828, May 2016.

[77] Y. R. Shen and N. Bloembergen, "Theory of stimulated Brillouin and Raman scattering," *Phys. Rev.*, vol. 137, no. 6A, p. A1787, 1965.

[78] H. Zoubi and K. Hammerer, "Optomechanical multimode hamiltonian for nanophotonic waveguides," *Phys. Rev. A*, vol. 94, no. 5, p. 053827, 2016.

[79] C. Wolff, M. J. Steel, B. J. Eggleton, and C. G. Poulton, "Stimulated Brillouin scattering in integrated photonic waveguides: Forces, scattering mechanisms, and coupled-mode analysis," *Phys. Rev. A*, vol. 92, p. 013836, Jul 2015.

[80] B. A. Auld, *Acoustic fields and waves in solids [by] B. A. Auld*. Wiley New York, 1973.

[81] R. D. M. Shelby L. Peterie and J. Ivanov. Seismology and its applications in kansas. [Online]. Available: http://www.kgs.ku.edu/Publications/PIC/pic37.html

[82] G. Müller, *Theory of Elastic Waves*, ser. Scientific Technical Report 2007 : GeoForschungsZentrum Potsdam. GFZ, 2007.

[83] A. W. Snyder and J. Love, *Optical waveguide theory*. Springer Science & Business Media, 2012.

[84] J. F. Nye, *Physical properties of crystals: their representation by tensors and matrices*. Oxford university press, 1985.

[85] D. Royer and E. Dieulesaint, *Elastic waves in solids II: generation, acousto-optic interaction, applications*. Springer Science & Business Media, 1999.

[86] G. P. Agrawal, *Nonlinear fiber optics*. Academic press, 2007.

[87] J. Leuthold, C. Koos, and W. Freude, "Nonlinear silicon photonics," *Nat. Photonics*, vol. 4, no. 8, pp. 535–544, 2010.

[88] Q. Lin, O. J. Painter, and G. P. Agrawal, "Nonlinear optical phenomena in silicon waveguides: modeling and applications," *Opt. Express*, vol. 15, no. 25, pp. 16 604–16 644, 2007.

[89] X. Sang, E.-K. Tien, and O. Boyraz, "Applications of two photon absorption in silicon," *Journal of optoelectronics and advanced materials*, vol. 11, no. 1, p. 15, 2009.

[90] I. Aldaya, A. Gil-Molina, J. L. Pita, L. H. Gabrielli, H. L. Fragnito, and P. Dainese, "Nonlinear carrier dynamics in silicon nano-waveguides," *Optica*, vol. 4, no. 10, pp. 1219–1227, Oct 2017.

[91] V. R. Almeida, Q. Xu, C. A. Barrios, and M. Lipson, "Guiding and confining light in void nanostructure," *Opt. Lett.*, vol. 29, no. 11, pp. 1209–1211, 2004.

[92] C. Wolff, M. J. Steel, B. J. Eggleton, and C. G. Poulton, "Stimulated Brillouin scattering in integrated photonic waveguides: Forces, scattering mechanisms, and coupled-mode analysis," *Phys. Rev. A*, vol. 92, no. 1, p. 013836, 2015.

[93] R. Pant, D. Marpaung, I. V. Kabakova, B. Morrison, C. G. Poulton, and B. J. Eggleton, "On-chip stimulated Brillouin scattering for microwave signal processing and generation," *Laser Photonics Rev.*, vol. 8, no. 5, pp. 653–666, 2014.

[94] H. Shin, W. Qiu, R. Jarecki, J. A. Cox, R. H. Olsson III, A. Starbuck, Z. Wang, and P. T. Rakich, "Tailorable stimulated Brillouin scattering in nanoscale silicon waveguides," *Nat. Commun.*, vol. 4, 2013.

[95] C. Wolff, M. Steel, and C. Poulton, "Formal selection rules for Brillouin scattering in integrated waveguides and structured fibers," *Opt. Express*, vol. 22, no. 26, pp. 32 489–32 501, 2014.

[96] C. Wolff, P. Gutsche, M. J. Steel, B. J. Eggleton, and C. G. Poulton, "Power limits and a figure of merit for stimulated Brillouin scattering in the presence of third and fifth order loss," *Opt. Express*, vol. 23, no. 20, pp. 26 628–26 638, 2015.

[97] B.-S. Song, S. Noda, T. Asano, and Y. Akahane, "Ultra-high-q photonic double-heterostructure nanocavity," *Nat. Mater.*, vol. 4, no. 3, pp. 207–210, 2005.

[98] W. Loh, A. A. S. Green, F. N. Baynes, D. C. Cole, F. J. Quinlan, H. Lee, K. J. Vahala, S. B. Papp, and S. A. Diddams, "Dual-microcavity narrow-linewidth Brillouin laser," *Optica*, vol. 2, no. 3, pp. 225–232, Mar 2015.

[99] W. Loh, S. B. Papp, and S. A. Diddams, "Noise and dynamics of stimulated-Brillouin-scattering microresonator lasers," *Phys. Rev. A*, vol. 91, no. 5, p. 053843, 2015.

[100] H. Lee, T. Chen, J. Li, K. Y. Yang, S. Jeon, O. Painter, and K. J. Vahala, "Chemically etched ultrahigh-q wedge-resonator on a silicon chip," *Nat. Photonics*, vol. 6, pp. 369 – 373, 2012.

[101] K. J. Vahala, "Optical microcavities," *Nature*, vol. 424, no. 6950, pp. 839–846, 2003.

[102] J. Geng, S. Staines, Z. Wang, J. Zong, M. Blake, and S. Jiang, "Highly stable low-noise Brillouin fiber laser with ultranarrow spectral linewidth," *IEEE Photon. Technol. Lett*, vol. 18, no. 17, pp. 1813–1815, 2006.

[103] W. R. McKinnon, D.-X. Xu, C. Storey, E. Post, A. Densmore, A. Delâge, P. Waldron, J. H. Schmid, and S. Janz, "Extracting coupling and loss coefficients from a ring resonator," *Opt. Express*, vol. 17, no. 21, pp. 18 971–18 982, Oct 2009.

[104] D. G. Rabus, *Integrated ring resonators*. Springer, 2007.

[105] A. D. Bristow, N. Rotenberg, and H. M. Van Driel, "Two-photon absorption and kerr coefficients of silicon for 850–2200 nm," *Appl. phys. lett.*, vol. 90, no. 19, p. 191104, 2007.

[106] M. Tomes and T. Carmon, "Photonic micro-electromechanical systems vibrating at x-band (11-ghz) rates," *Phys. Rev. Lett.*, vol. 102, no. 11, p. 113601, 2009.

[107] Q. Lin, O. J. Painter, and G. P. Agrawal, "Nonlinear optical phenomena in silicon waveguides: modeling and applications," *Opt. Express*, vol. 15, no. 25, pp. 16 604–16 644, 2007.

[108] J. Komma, C. Schwarz, G. Hofmann, D. Heinert, and R. Nawrodt, "Thermo-optic coefficient of silicon at 1550 nm and cryogenic temperatures," *Appl. Phys. Lett.*, vol. 101, no. 4, p. 1905, 2012.

[109] H. Watanabe, N. Yamada, and M. Okaji, "Linear thermal expansion coefficient of silicon from 293 to 1000 K," *Int. J. Thermophys.*, vol. 25, no. 1, pp. 221–236, 2004.

[110] V. R. Almeida, C. A. Barrios, R. R. Panepucci, and M. Lipson, "All-optical control of light on silicon chip," *Nature*, vol. 431, no. 7012, p. 1081, 2004.

[111] S. Azzini, D. Grassani, M. Galli, L. C. Andreani, M. Sorel, M. J. Strain, L. Helt, J. Sipe, M. Liscidini, and D. Bajoni, "From classical four-wave mixing to parametric fluorescence in silicon microring resonators," *Opt. Lett.*, vol. 37, no. 18, pp. 3807–3809, 2012.

[112] M. Ferrera, L. Razzari, D. Duchesne, R. Morandotti, Z. Yang, M. Liscidini, J. Sipe, S. Chu, B. Little, and D. Moss, "Low-power continuous-wave nonlinear optics in doped silica glass integrated waveguide structures," *Nat. Photonics*, vol. 2, no. 12, pp. 737–740, 2008.

[113] G. Lin, S. Diallo, K. Saleh, R. Martinenghi, J.-C. Beugnot, T. Sylvestre, and Y. K. Chembo, "Cascaded Brillouin lasing in monolithic barium fluoride whispering gallery mode resonators," *Appl. Phys. Lett.*, vol. 105, no. 23, p. 231103, 2014.

[114] J. Li, H. Lee, and K. J. Vahala, "Low-noise Brillouin laser on a chip at 1064 nm," *Opt. Lett.*, vol. 39, no. 2, pp. 287–290, 2014.

[115] I. V. Kabakova, R. Pant, D.-Y. Choi, S. Debbarma, B. Luther-Davies, S. J. Madden, and B. J. Eggleton, "Narrow linewidth Brillouin laser based on chalcogenide photonic chip," *Opt. Lett.*, vol. 38, no. 17, pp. 3208–3211, 2013.

[116] S. R. Mirnaziry, "Stimulated brillouin scattering in nanophotonic waveguides and resonators," Ph.D. dissertation, School of Mathematical and Physical Sciences, 2018.

[117] W. Loh, A. A. Green, F. N. Baynes, D. C. Cole, F. J. Quinlan, H. Lee, K. J. Vahala, S. B. Papp, and S. A. Diddams, "Dual-microcavity narrow-linewidth Brillouin laser," *Optica*, vol. 2, no. 3, pp. 225–232, 2015.

[118] S. Spillane, T. Kippenberg, and K. Vahala, "Ultralow-threshold Raman laser using a spherical dielectric microcavity," *Nature*, vol. 415, no. 6872, pp. 621–623, 2002.

[119] T. J. Kippenberg, S. M. Spillane, B. Min, and K. J. Vahala, "Theoretical and experimental study of stimulated and cascaded Raman scattering in ultrahigh-q optical microcavities," *IEEE J. Sel. Top. Quantum Electron.*, vol. 10, no. 5, pp. 1219–1228, 2004.

[120] A. Yariv, "Universal relations for coupling of optical power between microresonators and dielectric waveguides," *Electron. Lett.*, vol. 36, no. 4, pp. 321–322, 2000.

[121] D. G. Rabus, *Integrated ring resonators*. Springer, 2007.

[122] W. McKinnon, D.-X. Xu, C. Storey, E. Post, A. Densmore, A. Delâge, P. Waldron, J. Schmid, and S. Janz, "Extracting coupling and loss coefficients from a ring resonator," *Opt. Express*, vol. 17, no. 21, pp. 18 971–18 982, 2009.

[123] R. G. Smith, "Optical power handling capacity of low loss optical fibers as determined by stimulated Raman and Brillouin scattering," *Appl. Opt.*, vol. 11, no. 11, pp. 2489–2494, 1972.

[124] G. L. Keaton, M. J. Leonardo, M. W. Byer, and D. J. Richard, "Stimulated Brillouin scattering of pulses in optical fibers," *Opt. Express*, vol. 22, no. 11, pp. 13 351–13 365, 2014.

[125] M. Maldovan and E. L. Thomas, "Simultaneous localization of photons and phonons in two-dimensional periodic structures," *Appl. Phys. Lett.*, vol. 88, no. 25, p. 251907, 2006.

[126] A. Akimov, Y. Tanaka, A. Pevtsov, S. Kaplan, V. Golubev, S. Tamura, D. Yakovlev, and M. Bayer, "Hypersonic modulation of light in three-dimensional photonic and phononic band-gap materials," *Phys. Rev. Lett.*, vol. 101, no. 3, p. 033902, 2008.